冷原子中的凝聚态问题

刘 伍 明

(中国科学院物理所）

http://www.iphy.ac.cn

Email: wmliu@aphy.iphy.ac.cn

Phone: 10-82649249(o)

Outline

1. Introduction
2. Superfluidity
3. Quantum phase transition
4. Strong correlated system
5. Spinor BEC
6. Boson - Fermion mixture
7. BEC – BCS crossover
8. Spin polarized fermi gas
9. BEC in solid
10. Application
11. Outlook

1. Introduction

Figure 1 Overview of neutral atomic and molecular cooling and trapping. The energy scale spans 12 orders of magnitude in kinetic energy E of atomic motion, expressed in temperature units $T = E/k_B$ (k_B is the Boltzmann constant). The length scale shows the corresponding de Broglie wavelength $\lambda = h/p$ (h is the Planck constant), where momentum $p = (2mE)^{1/2}$. The line to guide the eye is calculated using the mass of the ^{23}Na atom for m. Typical atomic dimensions are on the order of $1a_0 = 0.0529$ nm, the Bohr radius of the H atom, whereas Bose–Einstein condensates can have dimensions on the order of 100 µm. The figure also indicates typical orders of magnitude for familiar energy scales associated with atomic fine structure, hyperfine structure, natural radiative broadening and optical or magnetic energy shifts. Cooling requires a dissipative process to remove kinetic energy, whereas trapping requires a spatially dependent force to act on the atoms. Laser cooling[2–4] typically reaches kinetic energies below 1 mK, where k_BT is smaller than natural line widths, and atoms can be confined in a magneto-optical trap or optical trap. The latter uses a spatially dependent light shift attributable to a laser field to create a trapping potential for atoms. Similarly, a standing-wave light field can produce a periodic potential in space called an optical lattice[5,6] with individual lattice cells spaced by $\lambda_L/2$, where λ_L is the wavelength of the laser that makes the lattice. Atoms whose magnetic Zeeman shift decreases with decreasing field strength can be trapped in a region of space with a magnetic field minimum. Evaporative cooling[5] of trapped atoms can dramatically lower the temperature and reach the limit of quantum degeneracy, where the phase space density ρ, defined as the number of particles per cubic thermal de Broglie wavelength, is of order unity. If the atoms are bosons, then Bose–Einstein condensation occurs when ρ reaches the critical value of 2.6 (ref. 6; and see review in this issue by Anglin and Ketterle, pages 211–218).

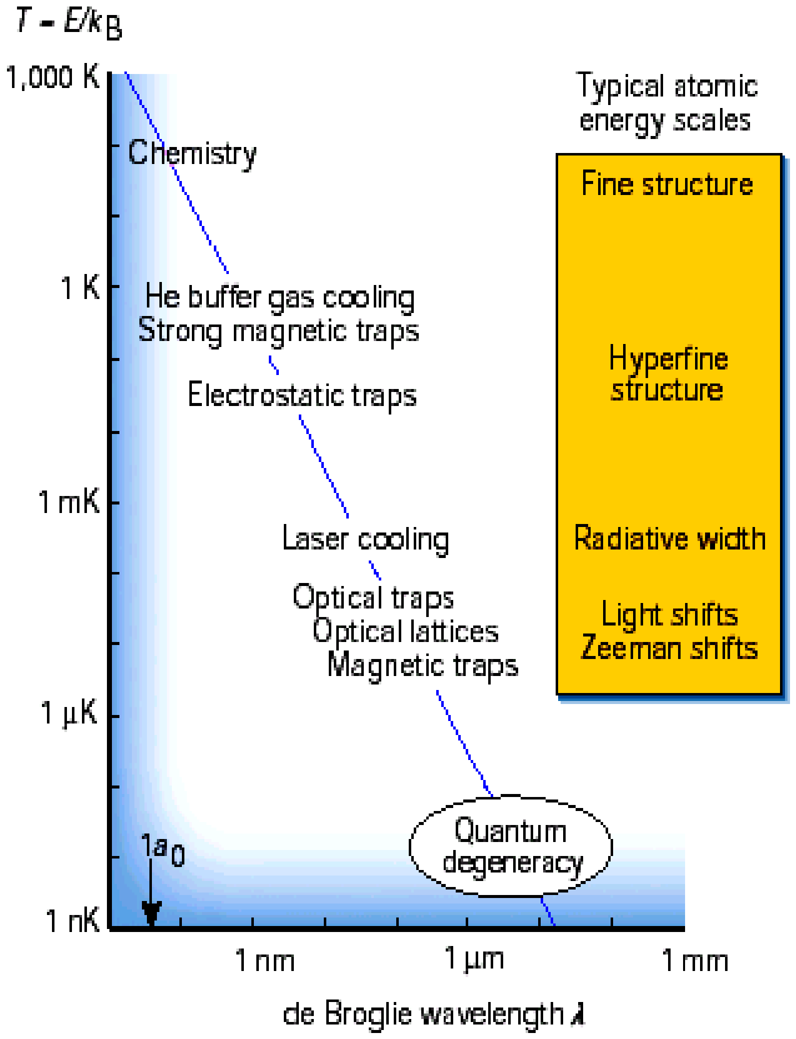

超导超流与相变

1913 H. K. Onnes 低温研究，液氦超导

- 1962 Lev Davidovich Landau 液氦超流理论
- 1972 J. Bardeen, L. N. Cooper, J.R. Schrieffer 超导 BCS 理论
- 1973 Ivar Giaever 超导隧道效应, Brian D. Josephson 超导隧道结
- 1978 Pyotr Leonidovich Kapitsa 氦II超流性
- 1982 Kenneth G. Wilson 连续相变重整化群理论
- 1987 K. Alexander Muller, J. Georg Bednorz 发现高温超导
- 1996 D. D. Osheroff, D. M. Lee, R. C. Richardson 发现氦三超流性
- 2001 E.A. Cornell, W. Ketterle, C.E. Wieman 玻色 - 爱因斯坦凝聚
- 2003 A. A. Abrikosov, U. L. Ginzburg, A. J. Leggett 超导 超流

1.1. BEC of ideal gas

7Li

6Li

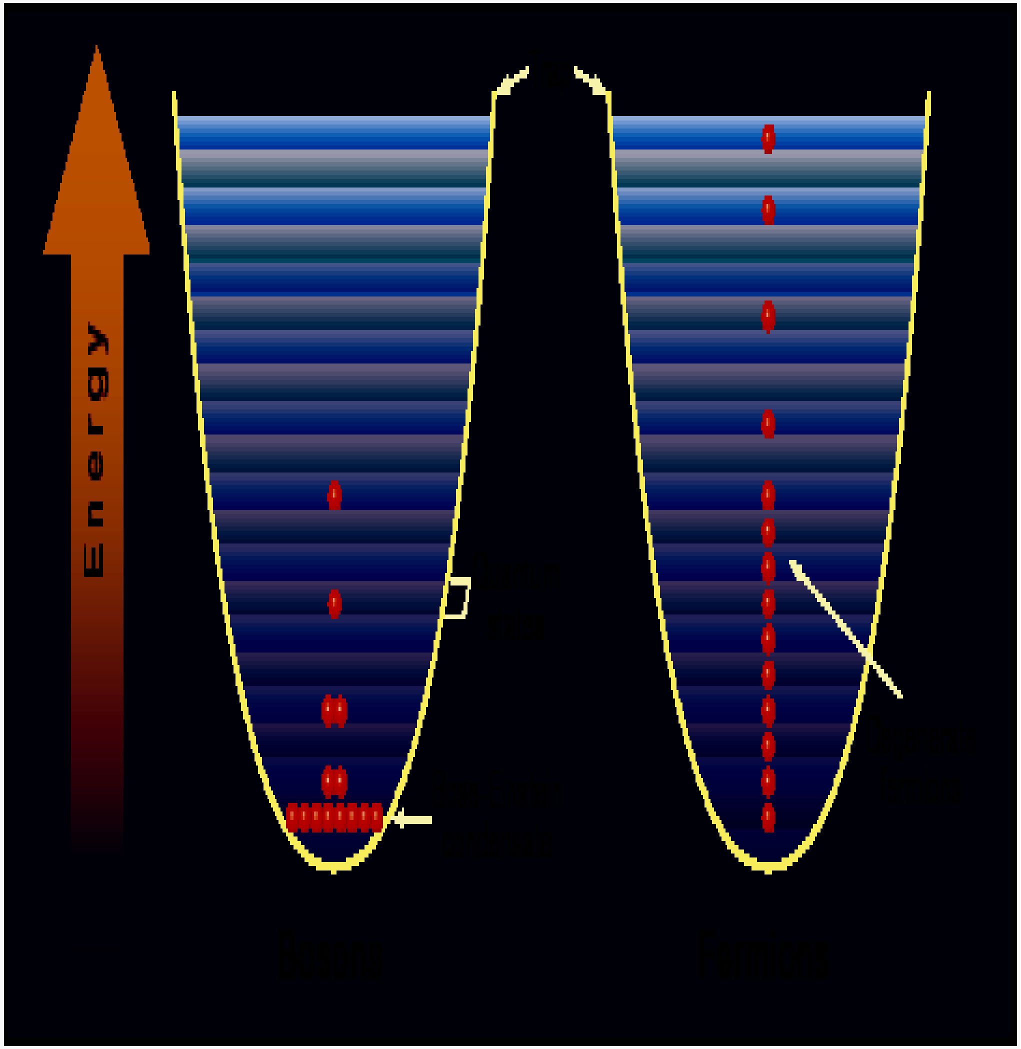

Joiners and loners. Near absolute zero, identical bosons pile into the least energetic quantum state (left), whereas identical fermions stack into low-energy states one by one.

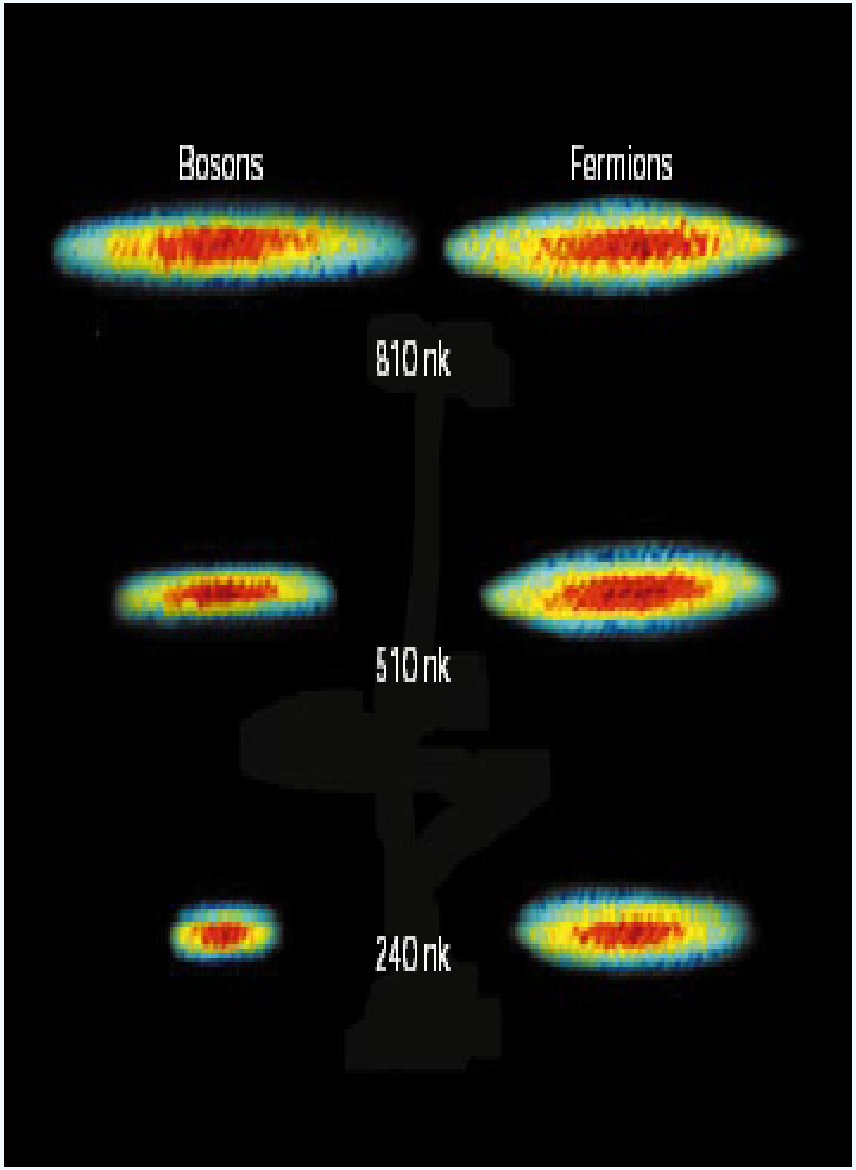

1.2. BEC in dilute gas

- Laser cooling
- Evaporative cooling—C.E. Wieman
- Block—Rotating magnetic field—E.A. Cornell (Rb)
- Block---laser beam—W. Ketterle (Na)
- R. Hulet (Li) ???

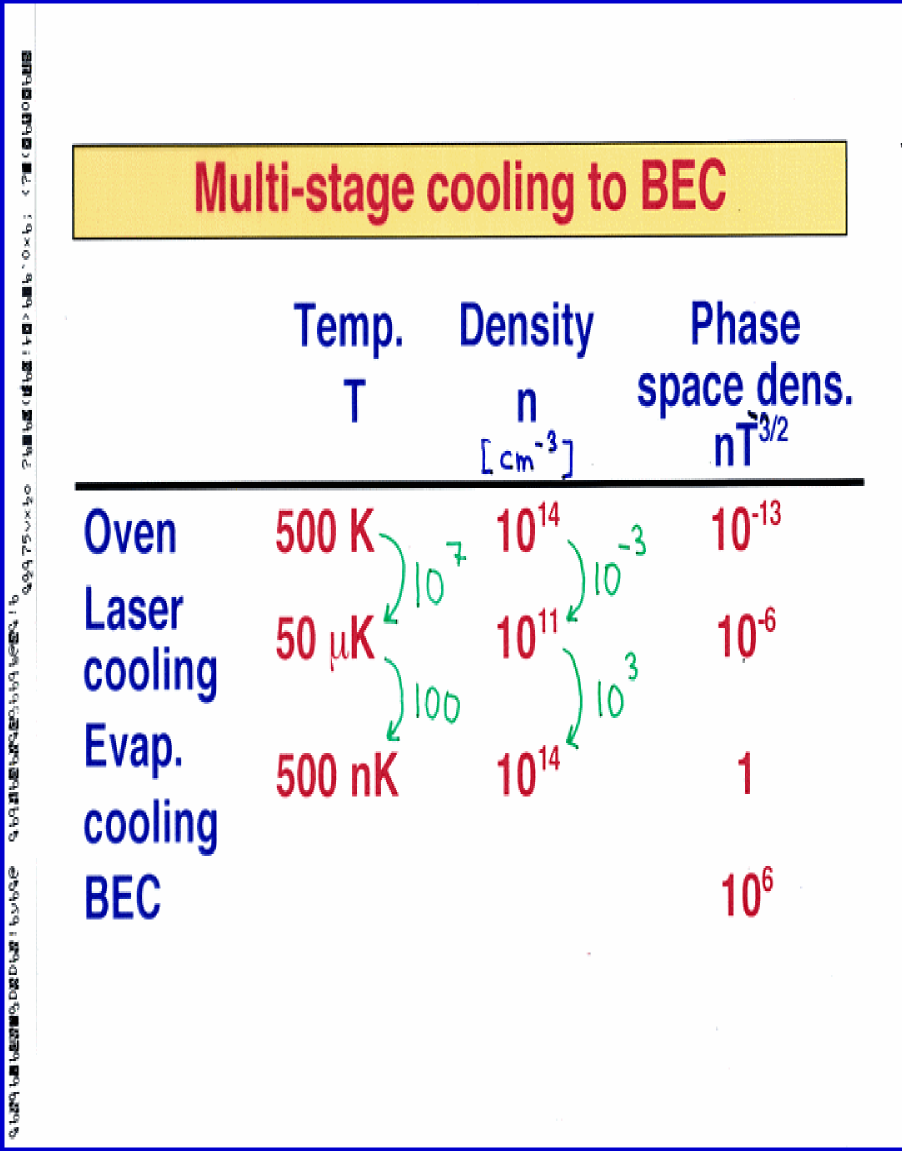

Multi-stage cooling to BEC

	Temp. T	Density n [cm^{-3}]	Phase space dens. $nT^{-3/2}$
Oven	500 K	10^{14}	10^{-13}
	10^{7}	10^{-3}	
Laser cooling	50 μK	10^{11}	10^{-6}
	100	10^{3}	
Evap. cooling	500 nK	10^{14}	1
BEC			10^{6}

BEC Apparatus

"Jila I" ~ 1/95- 11/96 (RIP Smithsonian)

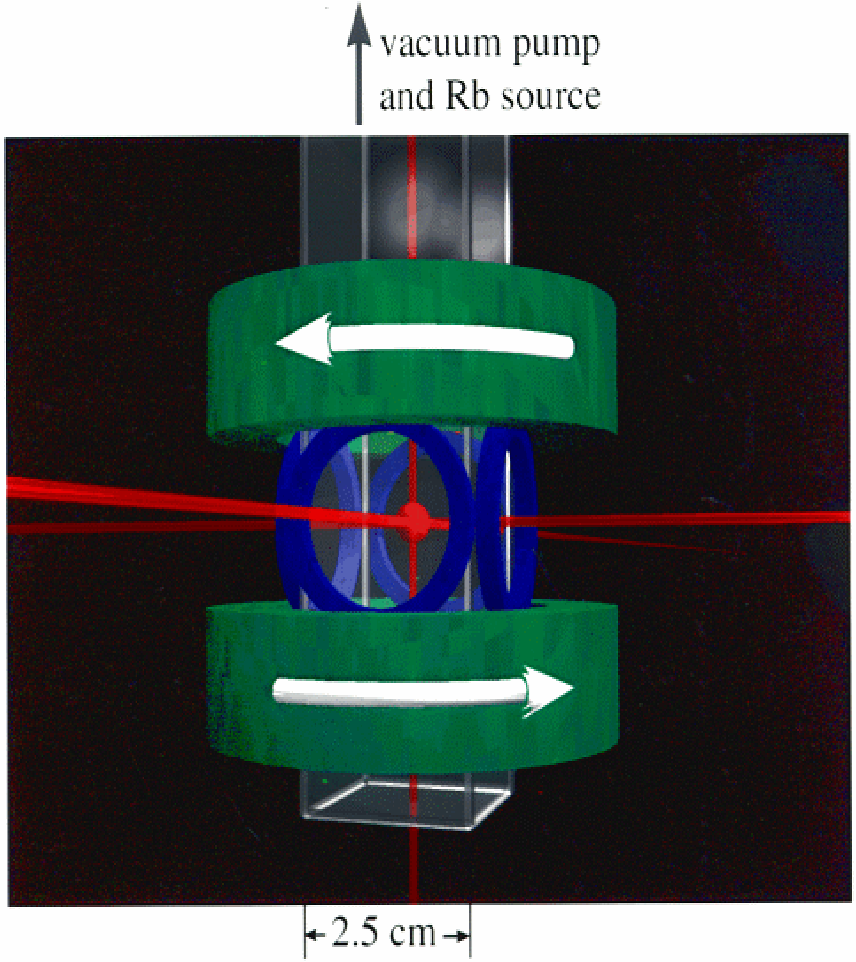

Cheap diode lasers

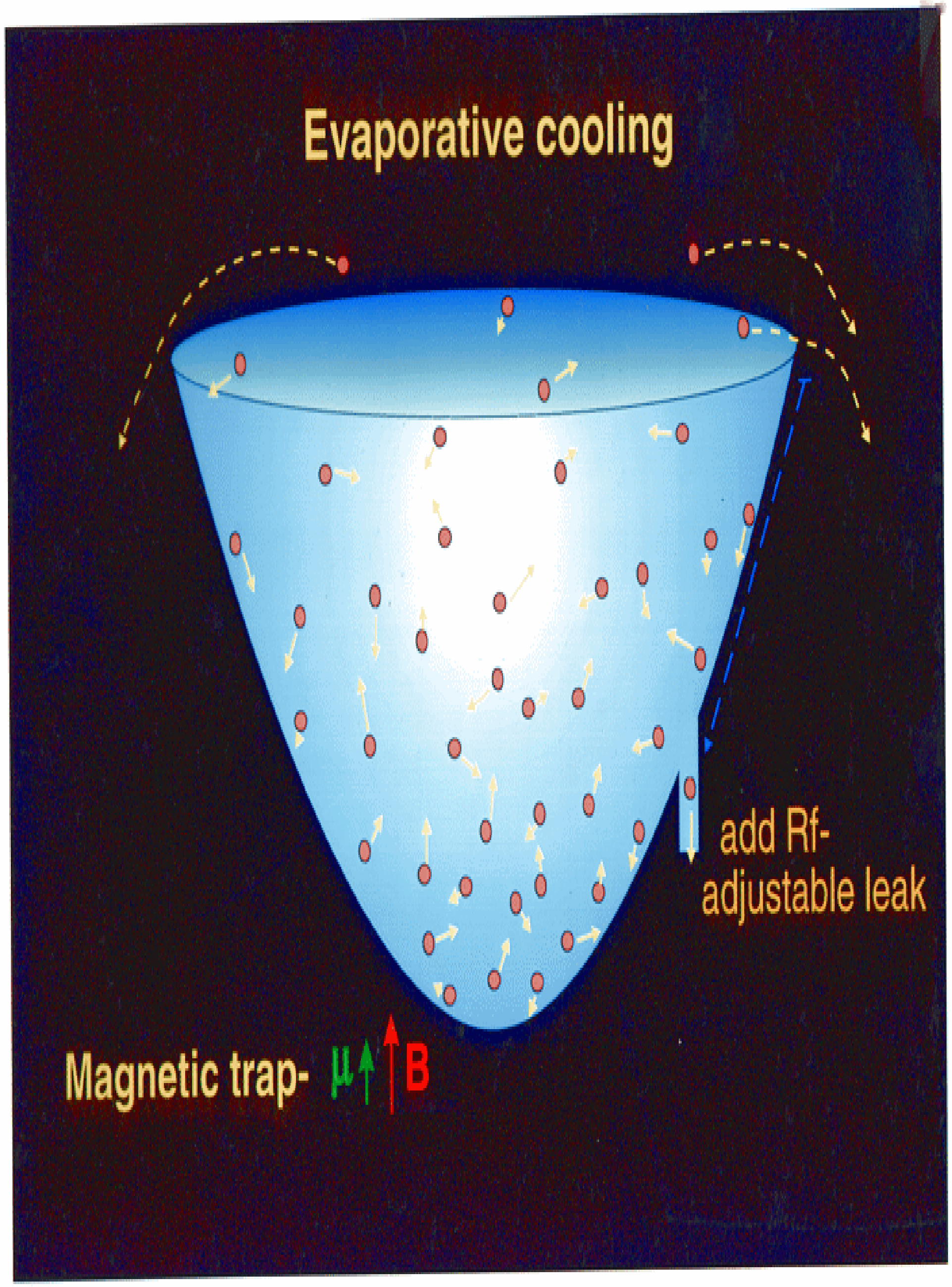

Observing condensate

1. Expand cloud.
2. “Shadow snapshot”.

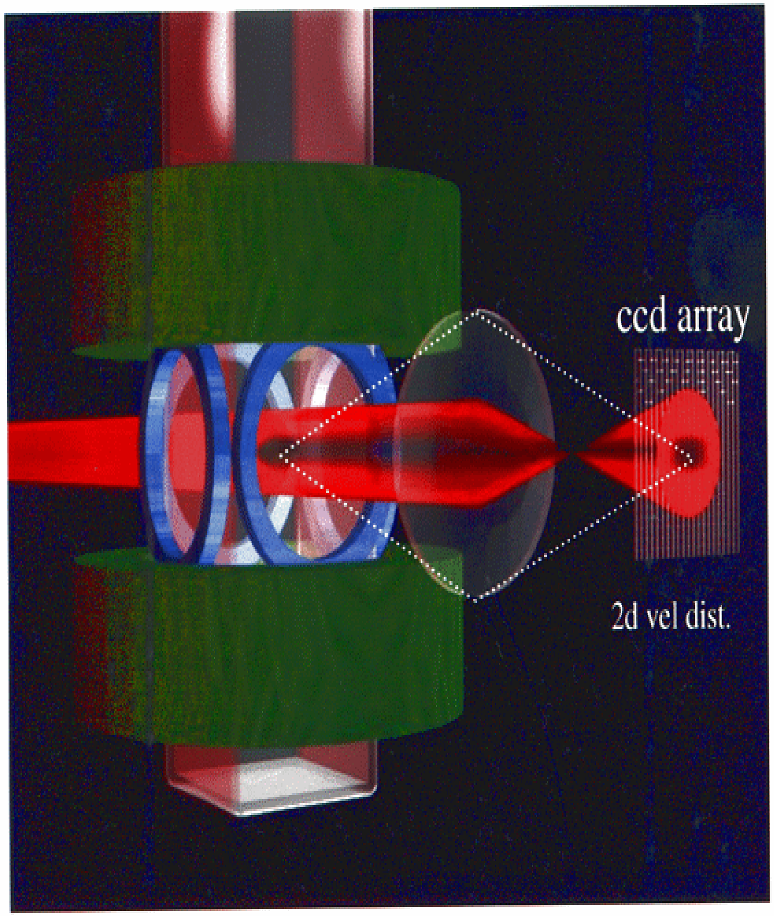

Destroys condensate

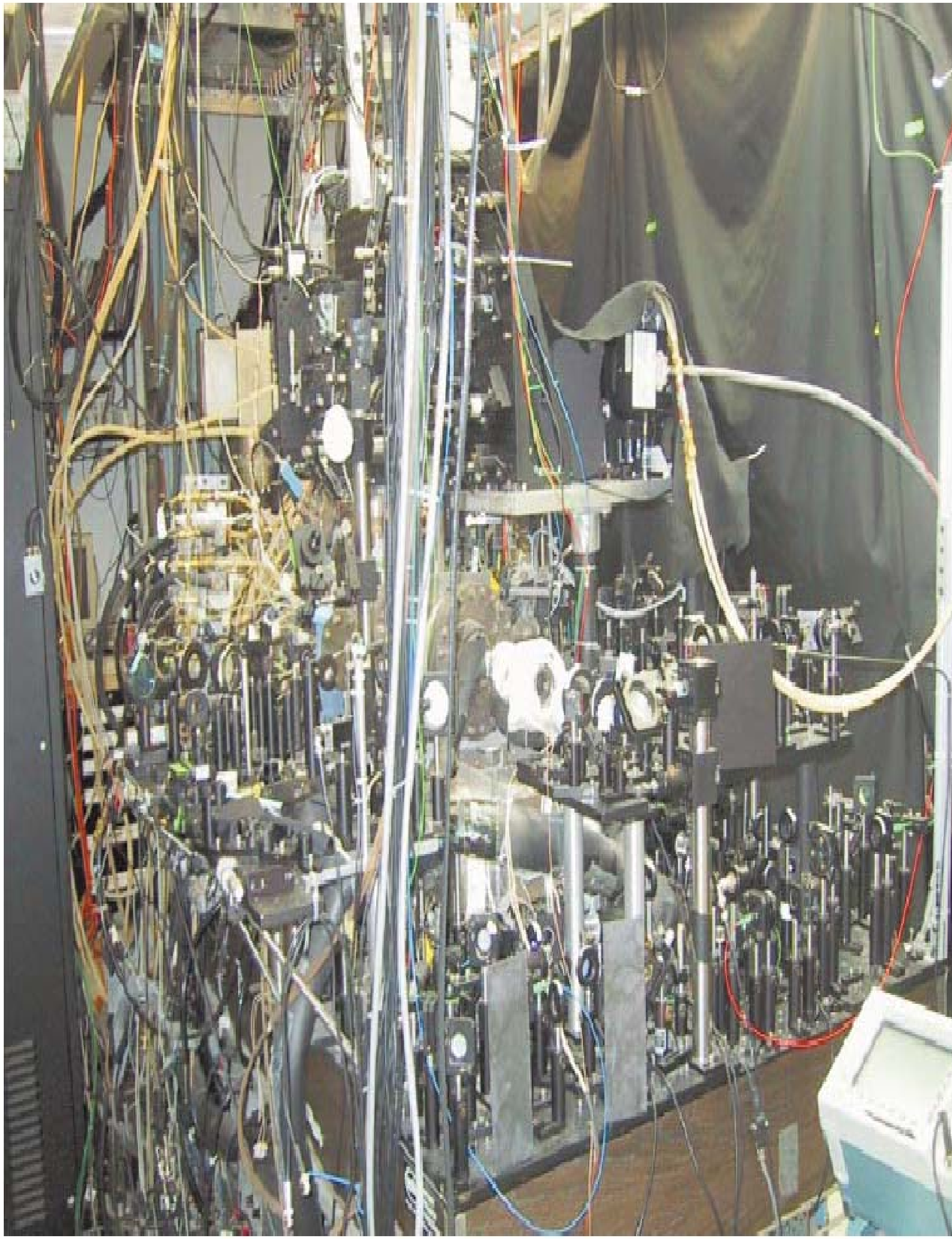

FIG. 11. (*Continued.*)

C. E. Wieman and E. A. Cornell, Science 269, 198 (1995).

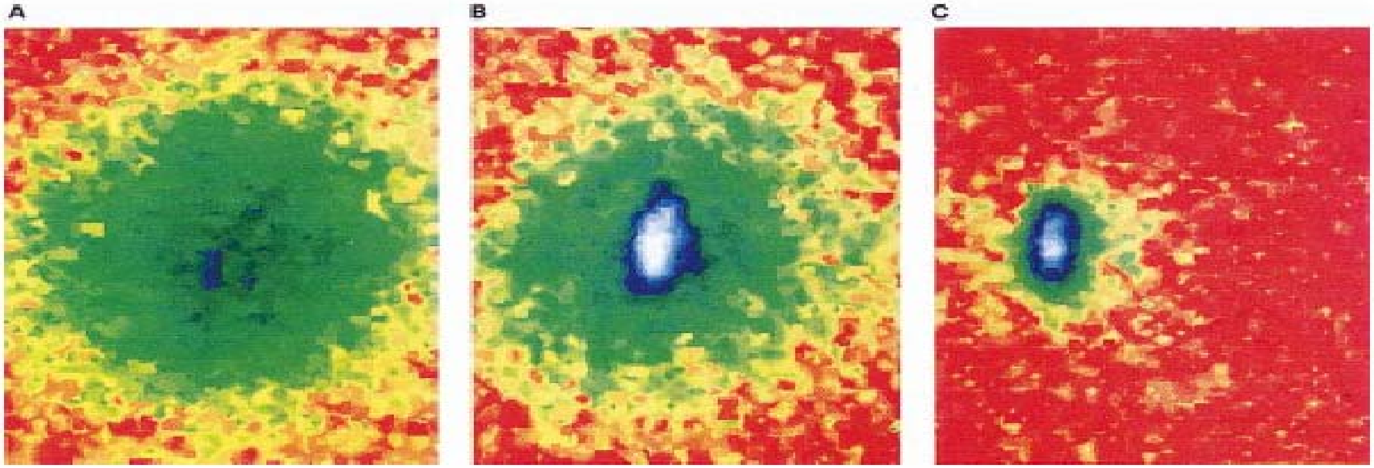

FIG. 8. Looking down on the three images of Figure 7 (Anderson *et al.*, 1995). The condensate in B and C is clearly elliptical in shape [Color].

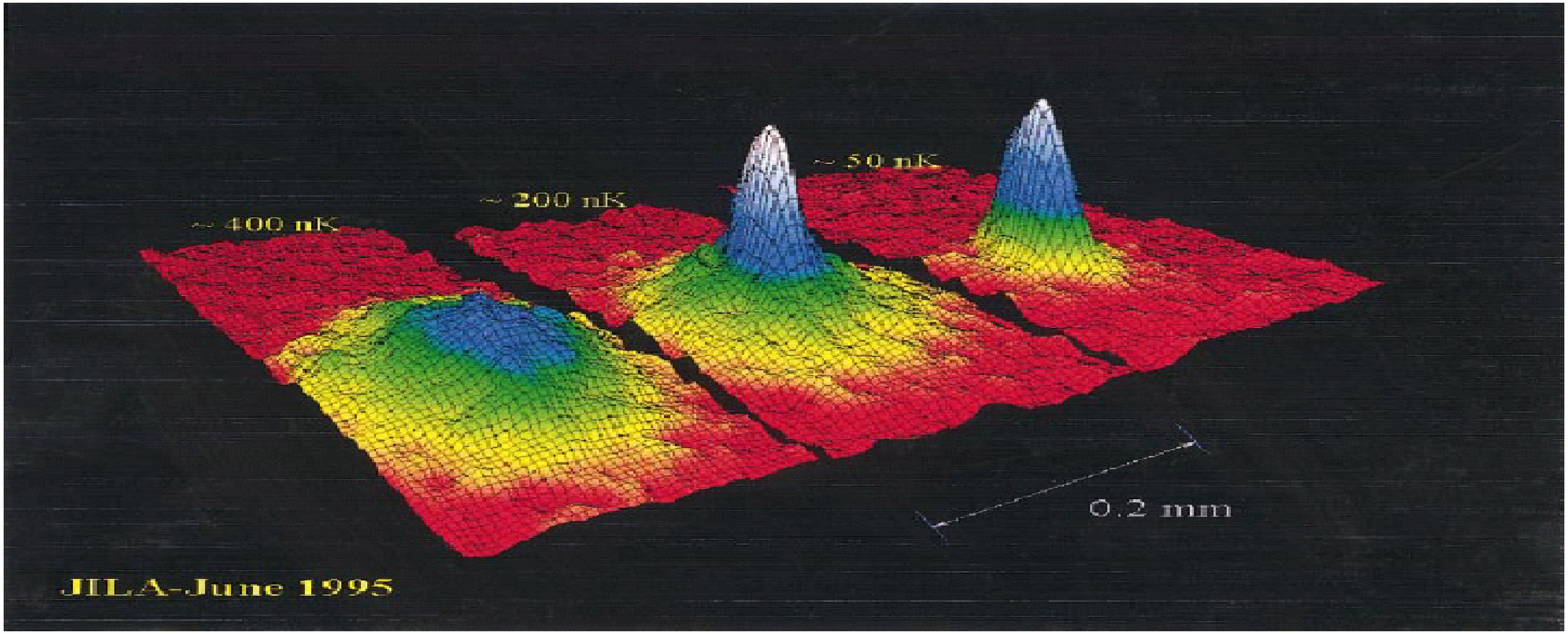

FIG. 7. Three density distributions of the expanded clouds of rubidium atoms at three different temperatures. The appearance the condensate is apparent as the narrow feature in the middle image. On the far right, nearly all the atoms in the sample are the condensate. The original experimental data were two-dimensional black and white shadow images, but these images have be

Photo: Ken Abbott, University of Colorado at Boulder

Photo: Volker Steger

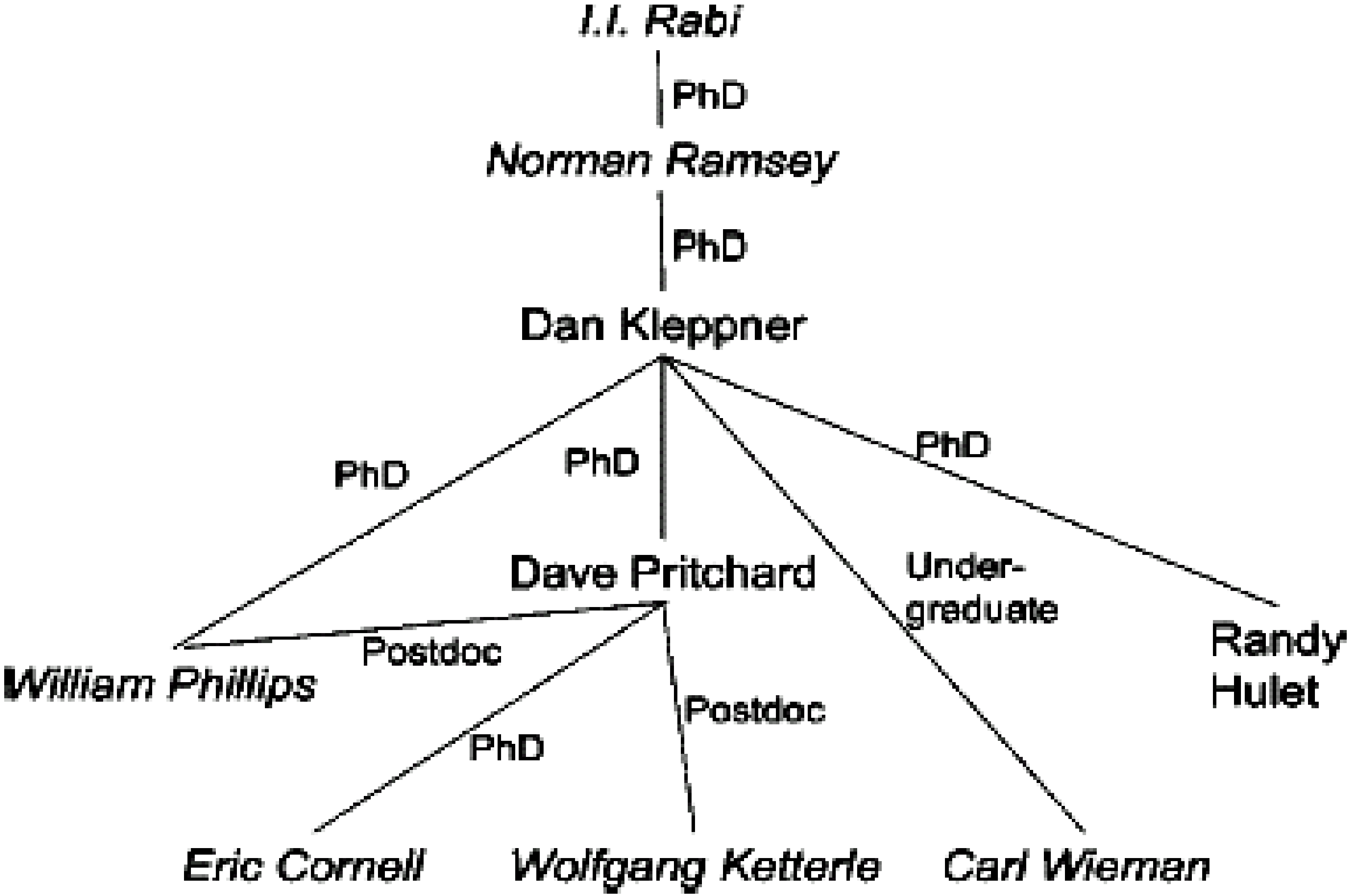

FIG. 10. Family tree of atomic physicists. People with names in italics are Nobel laureates.

FIG. 9. MIT faculty in ultralow-temperature atomic physics. Dan Kleppner, W.K., Tom Greytak, and Dave Pritchard look at the latest sodium BEC apparatus [Color].

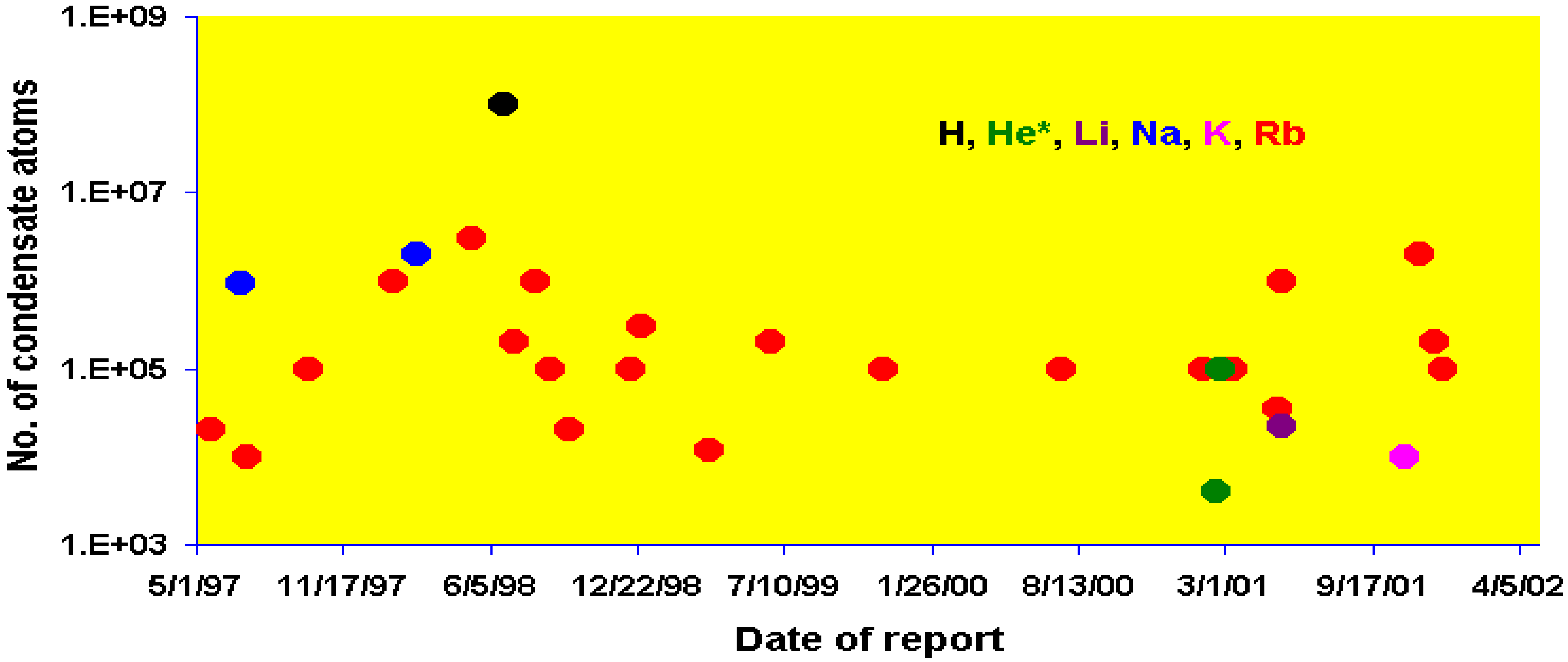

50 Lab.

- Elements： Li, Na, K, H, Rb, He, Fermi gases
- Trapping techniques: macroscopic chip (Nature 413, 498 (2001))
- Pure optics (Phys. Rev. Lett. 87, 010404 (2001))

  Sympathetic cooling (Phys. Rev. Lett. 87, 080403 (2001))
- Y.Z. Wang, Y.Q. Wang, BEC in China, March 2002, Shanghai, China

2. Superfluidity

2.1. Coherence

W. Ketterle, Science 275, 637 (1997).

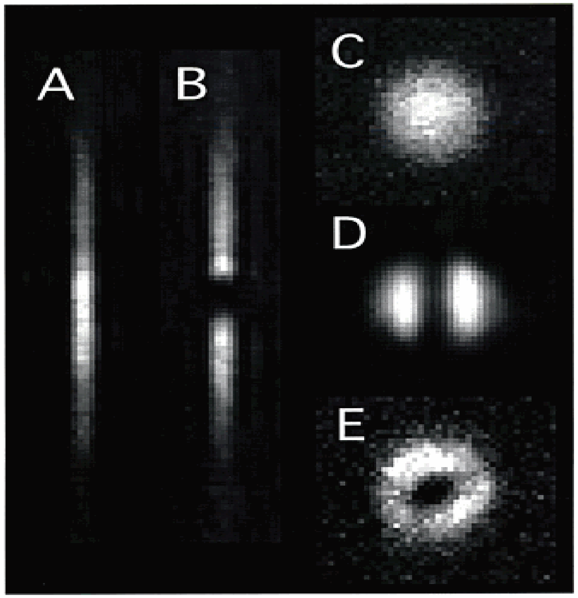

Shaping condensates with magnetic Fields and (Far off-resonant) light

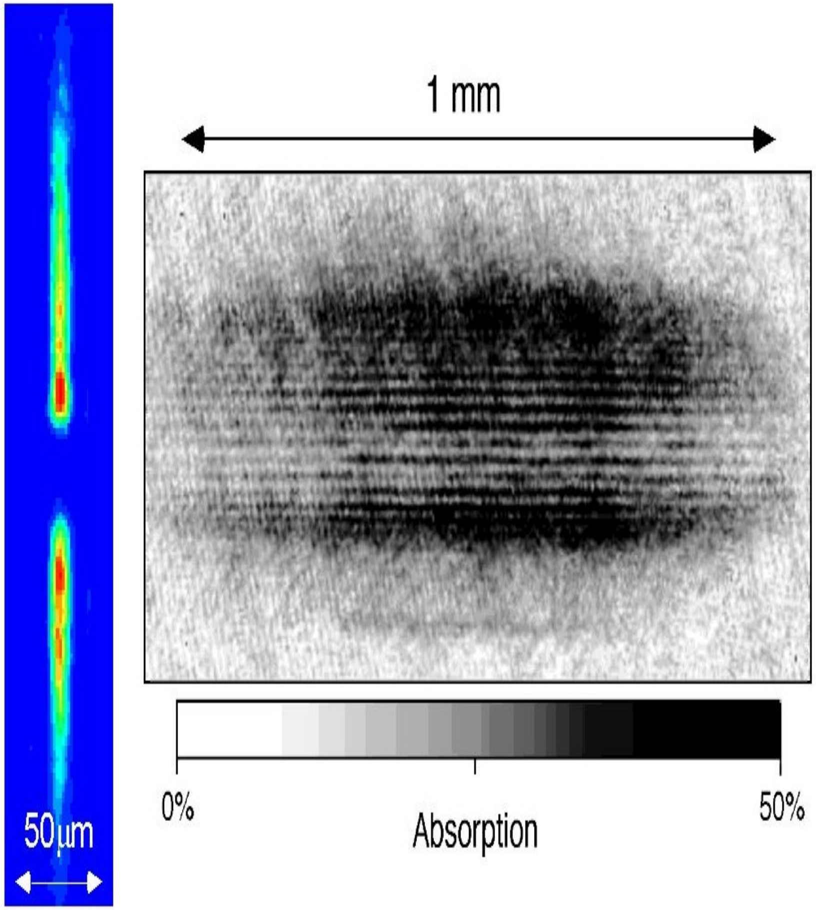

The Nobel Prize in Physics 2001

◀◀ BACK ▶▶

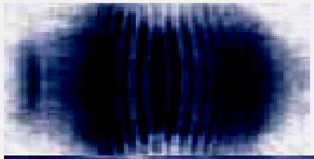

To the left, Ketterle's first interference pattern.

The interference pattern between two expanding condensates resembles that formed by throwing two stones into still water.

Large condensates and interference patterns

Wolfgang Ketterle came to the Massachusetts Institute of Technology (MIT) in 1990. He worked with a different alkali atom, sodium, and published his BEC results four months after Cornell and Wieman, but with a condensate containing some hundreds of times more atoms. In an interference experiment he showed that all the atoms really were linked in a single wave of matter. By first separating a condensate into two parts and then causing these to expand into each other, he could observe distinct interference patterns – rather like what happens when two stones are thrown into still water at the same time. The interference pattern would not have formed unless the matter waves were coherent.

Contents:

Based on materials from the 2001 Nobel Poster for Physics

Web Adapted Version of the Nobel Poster from the Royal Swedish Academy of Sciences

Last modified January 14, 2004

W.M. Liu, B. Wu, Q. Niu,

Nonlinear effects in interference of Bose-Einstein condensates,

Phys. Rev. Lett. 84, 2294 (2000).

（SCI 引用 121 次）

Many-body Hamiltonian

$$\begin{aligned} H &= \int dr\, \Psi^{+}(r)\left[-\frac{\hbar^{2}}{2m}\nabla^{2}+V_{ext}\right]\Psi(r) \\ &\quad + \frac{1}{2}\int dr dr'\, \Psi^{+}(r)\Psi^{+}(r')V(r-r')\Psi(r')\Psi(r) \end{aligned}$$

The mean field theory

$$\Psi(r,t)=\Phi(r,t)+\tilde{\Psi}'(r,t)$$

Gross-Pitaevskii equation

$$i\hbar\frac{\partial}{\partial t}\Phi(r,t)=\left(-\frac{\hbar^{2}\nabla^{2}}{2m}+V_{ext}(r)+\frac{4\pi\hbar^{2}a}{m}\left|\Phi\right|^{2}\right)\Phi(r,t)$$

Gross-Pitaevskii equation

$$i\hbar\frac{\partial}{\partial t}\Phi = \left(-\frac{\hbar^2\nabla^2}{2m} + V_{ext}(r) + \frac{4\pi\hbar^2 a}{m}|\Phi|^2\right)\Phi$$

Long time solution

$$\Phi(x,t) = \frac{\alpha\left(\frac{x}{t}\right)}{\sqrt{t}} e^{i\frac{x^2}{2t} - i2\left|\alpha\left(\frac{x}{t}\right)\right|^2 \log(4t)} + O\left(t^{-1}\log t\right)$$

$$|\alpha(k)|^2 = -\frac{1}{2\pi g}\log\left(1-|r(k)|^2\right)$$

Theoretical explanation

Fringe position

$$k_{\pm n} = \pm 2\sqrt{E_n} = \pm 2\left[V_0 + \left(n - \frac{1}{2}\right)\sqrt{2V_0''}\right]^{1/2}$$

Central fringe

$$\Delta k_0 = k_1 - k_{-1} = 4\left(V_0 + \sqrt{V_0''/2}\right)^{1/2}$$

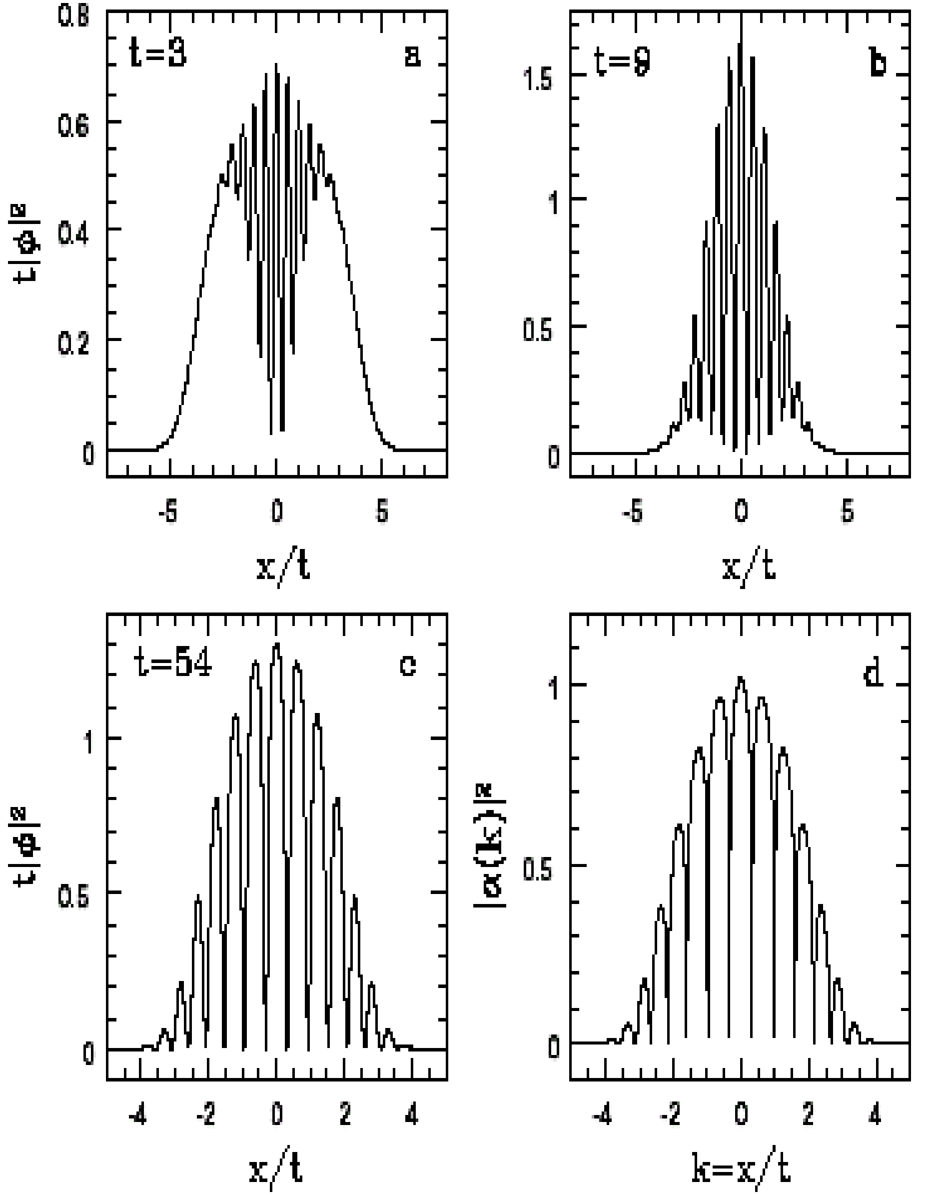

FIG. 1. Evolution of two BECs ($g = 2, d_0 = 12, \sigma = 1$). The scaled packets at (a) $t = 3$, (b) $t = 9$, and (c) $t = 54$. (d) $|\alpha(k)|^2$ in Eq. (4).

Experimental prediction:

1. Energy level 2. Many wave packets

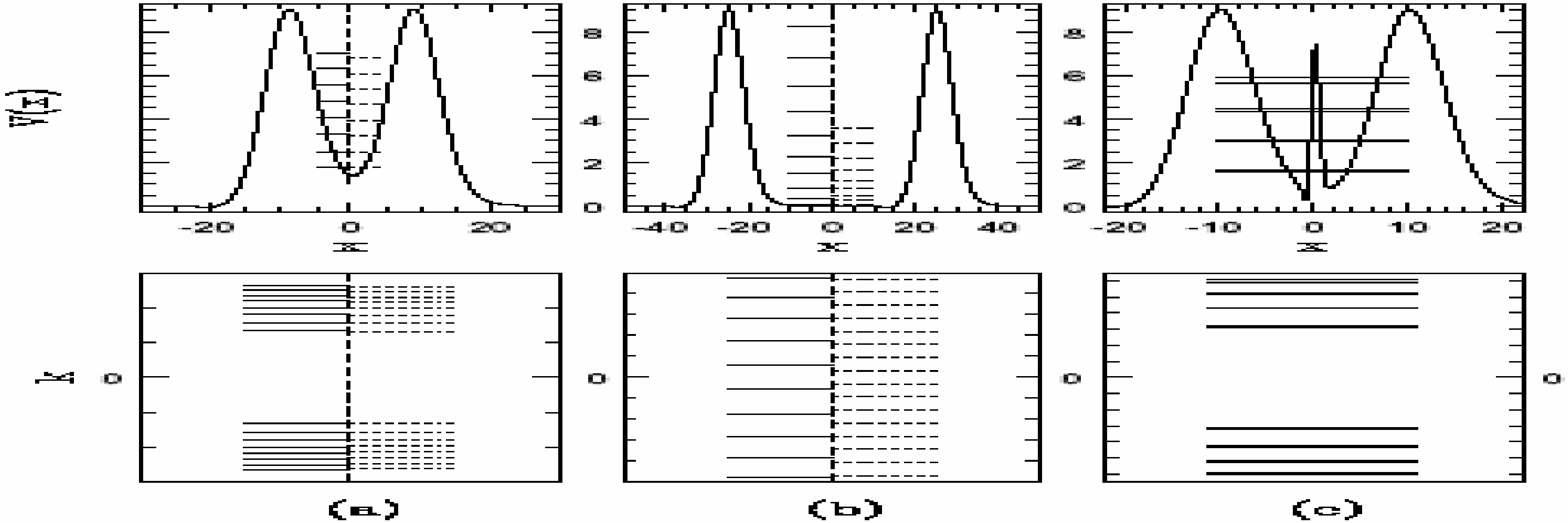

FIG. 2. The potentials, the energy levels, and the levels in k. Two Gaussian wave packets with (a) small separation, (b) large separation, and (c) three Gaussian wave packets. The solid level lines are accurate numerical results while the dotted lines are analytical results for comparison. Note that the energy levels in (b) are magnified by a factor of 10; the k level spacing is the fringe spacing or the interference band in the main text.

Ratio of level width to level spacing

$$\frac{\delta k_n}{\Delta k_n} = \frac{\delta E_n}{\Delta E_n} = 2e^{-2\sqrt{g-E_n}\,w(E_n)}$$

W.D. Li, X.J. Zhou, Y.Q. Wang, J.Q. Liang, W.M. Liu,

Time evolution of relative phase in two-component Bose-Einstein condensates with a coupling drive,

Phys. Rev. A64, 015602 (2001).

（**SCI** 引用 **23** 次）

2.2. Josephson effect

M.A. Kasevich, Science 298, 1363 (2002).

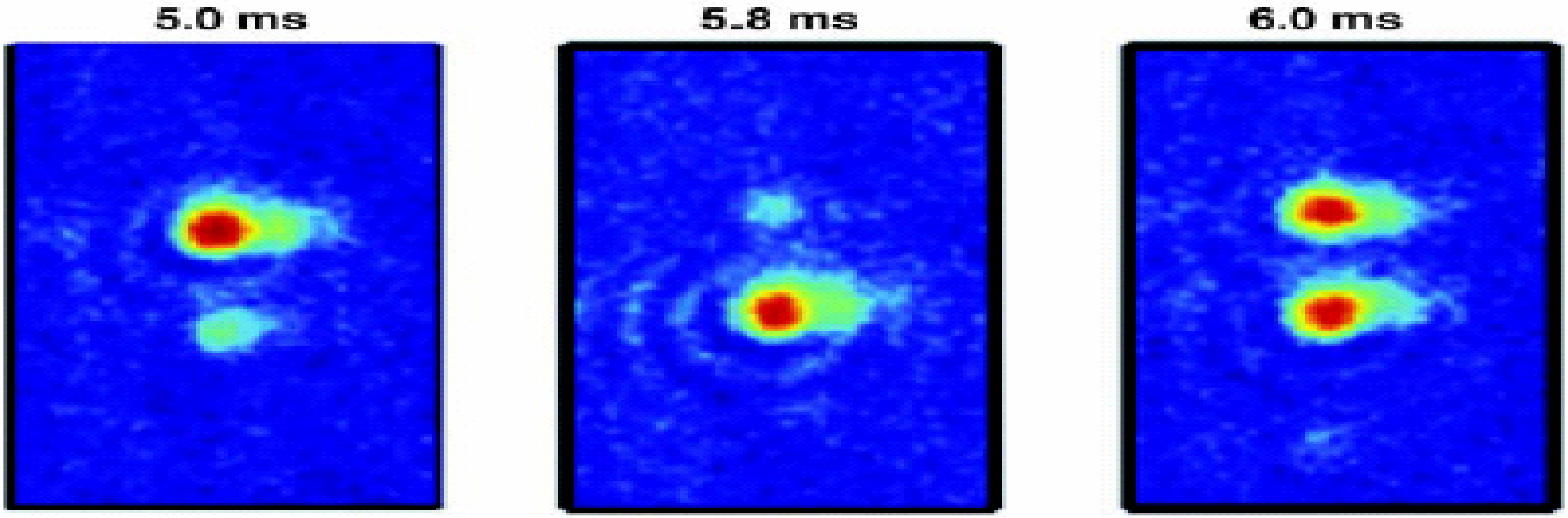

Fig. 6. AC Josephson effect in optical lattices, as observed through the interference profile of atoms suddenly released from a vertically oriented, one-dimensional optical lattice. The relative phase ϕ between adjacent wells evolves according to the Josephson relation $(h/2\pi)d\phi/dt = V$, where h is Planck's constant, t is time, and V is the chemical potential difference between adjacent wells. This evolution results in an oscillation of the populations of diffraction lobes in the interference signals. In this work, V is determined by gravity. The time label references the time interval that the atoms were held in the combined gravitational plus optical lattice potential before being released and imaged.

Quantum tunneling

W.M. Liu, W.B. Fan, W.M. Zheng, J.Q. Liang, S.T. Chui,

**Quantum tunneling of
Bose-Einstein condensates
in optical lattices under gravity,**

**Phys. Rev. Lett. 88, 170408 (2002).
（SCI 引用 92 次）**

Potential energy and Bloch bands

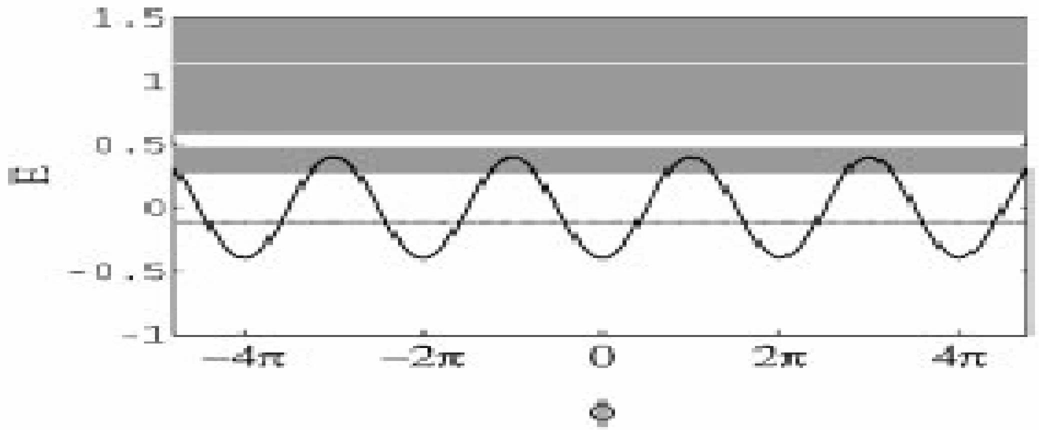

FIG. 1. Potential energy $V_0 \cos\phi$ and the Bloch bands for $V_0 = 0.4$.

Landau-Zener tunneling

- Barrier between lattices is low
- Localized level between lattices is coupling
- Miniband
- Adiabatic approximation
- Tunneling between delocalized states in different Bloch bands

Tilted bands and WS ladders

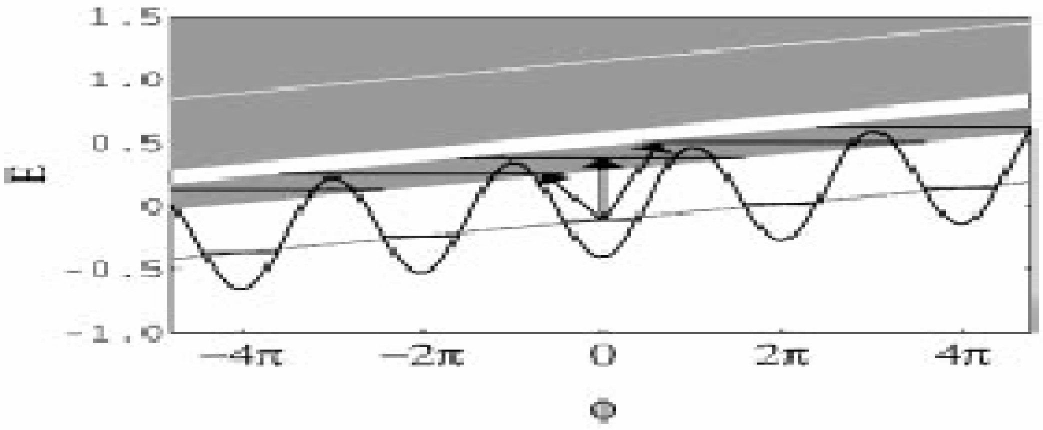

FIG. 3. Tilted bands and WS ladders for $V_0 = 0.4$ and $\alpha = 0.02$. Arrows indicate resonant excitations by an ac modulation of the acceleration.

Wannier-Stark tunneling

- An external field
- Wavefunction of miniband is localization
- Miniband is divided into discrete level
- Wannier-Stark ladder
- Tunneling between localized states in different individual wells—Wannier-Stark localized states

Temperature dependence

$$\Gamma(T) = \Gamma_0 \left(1 - e^{-\frac{\hbar w_0}{k_B T}}\right) e^{\frac{432 V_{\max}}{\hbar w_0} e^{-\frac{\hbar w_0}{k_B T}}}$$

At high temperature:

Arrhenius law

$$\Gamma_{AR} = \frac{\omega_0}{2\pi} e^{-V_{\max}/k_B T}$$

At intermediate temperature:
Thermally assisted tunneling

$$T_{cr} = \frac{hw_0}{2\pi k_B}$$

Crossover temperature

$$T_{cr} = 257nK$$

$$U_l(x, y) = 2.1E_R$$

At low temperature:
Pure quantum tunneling

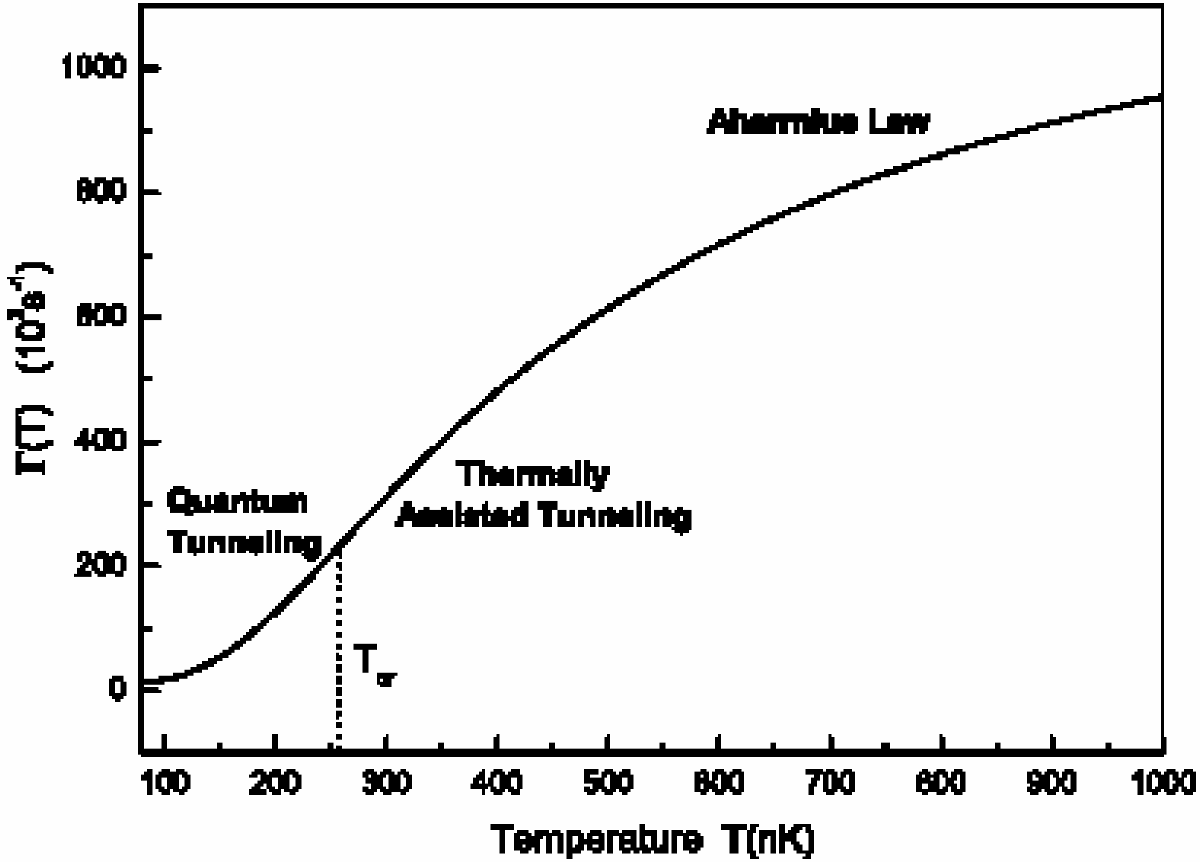

FIG. 1. The temperature dependence of the decay rate $\Gamma(T)$ for ^{87}Rb atoms with Yale experimental parameters $\lambda = 850$ nm, $U_l(x,y) = 2.1E_R$, where $E_R = \frac{2\pi^2\hbar^2}{m\lambda^2}$ is the recoil energy.

2.3. Soliton

L. Khaykovich et al., Science 296, 1290 (2002).

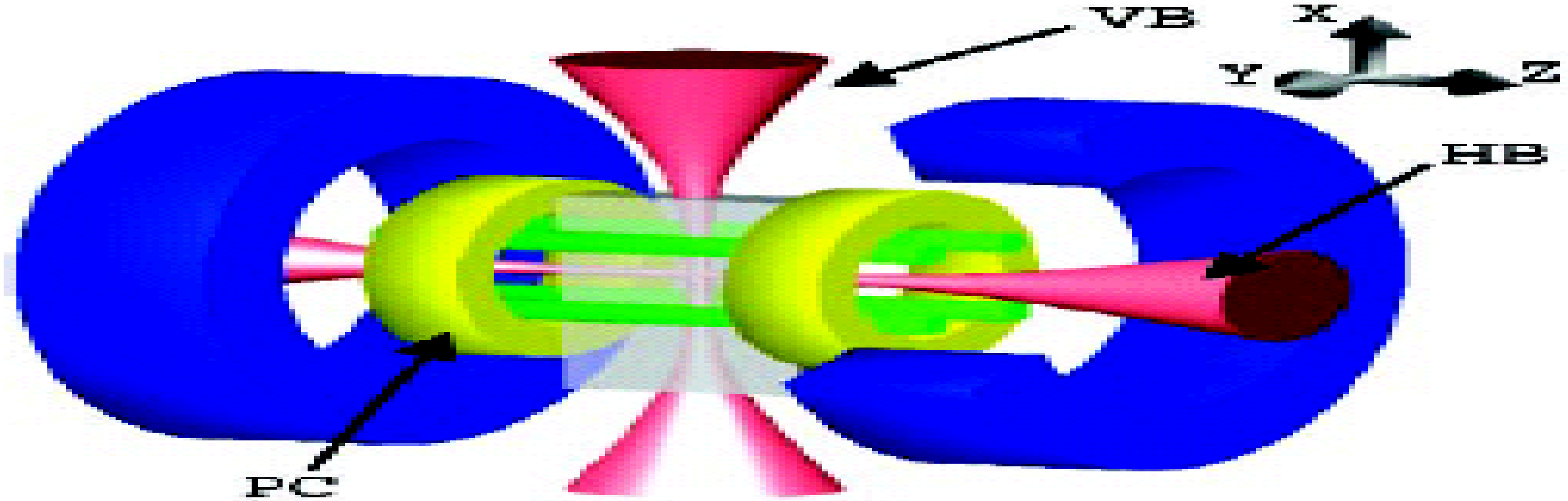

Fig. 1. Experimental setup for soliton production. ^{7}Li atoms are evaporatively cooled in a Ioffe-Pritchard magnetic trap and transferred into a crossed optical dipole trap in state $|F = 1, m_F = 1\rangle$ where they Bose condense. Magnetic tuning of the scattering length to positive, zero, and negative values is performed with the two pinch coils (PC). Switching-off the vertical trapping beam (VB) allows propagation of a soliton in the horizontal 1D waveguide (HB). Absorption images of solitons and BECs are recorded on a charge-coupled device camera in the x, z plane.

L. Khaykovich et al., Science 296, 1290 (2002).

Fig. 3. Absorption images at variable delays after switching off the vertical trapping beam. Propagation of an ideal BEC gas (**A**) and of a soliton (**B**) in the horizontal 1D waveguide in the presence of an expulsive potential. Propagation without dispersion over 1.1 mm is a clear signature of a soliton. Corresponding axial profiles are integrated over the vertical direction.

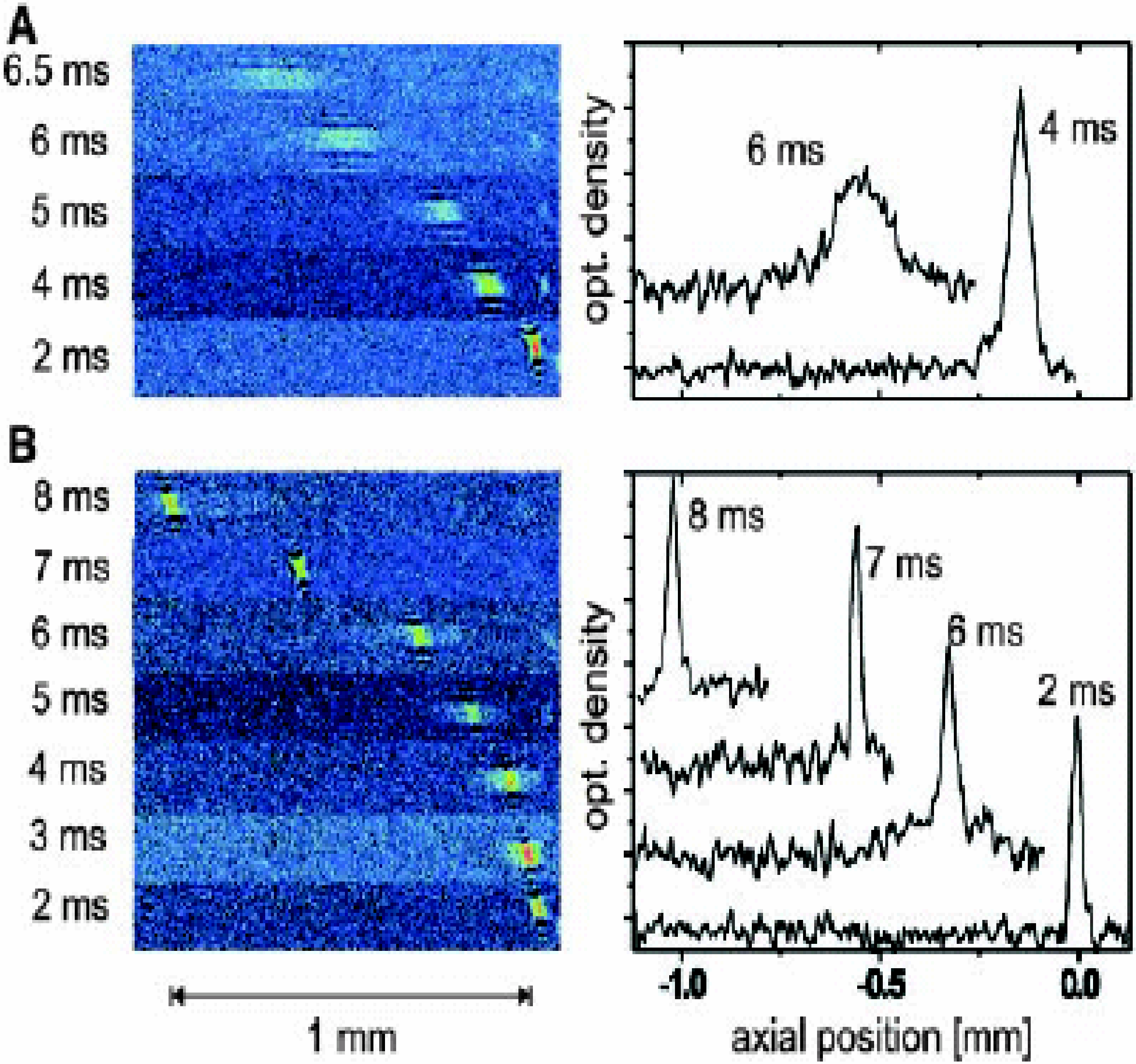

Z.W. Xie, Z.X. Cao, E.I. Kats, W.M. Liu,

Nonlinear dynamics
of dipolar Bose-Einstein condensate
in optical lattice,

Phys. Rev. A 71, 025601 (2005).

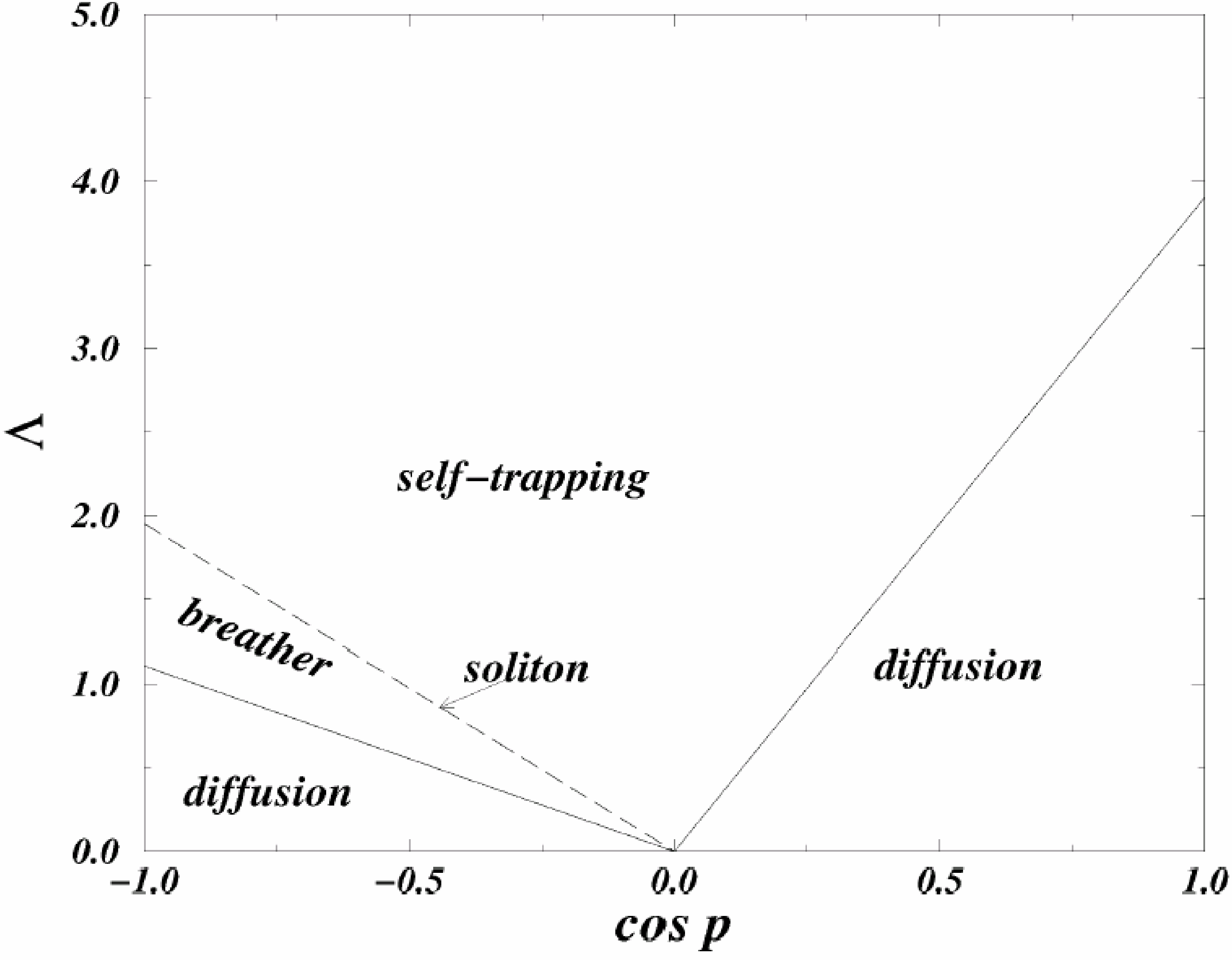

5.0
4.0
3.0
2.0
1.0
0.0
Λ
self−trapping
breather
soliton
diffusion
diffusion
−1.0
−0.5
0.0
0.5
1.0
cos p

L. Li, B.A. Malomed, D. Mihalache, W.M. Liu,

Exact soliton-on-plane-wave solutions for two-component Bose-Einstein condensates,

Phys. Rev. E 73, 066610 (2006).

2.4. Vortex and Abrikosov lattices

J. R. Abo-Shaeer et al., Science 292, 476 (2001).

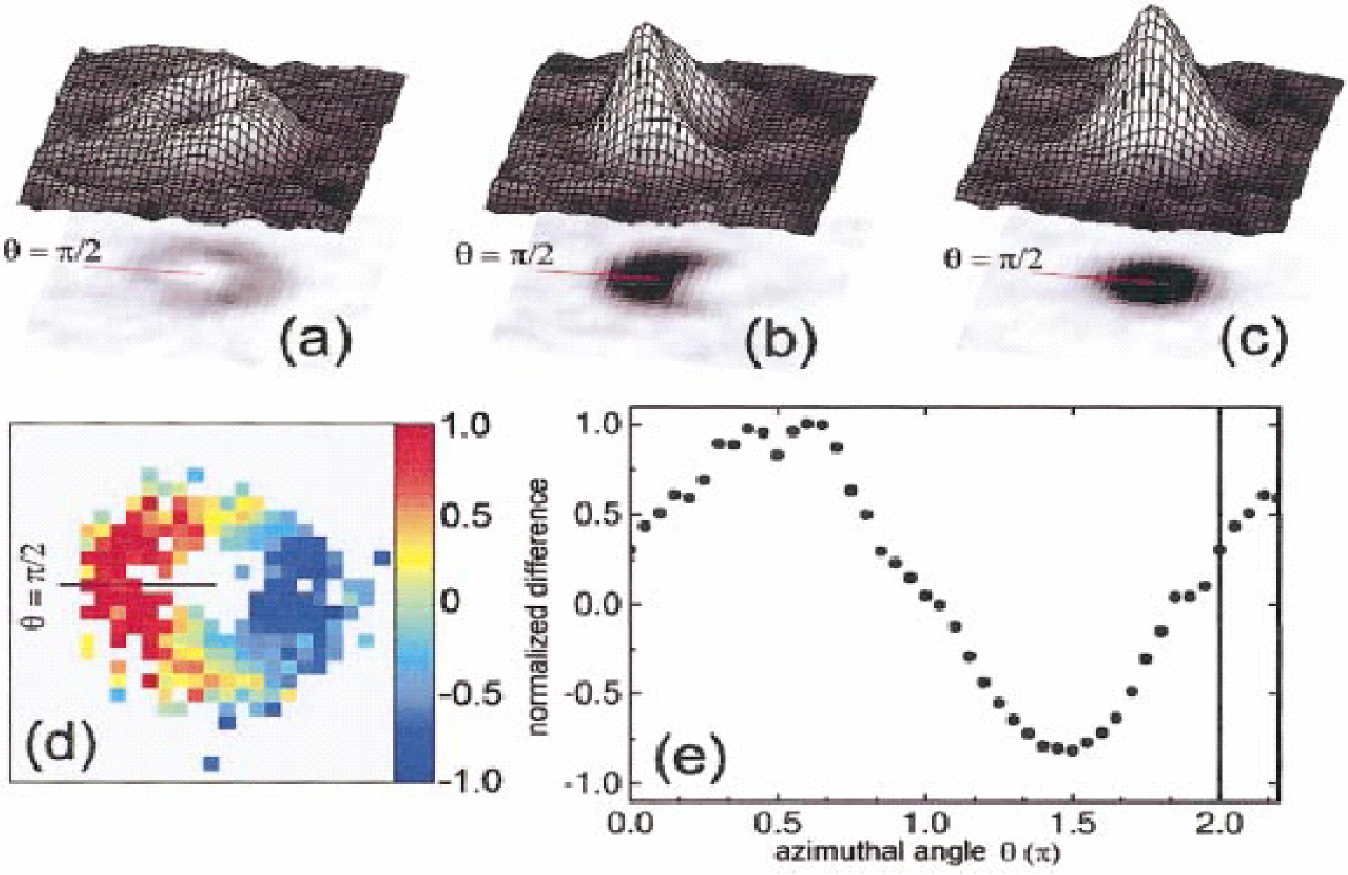

FIG. 11. Condensate images showing the first BEC vortex and the measurement of its phase as a function of azimuthal angle: (a) the density distribution of atoms in the upper hyperfine state after atoms have been put in that state in a way that forms a vortex; (b) the same state after a pi/2 pulse has been applied that mixes upper and lower hyperfine states to give an interferogram reflecting the phase distribution of the upper state; (c) residual condensate in the lower hyperfine state from which the vortex was formed that interferes with a to give the image shown in (b); (d) a color map of the phase difference reflected in (b); (e) radial average at each angle around the ring in (d). The data are repeated after the azimuthal angle 2π to better show the continuity around the ring. This shows that the cloud shown in (a) has the 2π phase winding expected for a quantum vortex with one unit of angular momentum. From Matthews *et al.*, 1999a [Color].

Superfluidity

L. Pitaevskii et al., Science 298, 2144 (2002).

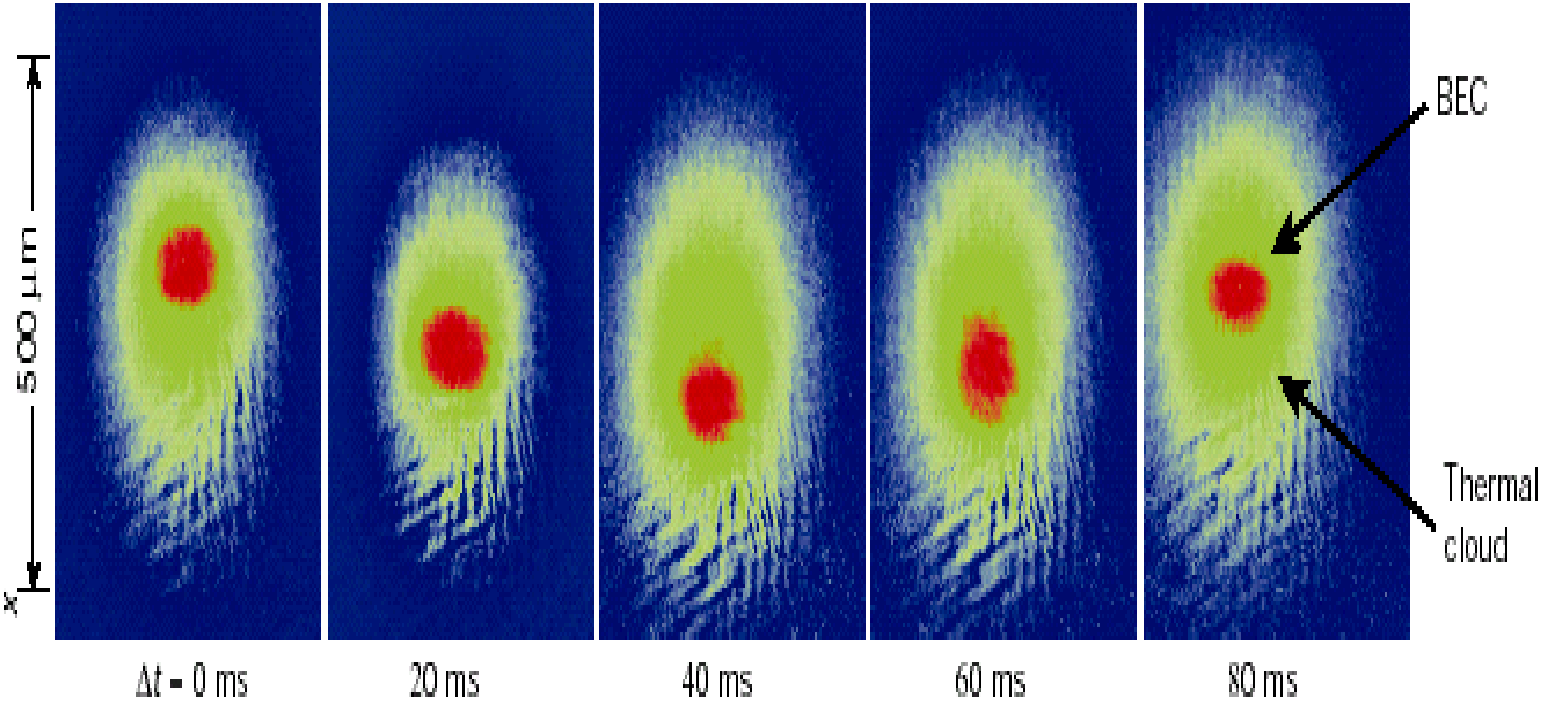

Figure 4 Signature of superfluidity in a Bose-condensed cloud[63]. The condensate and its thermal 'halo' of normal gas respond differently when they are dragged through a periodic potential. In the experiment, the clouds were displaced in a magnetic trap superimposed by an optical lattice. The condensate, distinguished by its much higher density (colour coded in red), tunnelled through the potential peaks and oscillated in the magnetic trapping potential, whereas the normal fraction was pinned by the optical lattice. Interaction between the two clouds eventually led to damping of the condensate motion.

3. Quantum phase transition

Superfluid
Mott insulator

Insulator + disorder = Bose glass
Insulator + weak disorder = Anderson glass

Berezinskii–Kosterlitz–Thouless transation

M. Greiner et al., Nature 415, 39 (2002)

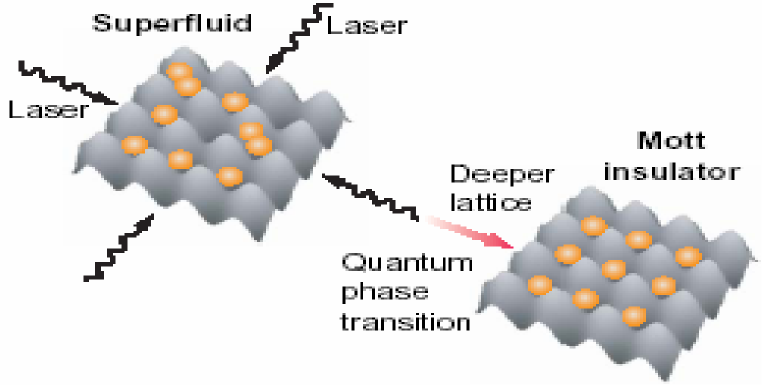

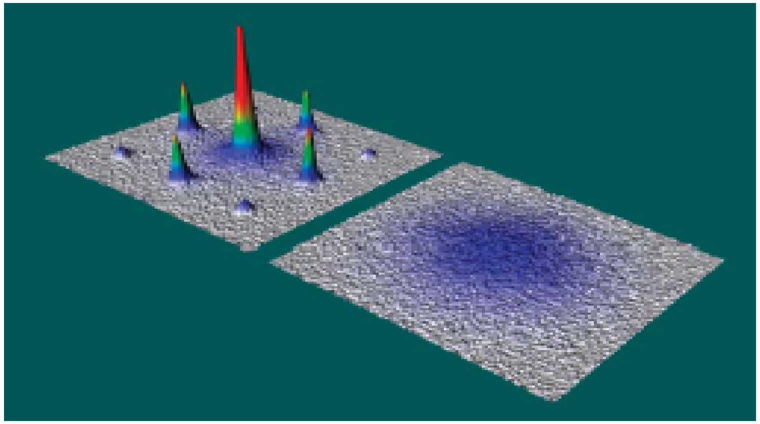

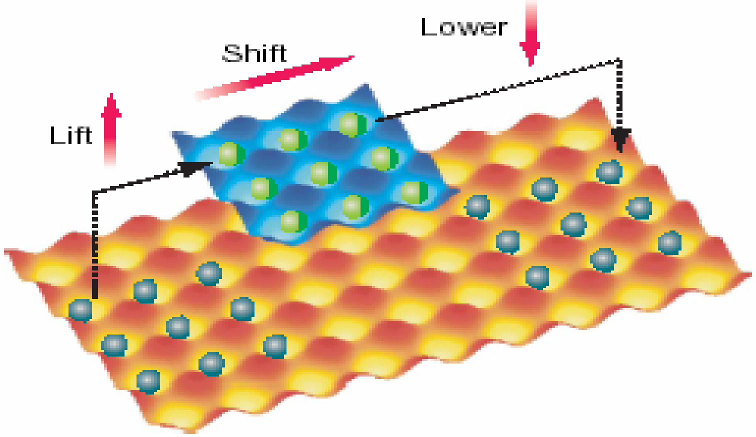

Cold atoms in optical lattices. (Top) Cold atoms in a periodic optical potential localize near the potential minima. The atoms can tunnel to neighboring sites with hopping amplitude J. Atoms on the same site repel each other according to the onsite interaction U. For weak lattices (J >> U), the atoms form a superfluid (BEC) with atoms delocalized over many lattice sites. With increasing laser intensity (J << U), the atoms form a Mott insulator state in which atoms are locked at individual lattice sites (*3*). **(Bottom)** Experimental signatures of the superfluid–Mott insulator transition (*4*). In the superfluid (rear), the atoms show an interference pattern, which disappears in the Mott phase (front). **(Right)** Entangling atoms in a lattice. Depending on their internal state, atoms collide with neighboring atoms when the potential holding atoms in one state is moved while the potential holding atoms in the other state is kept stationary (*11, 12*).

J.J. Liang, J.Q. Liang, W.M. Liu,

Quantum phase transition
of condensed bosons in optical lattices,

Phys. Rev. A68, 043605 (2003).

（**SCI** 引用 **32** 次）

Z.W. Xie, W.M. Liu,

Superfluid–Mott insulator transition of dipolar bosons in an optical lattice,

Phys. Rev. A70, 045602 (2004).

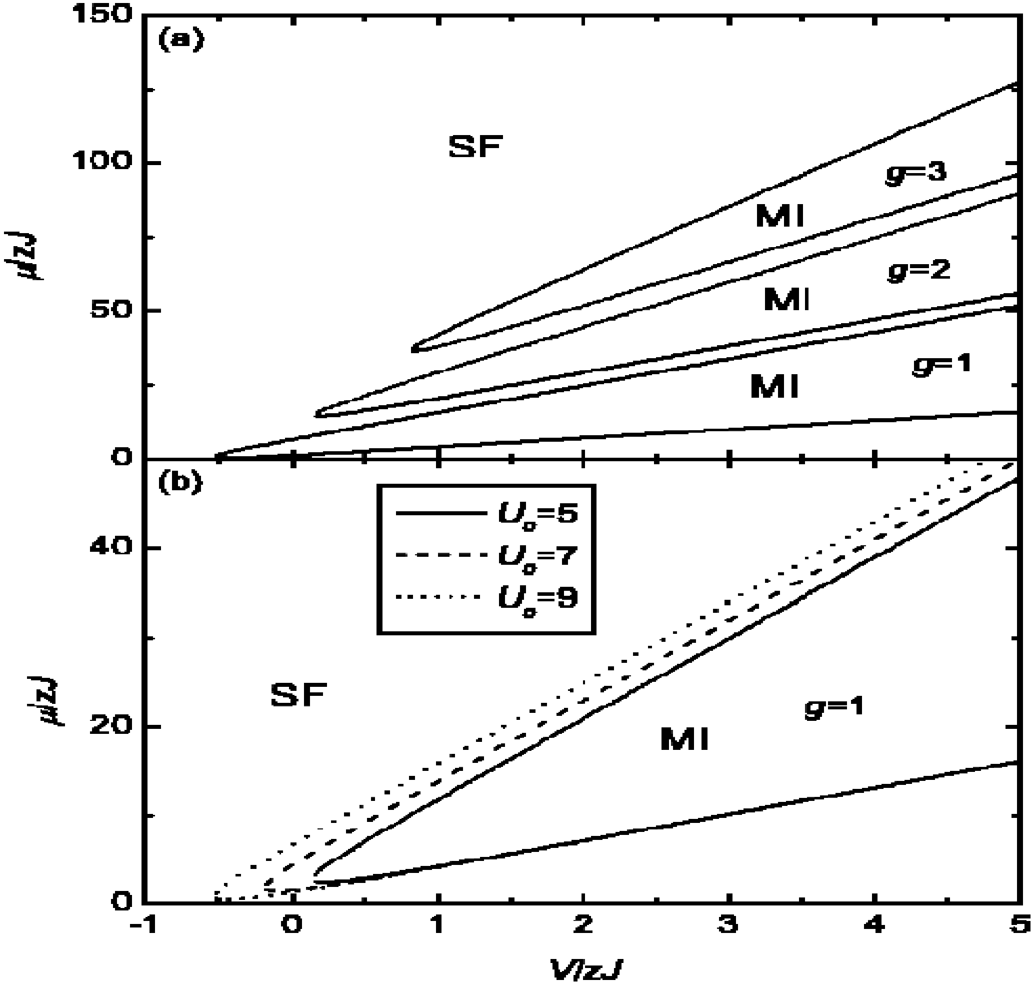

FIG. 1. Phase diagram of dipolar Bose-Hubbard model in an optical lattice with (a) $U_0=9$ and (b) different on-site energies U_0. The vertical axis shows the dimensionless chemical potential $\mu/zJ=\overline{\mu}$ and the horizontal axis shows the dimensionless dipole-dipole interaction $V/zJ=\overline{V}$. "SF" and "MF" mean "superfluid phase" and "Mott-insulator phase", respectively.

G.P. Zheng, J.Q. Liang, W.M. Liu,

Phase diagram of

two-species Bose-Einstein condensates

in an optical lattice，

Phys. Rev. A71, 053608 (2005)

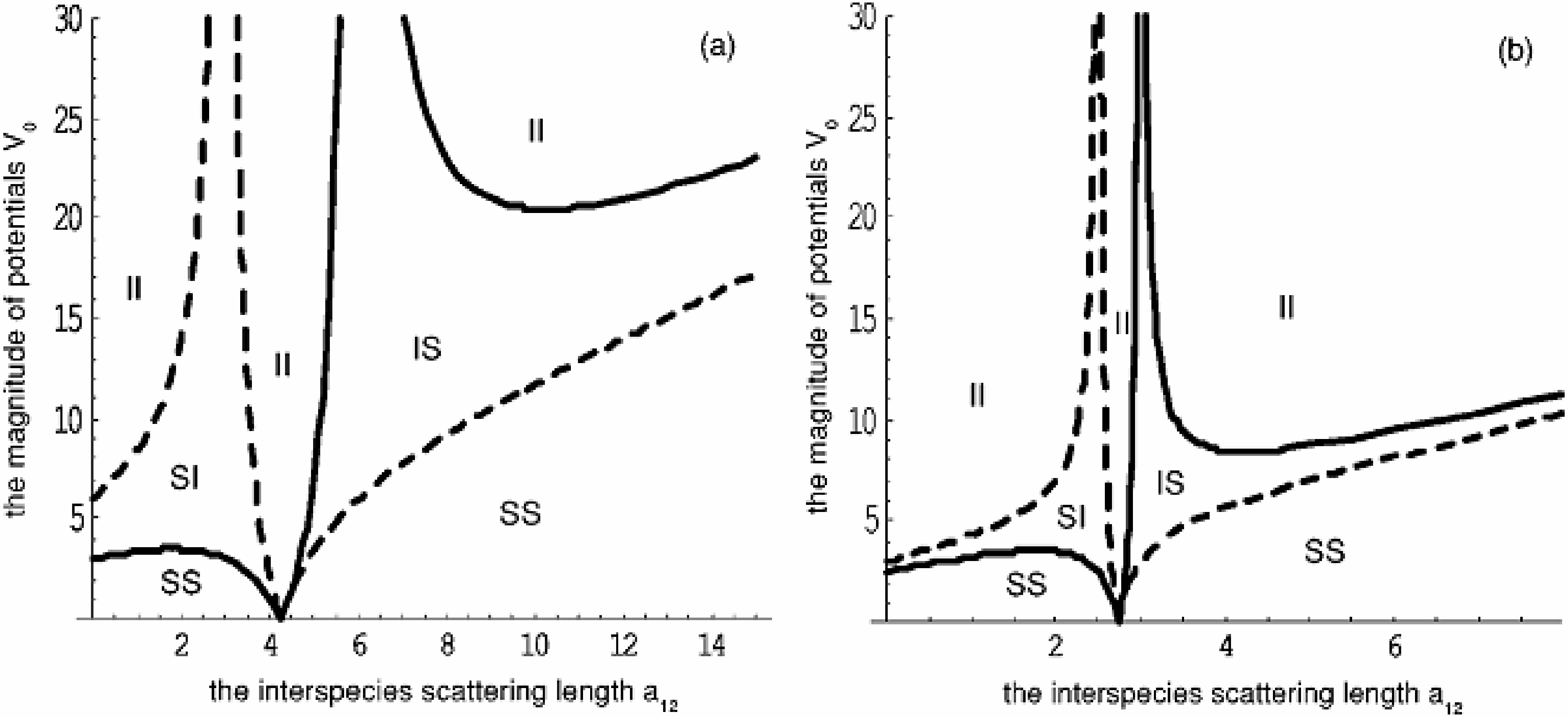

FIG. 1. Phase diagrams of two-species BECs in a 1D optical lattice. The magnitude of potentials V_0 is in units of $4n\hbar\omega_0$. The interspecies scattering length is in units of nm. Dashed curves: phase boundary of species 1; solid curves: phase boundary of species 2. The *s*-wave scattering lengths between the same species are as follows: (a) $a_1=6$ nm (^{87}Rb), $a_2=3$ nm (^{23}Na). (b) $a_1=3$ nm (hyperfine state $|f=1,m_f=1\rangle$ of ^{23}Na), $a_2=2.5$ nm (hyperfine state $|f=1,m_f=0\rangle$ of ^{23}Na).

P.B. He, Q. Sun, S.Q. Shen, W. M. Liu,

Magnetic quantum phase transition of cold atoms in optical lattice,

Phys. Rev. A 76, 043618 (2007).

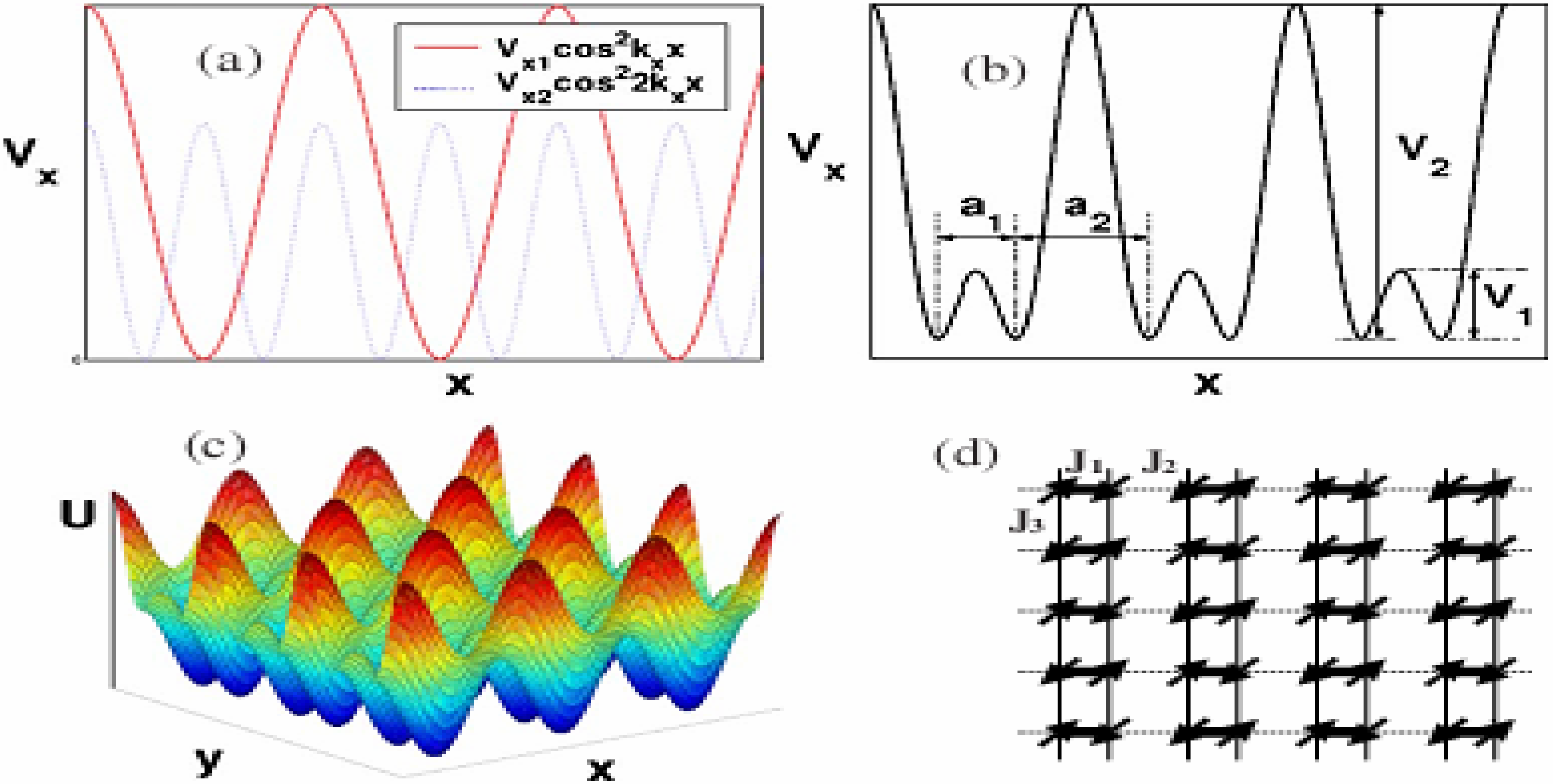

FIG. 1. (Color online) (a) Two selected optical potentials along the x direction, where the potential V_{x2} (dotted line) has twice the period of V_{x1} (solid line). (b) Total potential in the x axis, where a_1, a_2, V_1, and V_2 are the widths and heights of barriers of intradimers and interdimers, respectively. (c) Landscape of potential in the x-y plane. (d) Geometry of the 2D coupled spin ladders, where J_1, J_2, and J_3 are intradimer, interdimer, and interladder spin-spin couplings, respectively.

A.C. Ji, X.C. Xie, W. M. Liu,

Magnetic dynamics of polarized light in arrays of microcavities,

Phys. Rev. Lett. 99, 183602 (2007).

4. Strong correlated system

4.1. Strong interacting system

4.2. Strong correlated system

4.3. Quantum Hall effect

BEC near Feshbach resonance

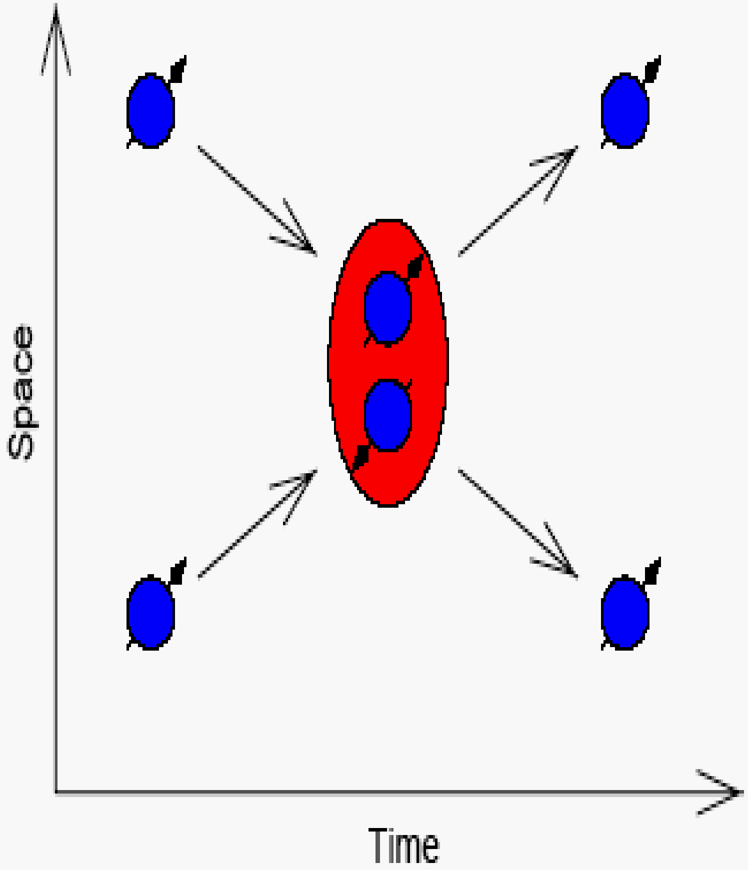

Fig. 1. Illustration of a Feshbach-resonant atomic collision. Two atoms, with a hyperfine state indicated by the arrow, collide and form a long-lived molecule with a different spin arrangement, which ultimately decays again into two atoms.

4.1. Strong interacting system

S. Inouye et al., Nature 392, 151 (1998).

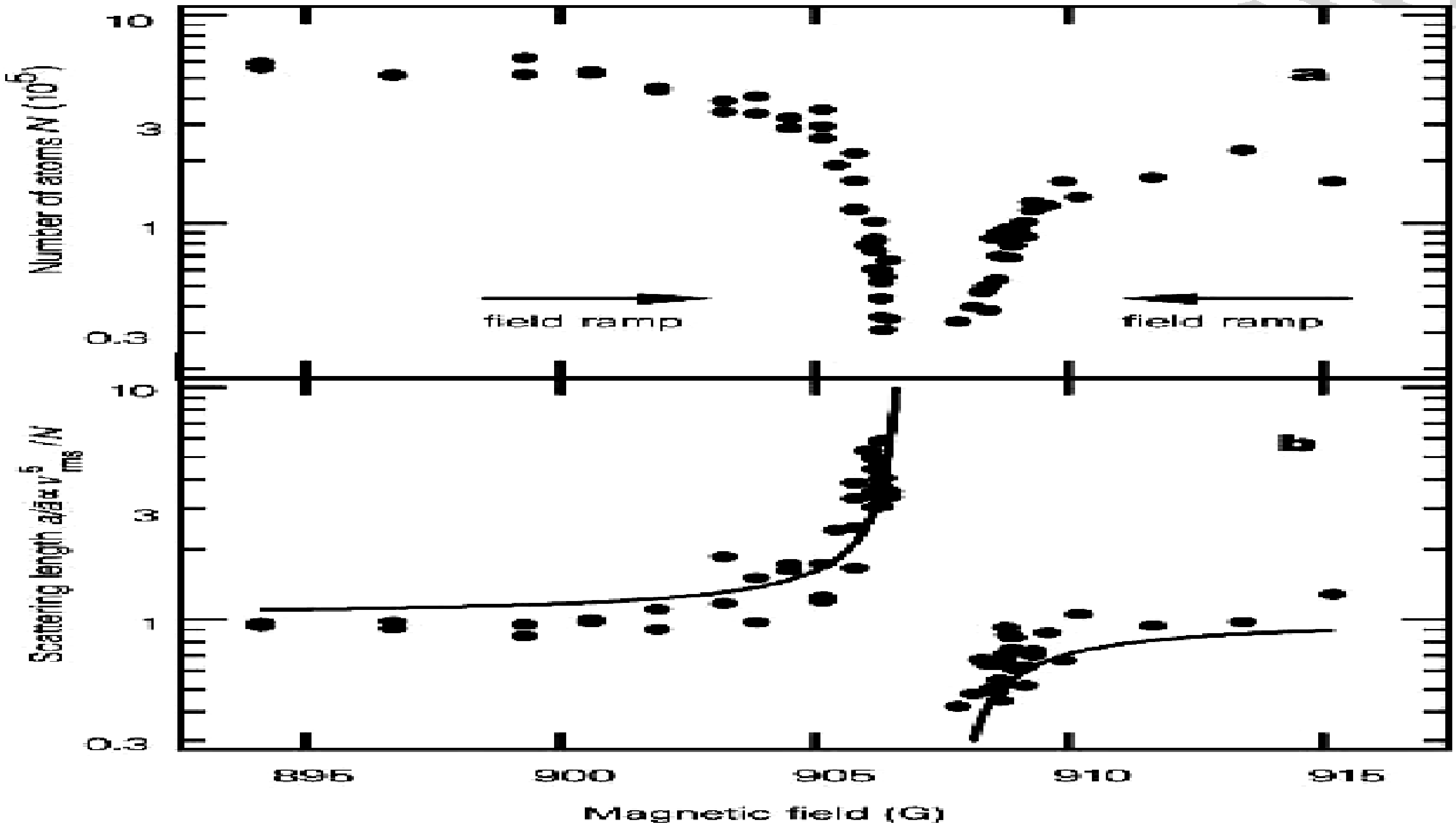

Figure 2 Observation of the Feshbach resonance at 907 G using time-of-flight absorption imaging. **a**, Number of atoms in the condensate versus magnetic field. Field values above the resonance were reached by quickly crossing the resonance from below and then slowly approaching from above. **b**, The normalized scattering length $a/\tilde{a} \propto v_{\mathrm{rms}}^5/N$ calculated from the released energy, together with the predicted shape (equation (1), solid line). The values of the magnetic field in the upper scan relative to the lower one have an uncertainty of <0.5 G.

Z. X. Liang, Z. D. Zhang, W. M. Liu,

Dynamics of a bright soliton
in Bose-Einstein condensates
with time-dependent atomic scattering length
in an expulsive parabolic potential,

Phys. Rev. Lett. 74, 050402 (2005).

（**SCI** 引用 **47** 次）

$$
\begin{aligned}
i\frac{\partial\psi\left(x,t\right)}{\partial t}+\frac{\partial^{2}\psi\left(x,t\right)}{\partial x^{2}} &+ 2a(t)|\psi\left(x,t\right)|^{2}\psi\left(x,t\right)\\
&+ \frac{1}{4}\lambda^{2}x^{2}\psi\left(x,t\right)=0.
\end{aligned}
\tag{1}
$$

$$
\begin{aligned}
\psi &= \left[A_c+A_s\frac{(\gamma\cosh\theta+\cos\varphi)+i(\alpha\sinh\theta+\beta\sin\varphi)}{\cosh\theta+\gamma\cos\varphi}\right]\\
&\quad\times\exp\left(\frac{\lambda t}{2}+i\varphi_c\right),
\end{aligned}
\tag{4}
$$

where

$$
\begin{aligned}
\theta &= -\frac{\left[\left(k_0+k_s\right)\Delta_R-\sqrt{g_0}A_s\Delta_I\right]\left[\exp\left(2\lambda t\right)-1\right]}{2\lambda}\\
&\quad+\Delta_R x\exp\left(\lambda t\right),\\
\varphi &= -\frac{\left[\left(k_0+k_s\right)\Delta_I+\sqrt{g_0}A_s\Delta_R\right]\left[\exp\left(2\lambda t\right)-1\right]}{2\lambda}\\
&\quad+\Delta_I x\exp\left(\lambda t\right),
\end{aligned}
\tag{5}
$$

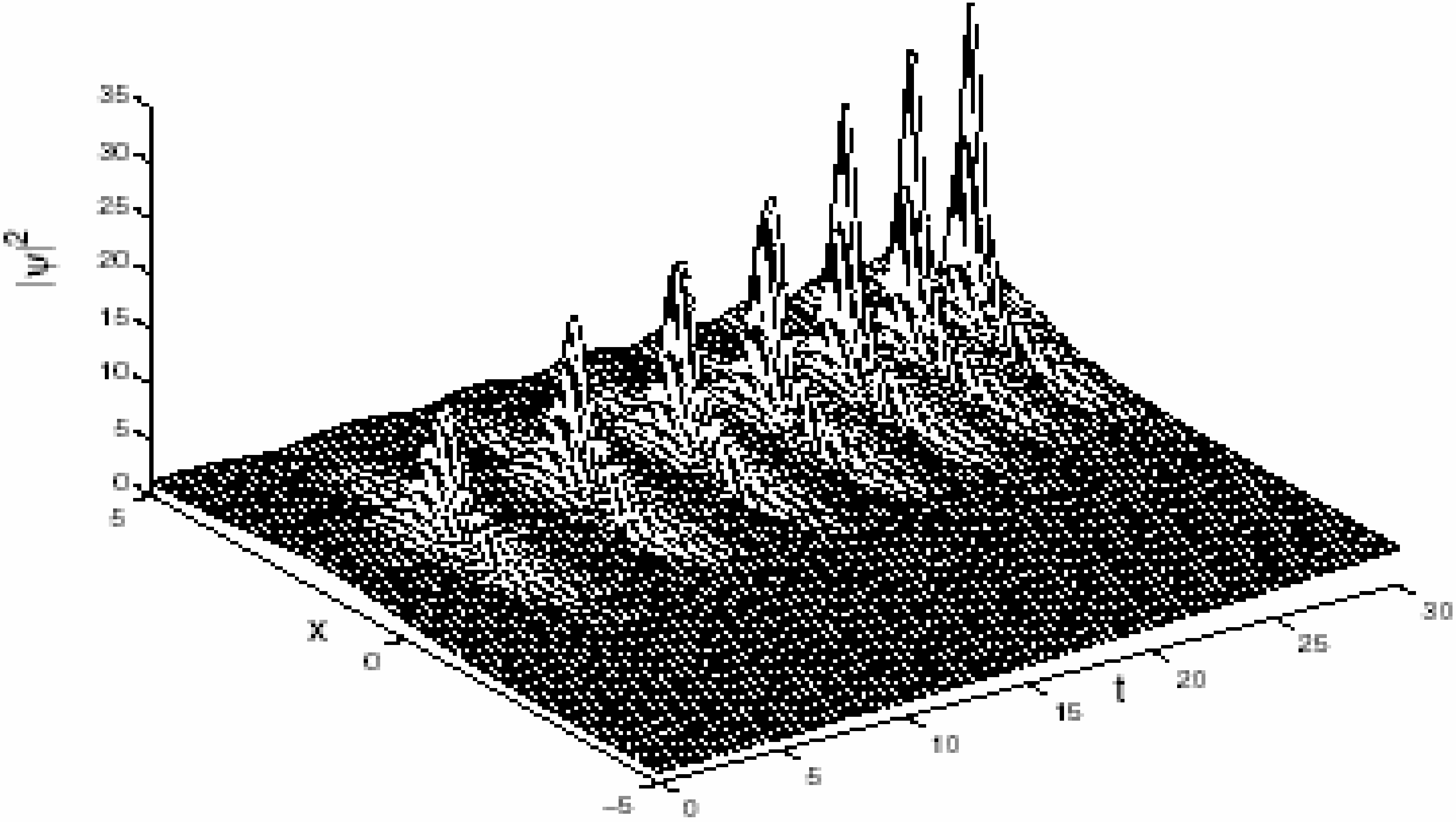

Figure 1: The dynamics of Feshbach resonance managed soliton in the expulsive parabolic potential given by Eq. (8). The parameters are given as follows:$\lambda = 2 \times 10^{-2}$, $g_0 = 0.25$, $A_c = 1$, $A_s = 2.4$, $k_0 = 0.03$,

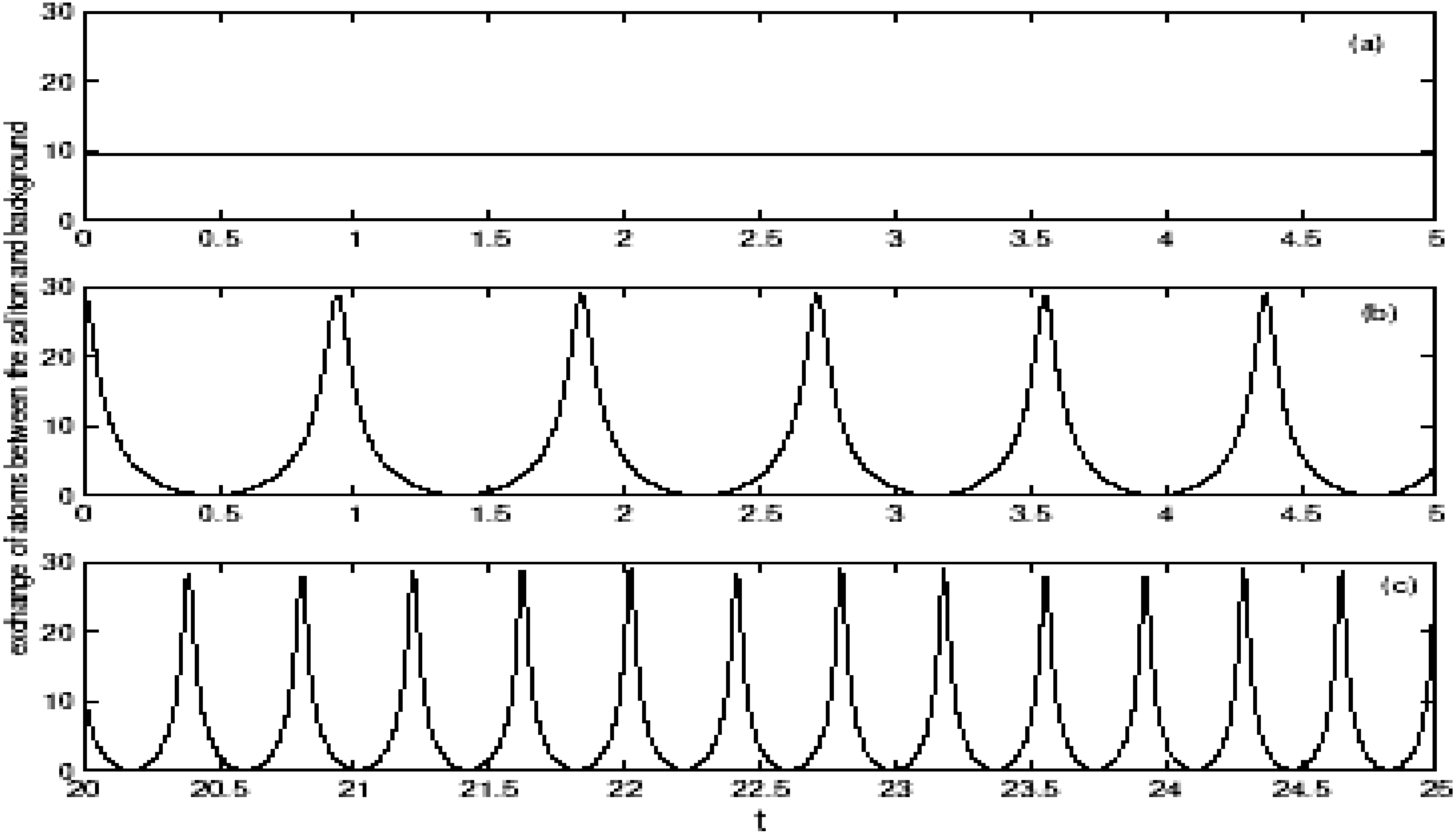

Figure 2: Time-periodic atomic exchange between the bright soliton and the background given by Eq. (13). The range of time is: (a) and (b) t=[0, 5], (c) t=[20, 25]. The parameters are given as follows: $\lambda = 0.02$, $g_0 = 1$, $A_s = 4.8$, (a) $A_c = 0$, (b) and (c) $A_c = 2.3$.

4.2. Strong correlated bosonic system

$$\hat{H} = -J\sum_{\langle i,j\rangle} \hat{a}_i^{\dagger}\hat{a}_j + \sum_i \varepsilon_i \hat{n}_i + \frac{1}{2}U\sum_i \hat{n}_i(\hat{n}_i - 1), \qquad (3)$$

4.3. Quantum Hall Effect

1985, Quantum Hall Effect, Nobel Prize in Physics

1998, Fraction Quantum Hall Effect, Nobel Prize in Physics

2003, Spin Hall Effect

5. Spinor BEC

J. Stenger, Nature 396, 345 (1998).

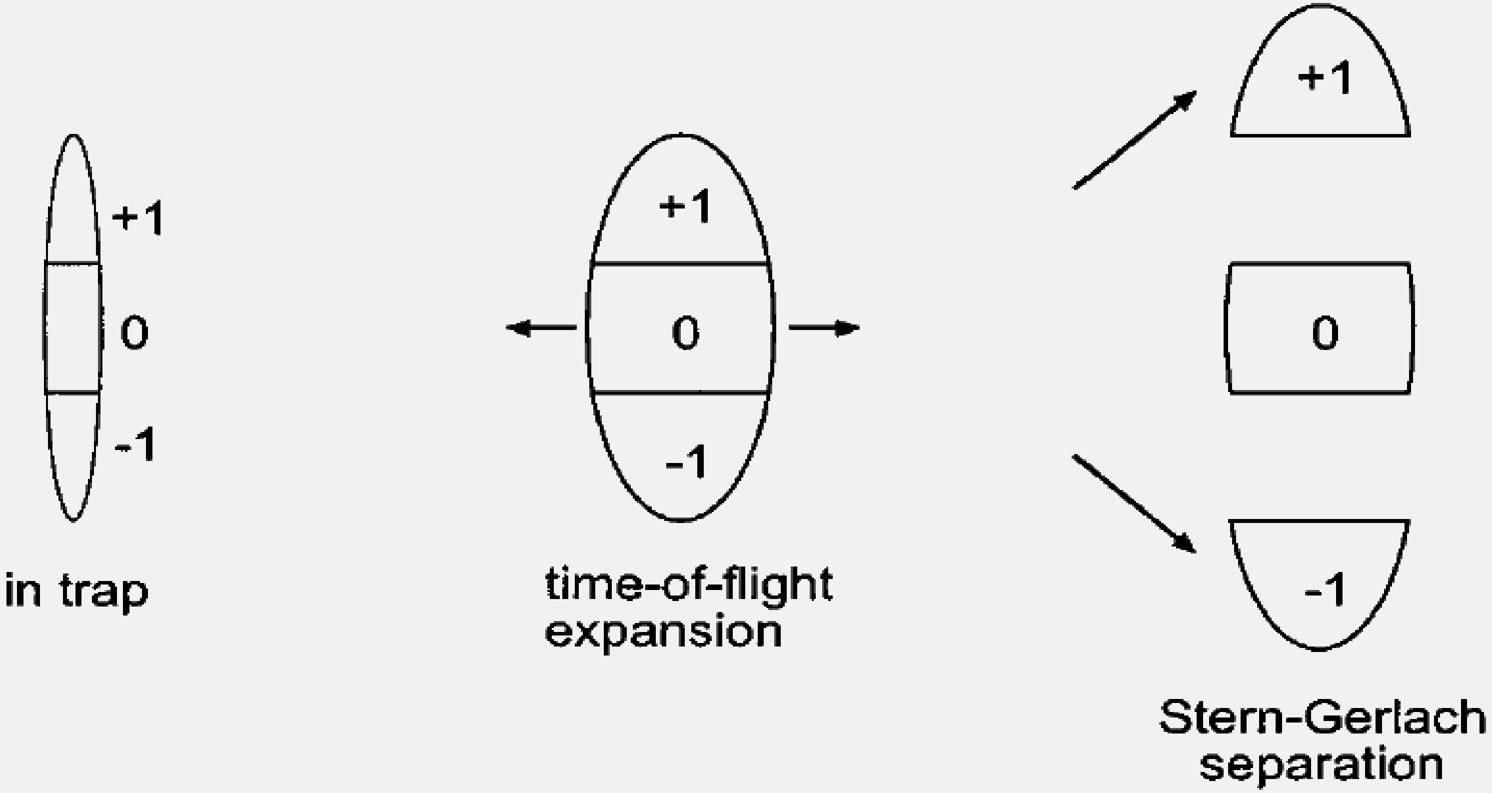

Fig. 21. Probing spinor condensates. After release from the elongated optical trap, the trapped spinor condensate expands primarily radially while maintaining the axial hyperfine distribution. A magnetic field gradient is then used to separate out the different components while preserving their shape. A subsequent absorption probe reveals the spatial and hyperfine distributions in the trap. From Ref. 53.

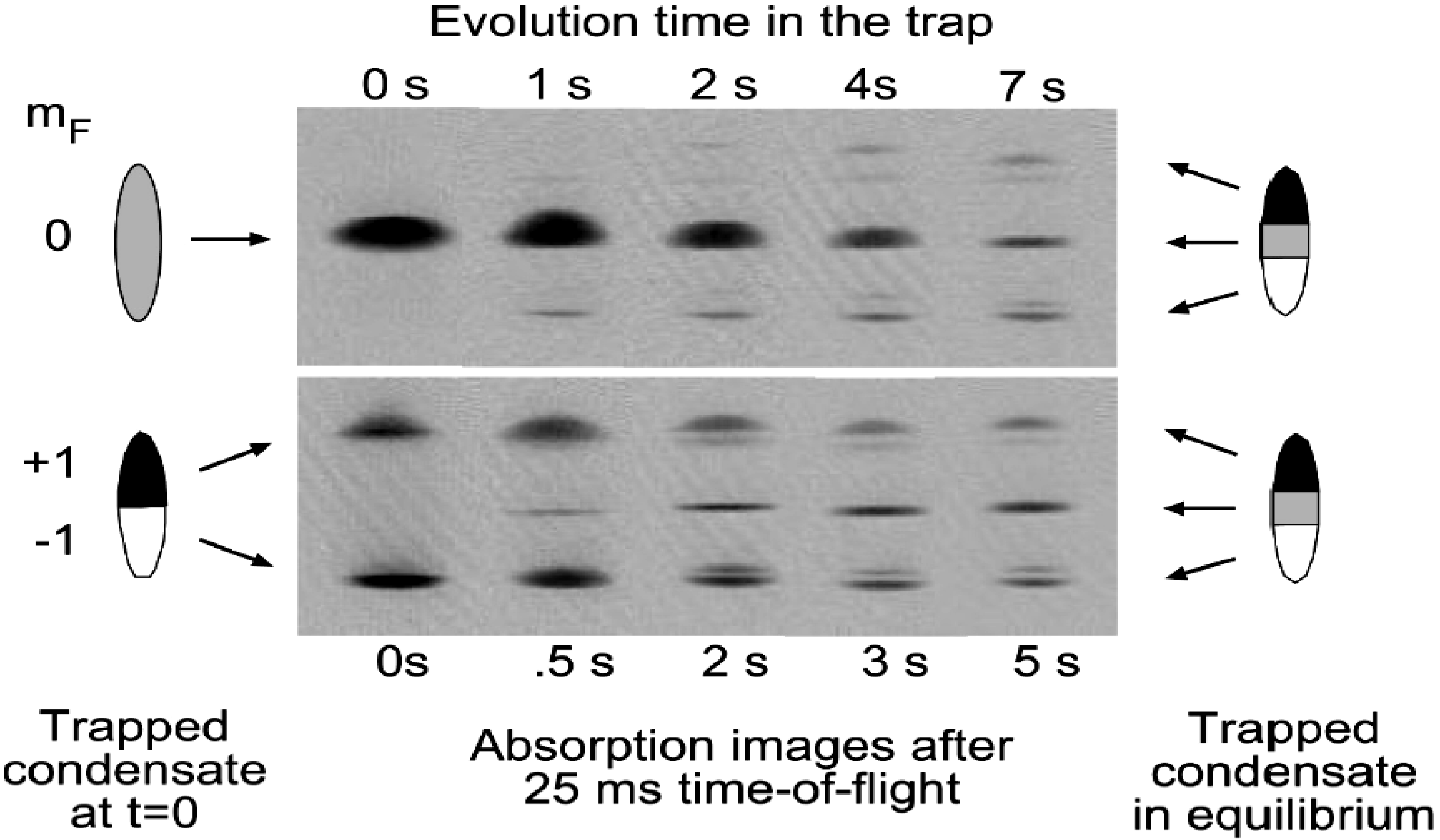

Fig. 22. Formation of the ground-state spin domains. Absorption images of ballistically expanding spinor condensates show both the spatial and hyperfine distributions. The images of clouds with various dwell times in the trap show the evolution to the same equilibrium for condensates prepared in either a pure $|m_F = 0\rangle$ state (upper row) or in equally populated $|m_F = \pm1\rangle$ states (lower row). From Ref. 53.

Z.W. Xie, W.P. Zhang, S.T. Chui, W.M. Liu,

Magnetic solitons of spinor Bose-Einstein condensates in optical lattice,

Phys. Rev. A69, 053609 (2004).

Z.D. Li, P.B. He, L.Li, J.Q. Liang, W.M. Liu,

Soliton collision of spinor Bose-Einstein condensates in optical lattice,

Phys. Rev. A71, 053608 (2005).

L. Li, Z.D. Li, B. A. Malomed, D. Mihalache, W. M. Liu,

Exact soliton solutions and nonlinear modulation instability in spinor Bose-Einstein condensates,

Phys. Rev. A 72, 033611 (2005).

6. Boson-Fermion mixture

6.1. Collapse of attractive BEC

6.2. Collapse of Fermi gas

6.3. Boson-Fermion mixture

6.1. Collapse of attractive BEC

C.E. Wieman, Nature 412, 295 (2001).

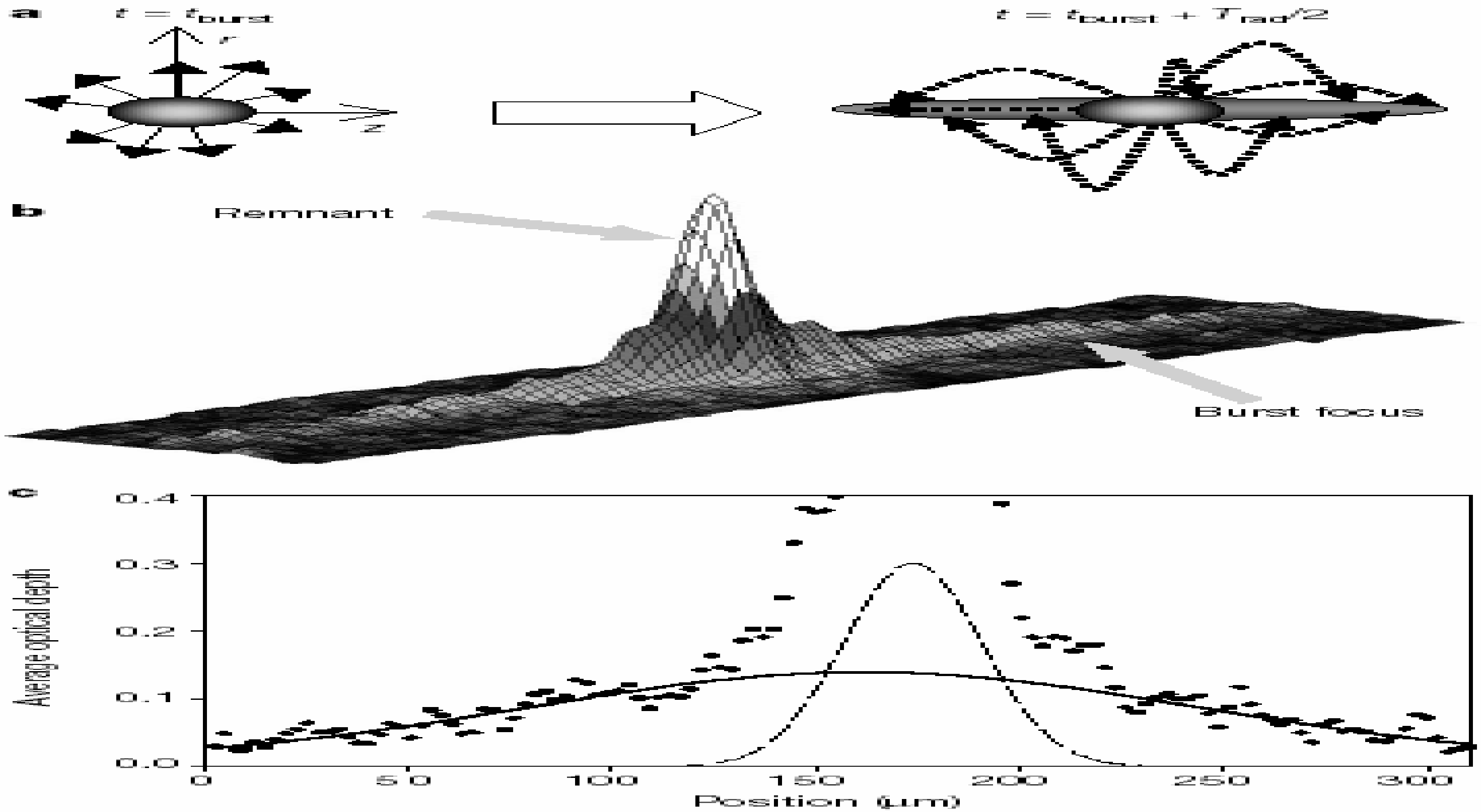

Figure 3 A burst focus. **a**, Conceptual illustration of a radial burst focus. t_{burst} is the time at which the burst is generated and T_{rad} is the radial trap period. **b**, An image of a radial burst focus taken 33.5 ms after a jump from $a_{init} = 0$ to $-30a_0$ for $N_0 = 10{,}000$. $T_{rad}/2 = 28.6$ ms, which indicates that the burst occurred 4.9(5) ms after the jump. The axial energy distribution for this burst corresponded to an effective temperature of 62 nK. The image is 60 × 310 μm. **c**, Radially averaged cross-section of **b** with a gaussian fit to the burst energy distribution. The central 100 μm were excluded from the fit to avoid distortion in the fit due to the condensate remnant ($\sigma = 9$ μm) and the thermal cloud ($\sigma = 17$ μm). The latter is present in the pre-collapse sample due to the finite temperature, and appears to be unaffected by the collapse. The dashed line indicates the fit to this initial thermal component. We note the offset between the centres of the burst and the remnant. This offset varies from shot to shot by an amount comparable to the offset shown.

6.2. Collapse of Fermi gas

M. Inguscio, Science 297, 2240 (2001).

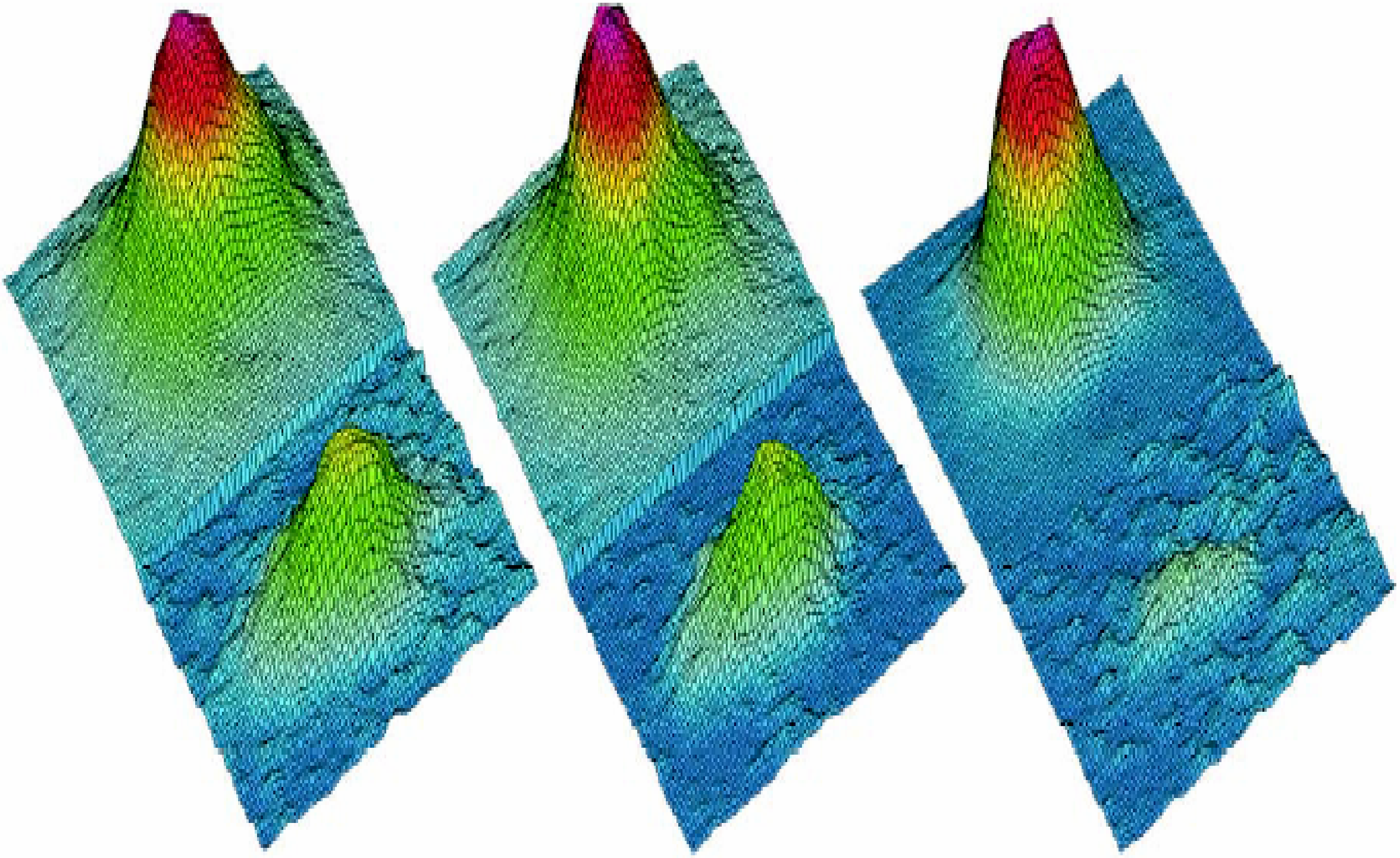

Fig. 2. False-color reconstruction of the density distributions of the Fermi (front) and Bose (back) gases during the evaporation procedure, as detected after a ballistic expansion of 4 ms for K and 19 ms for Rb. (**Left**) The BEC starts to form out of the thermal cloud and is coexisting with a relatively large Fermi gas; (**middle**) as the BEC grows larger, the Fermi gas is only moderately depleted by inelastic collisions; (**right**) when a quasi-pure condensate of 10^5 atoms has formed, the Fermi gas has already collapsed. The fermionic distributions have been vertically expanded by a factor of 3.

6.3. Boson - Fermion mixture

R.G. Hulet, Science 291, 2570 (2001).

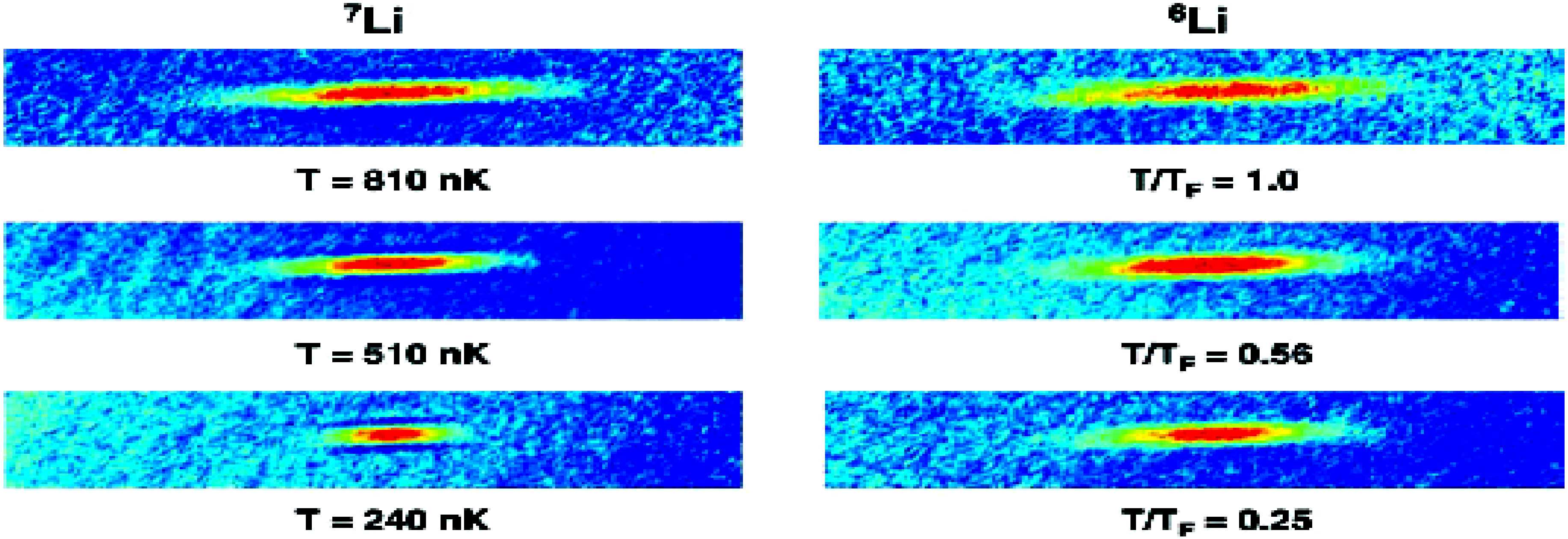

Fig. 1. Two-dimensional false-color images of both ^{7}Li and ^{6}Li clouds. At $T/T_F = 1.0$, the two clouds are approximately the same size, but as the atoms are cooled further, to $T/T_F = 0.56$, the Bose gas contracts, whereas the Fermi gas exhibits only subtle changes in size. At $T/T_F = 0.25$, the size difference between the two gases is clearly discernable. At this temperature the ^{7}Li image displays distortions due to high optical density. However, these distortions are present only in the radial direction and do not affect the measurements. The fitted numbers of ^{7}Li and ^{6}Li atoms, N_7 and N_6, and the fitted temperatures are as follows: For the upper set, $N_7 = 2.4 \times 10^5$, $N_6 = 8.7 \times 10^4$, and $T = 810$ nK; for the middle set, $N_7 = 1.7 \times 10^5$, $N_6 = 1.3 \times 10^5$, and $T = 510$ nK; and for the lower set, $N_7 = 2.2 \times 10^4$, $N_6 = 1.4 \times 10^5$, and $T = 240$ nK. The probe detuning is a parameter of the fits but is constrained to vary by no more than its uncertainty of ± 3 MHz. The fits result in typical reduced-χ^2 values of ~ 1.0. The uncertainties in number and temperature are due mainly to the uncertainties in the fit and are roughly estimated by finding the point at which the reduced-χ^2 increases by 20%. The resulting uncertainties are 8% in temperature and 15% in number. Other sources of uncertainty are relatively insignificant. The size of each displayed image is 1.00 mm in the horizontal axis and 0.17 mm in the vertical axis.

7. BEC – BCS crossover

BEC: $a>0$, bound molecular state

BCS: $a<0$, fermionic atom pairs -

strong interaction

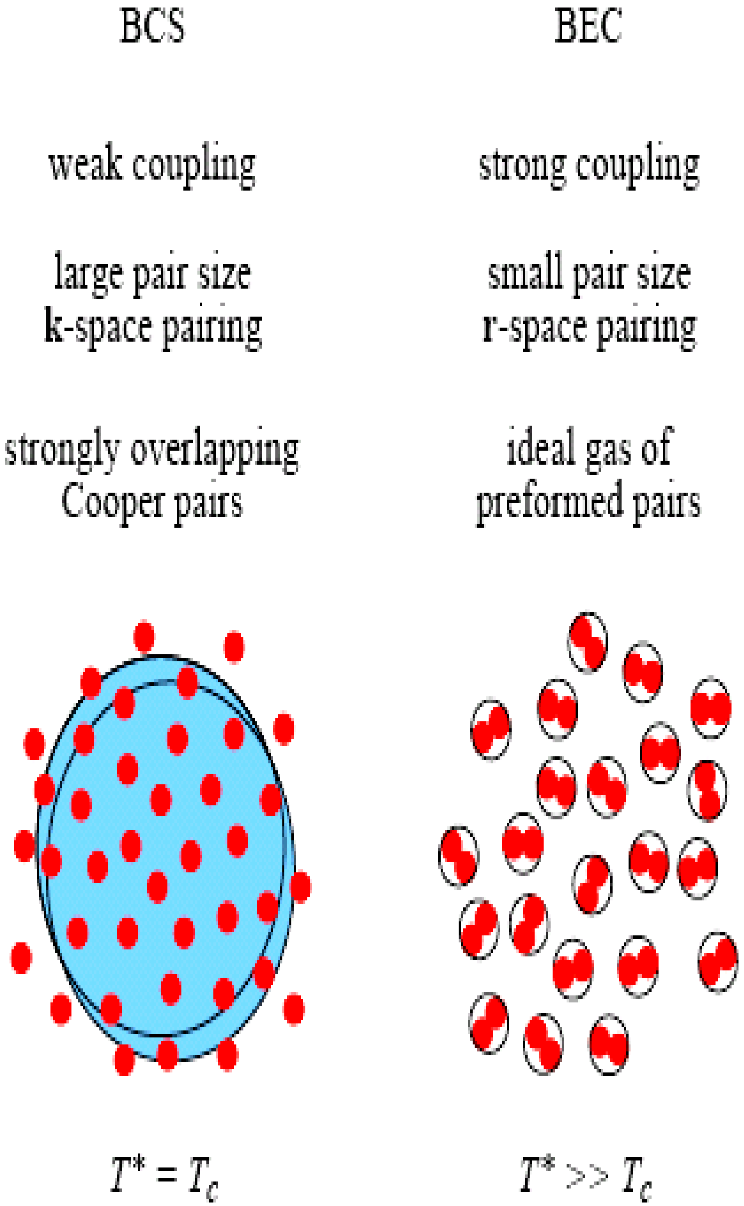

Fig. 1. Contrast between BCS- and BEC-based superfluids. Here T^* represents the temperature at which pairs form, while T_c is that at which they condense.

BCS

$$\frac{\text{Binding energy of pairs}}{\text{Fermi energy}} \approx \frac{\text{Transition termperature}}{\text{Fermi temperatue}} \approx$$

10^{-5} … 10^{-4}	normal superconductors
10^{-3}	superfluid ^{3}He
10^{-2}	high T_c superconductors

BEC

$$\frac{\text{Binding energy of bosons}}{k_B \text{ BEC transition temperature}} \approx$$

10^{5}	superfluid ^{4}He
10^{10}	alkali BEC

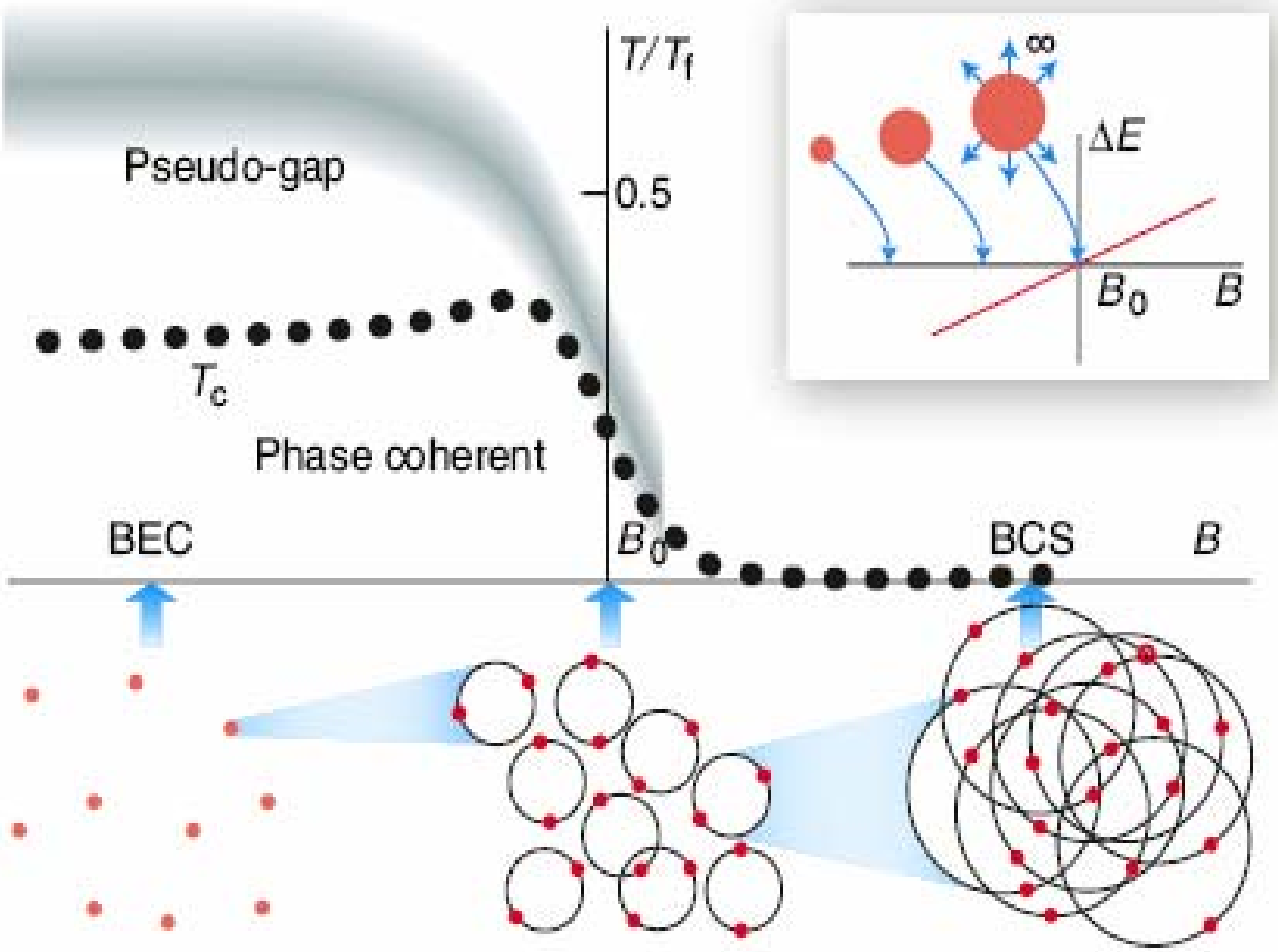
Pseudo-gap
T/T_f
0.5
T_c
Phase coherent
BEC
B_0
BCS
B
∞
ΔE
B_0
B

8. Spin polarized fermi gas

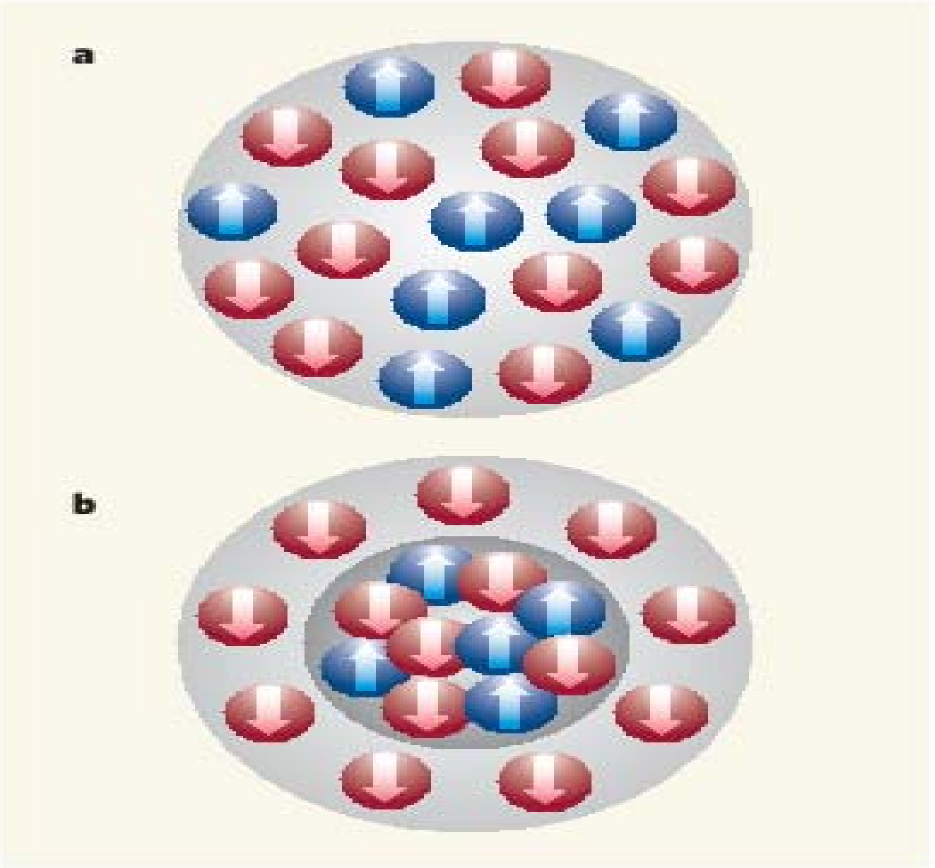

Figure 1 | Changing shape. **a**, A homogeneous state of an unequal number of spin-up and spin-down atoms, such as that prepared by Zwierlein *et al.*[1]. **b**, As the gas temperature is lowered past a critical value, a phase transition occurs. A superfluid state forms in the centre of the gas with spin-up and spin-down atoms paired and equal in number, and the excess unpaired atoms move to outside the central core.

配对机制有：**Sarma** 态或称为能隙内配对态 **(interior gap pairing)**，相分离态，费米面变形后的配对态和库柏对带有有限动量的**Fulde-Ferrell-Larkin-Ovchinnikov (FFLO)**态。

一维极化费米子的基态总共有三个相：**BCS** 超流相 **(SF)**，极化超流相 **(SFp)** 和正常相 **(N)** 。

M.W. Zwierlein et al., Science 311, 492 (2006)

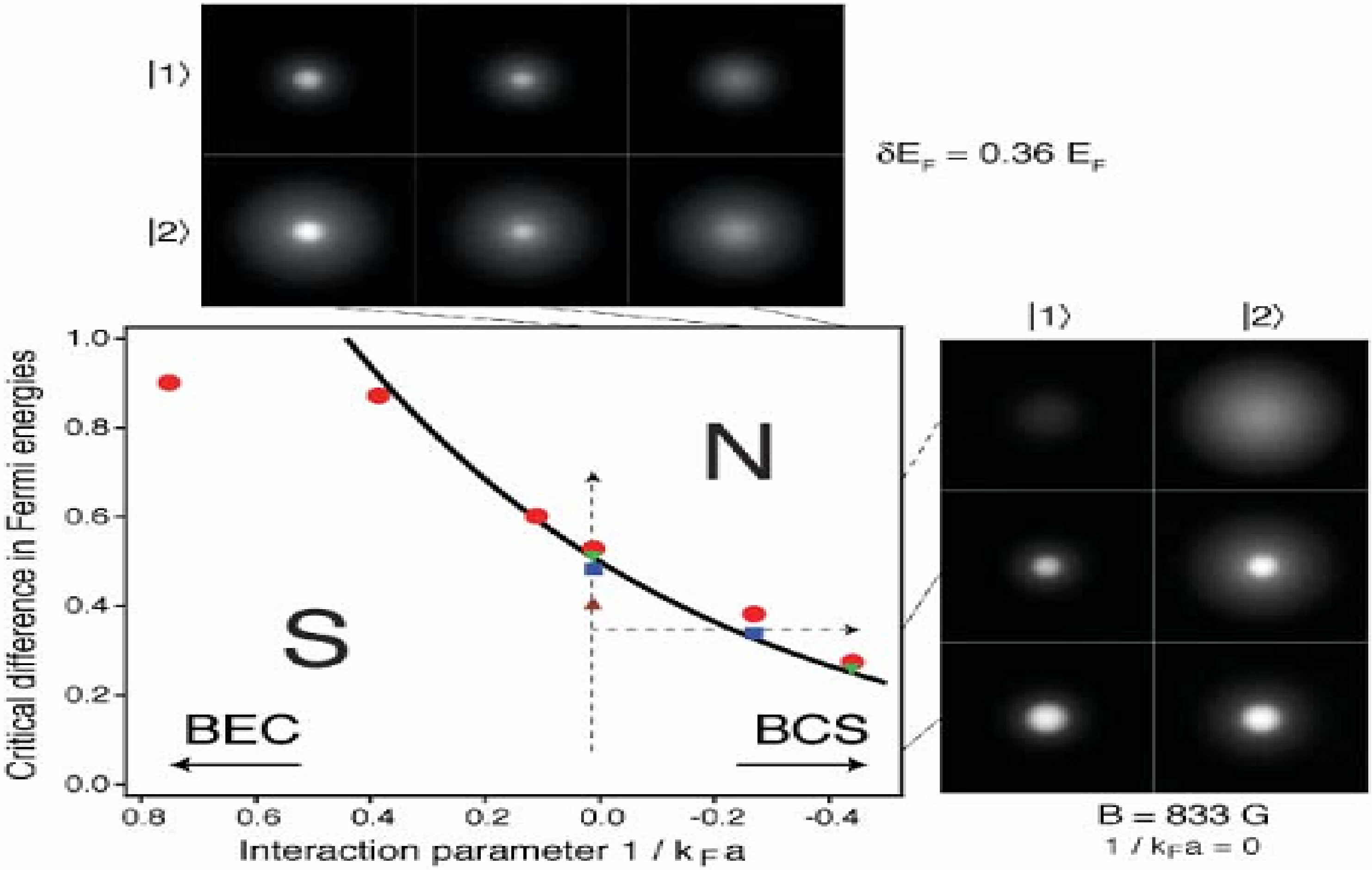

Fig. 5. Critical difference in Fermi energies δE_F between the two spin states for which the superfluid-to-normal transition is observed. δE_F for each interaction strength and temperature is obtained from the critical population imbalance determined in Fig. 3 using $\delta E_F/E_F = (1 + \delta_c)^{1/3} - (1 - \delta_c)^{1/3}$. The symbols are defined in Fig. 3. The line shows the expected variation of the pairing gap Δ, where the value on resonance has been taken from (*24*) and the exponential behavior in the BCS regime, $\Delta \sim e^{-\pi/2k_F|a|}$, was assumed. Although the trend of δE_F is expected to follow that of Δ, the close agreement is coincidental. Representative density profiles illustrate the quantum phase transition for fixed interaction and for fixed population imbalance along the dashed lines.

M.W. Zwierlein et al., Nature 442, 54 (2006)

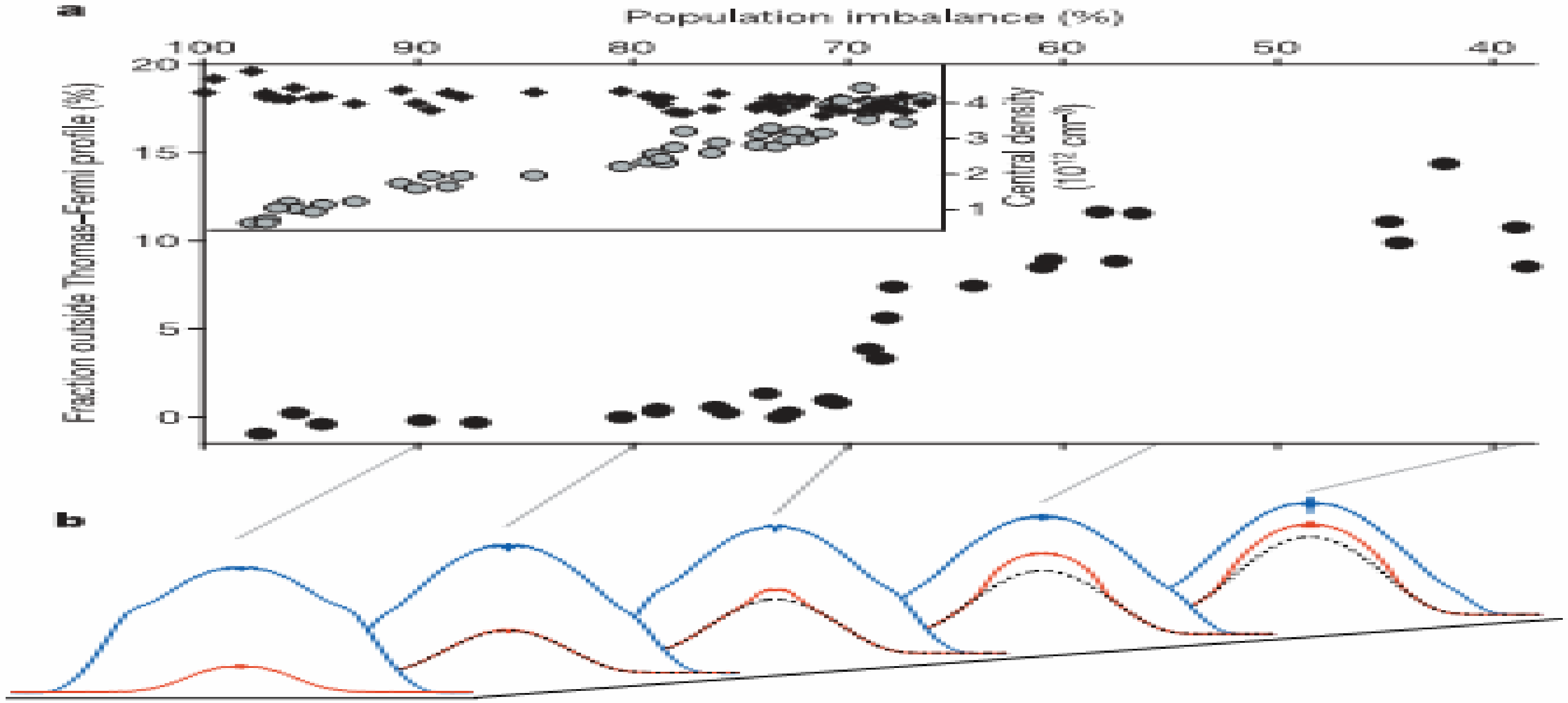

Figure 3 | Quantum phase transition to superfluidity for decreasing population imbalance. **a**, Main panel, the 'condensate fraction' of excess minority atoms, not contained in the Thomas–Fermi fit, versus population imbalance on resonance. **b**, Column density profiles of majority (blue) and minority (red) clouds, azimuthally averaged, for varying population imbalance. The condensate is clearly visible in the minority component as the dense central feature on top of the normal background (finite-temperature Thomas–Fermi fit, dotted lines). Below the critical imbalance $\delta_c = 70\%$, the condensate starts to form. The inset in **a** shows the central densities of the larger (black diamonds) and smaller (grey circles) cloud in the normal state above δ_c. This demonstrates that here the central densities are unequal, suppressing superfluidity. The densities were calculated from the central optical density and the fitted size of the clouds, assuming local density approximation and adjusting for ballistic (hydrodynamic) expansion of the outer radii of majority (minority) clouds. The data points for the condensate fraction show the average of several independent measurements.

G.B. Partridge et al., Science 311, 503 (2006)

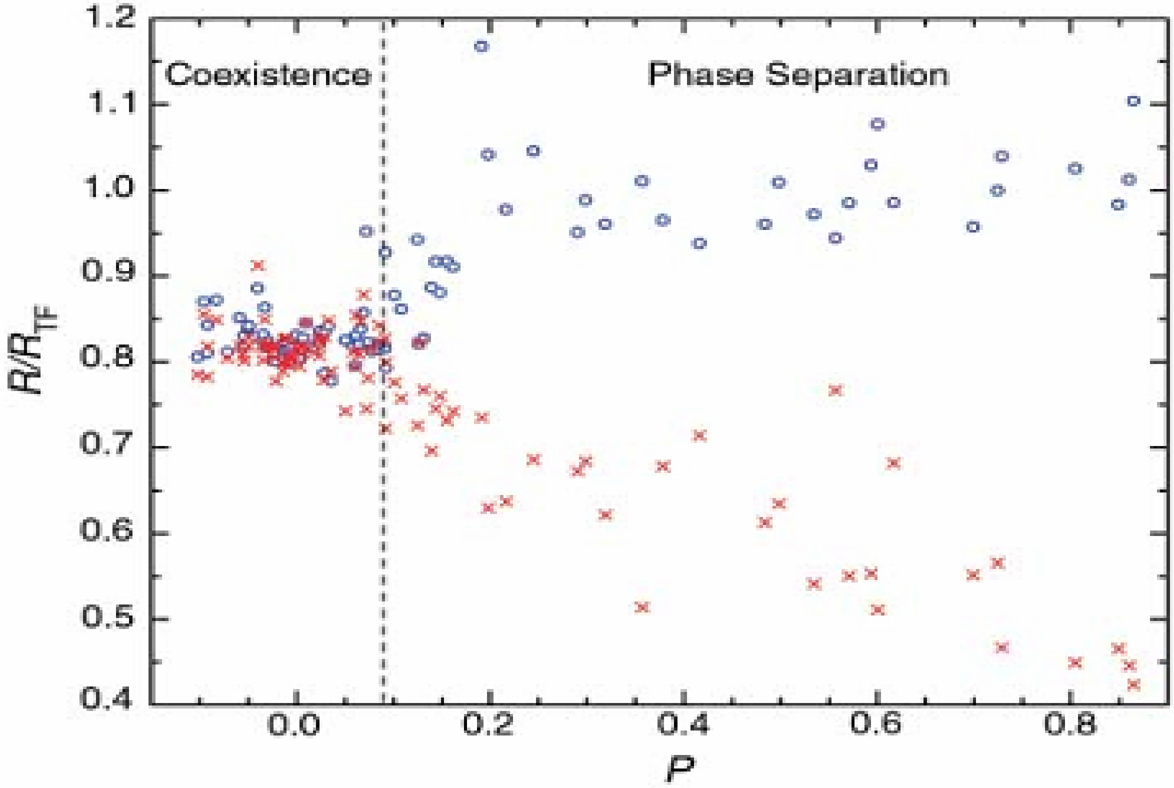

Fig. 3. R/R_{TF} versus P. The ratios of the measured axial radius to that of a noninteracting T-F distribution are shown as blue open circles for state $|1\rangle$ and as red crosses for state $|2\rangle$. The data combine 92 independent shots. The dashed line corresponds to the estimated critical polarization, $P_c = 0.09$, for the phase transition from coexisting to separated phases. The images are of sufficient quality that the assignment of phase separation is ambiguous in only two of the shots represented. Our contention for a phase transition at P_c has its basis in statistical evidence: None of the 31 shots deliberately prepared as $P = 0$ and only one with a measured $P < 0.07$ is phase separated, whereas all but two shots with $P > 0.11$ are. The width of this transition region is consistent with our statistical uncertainty in the measurement of P. Although fluctuations in absolute probe detuning lead to 15% uncertainty in total number, the difference in the two probe frequencies is precisely controlled, resulting in lower uncertainty in P. We estimate the uncertainty in a single measurement of P to be 5%, which is the standard deviation of measurements of P for distributions prepared as $P = 0$. Also from these distributions, we find no significant systematic shift in detection of relative number. The uncertainty in the ratio R/R_{TF} is estimated to be 2.5%, due mainly to the uncertainty in measuring υ_z (*20*). The uncertainty in R/R_{TF} for state $|2\rangle$ grows with increasing P because of greater uncertainty in the fitted value of R with decreasing N_2.

9. Magnon BEC

Science 298, 760 (2002).

9.1. Magnon BEC

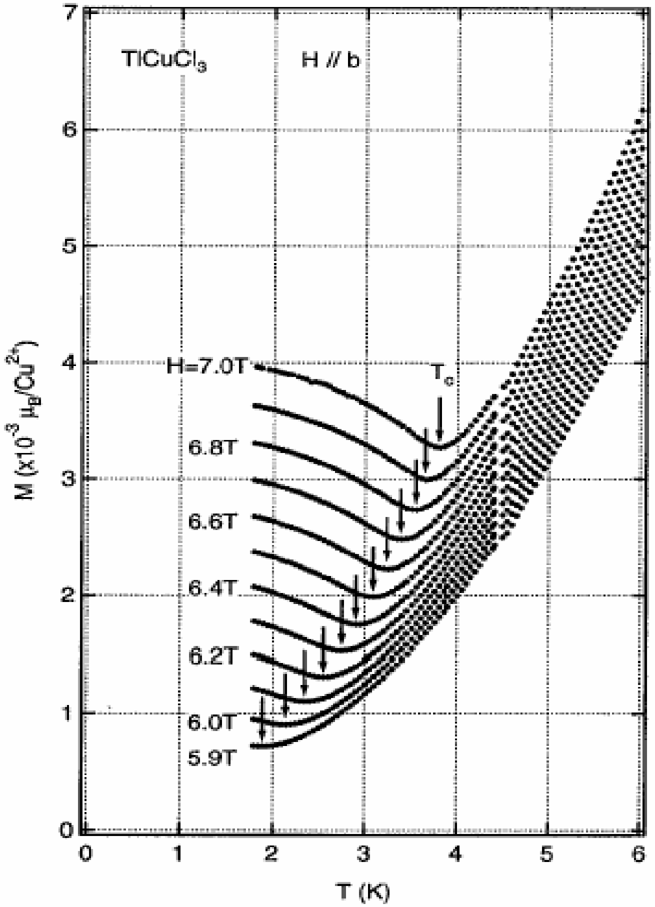

FIG. 2. The low-temperature magnetizations of TlCuCl$_3$ measured at various external fields for $H \parallel b$.

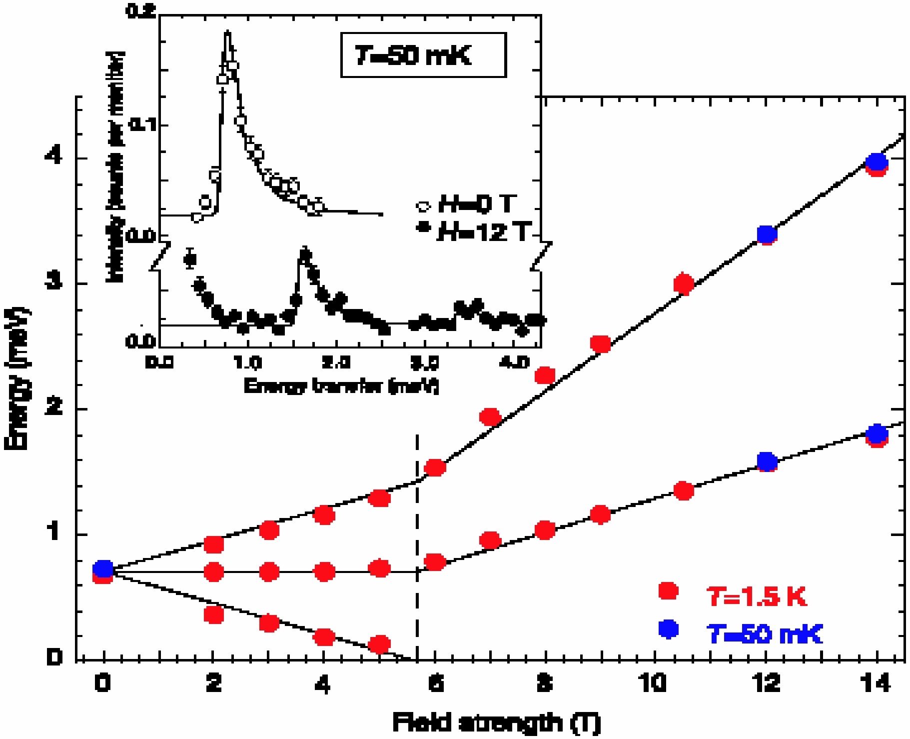

Figure 2 Dependence on the external magnetic field *H* of the magnetic excitation energy measured in TlCuCl$_3$ at the Bragg point $\tau = (0\ 4\ 0)$ r.l.u. Data are shown for fixed $T = 1.5$ K (red symbols) and $T = 50$ mK (blue symbols). Data are extracted from least-squares fits to the neutron scattering spectra (inset), curves reflect a Zeeman model. The quantum critical field $H = H_c$ is denoted by the dashed boundary. Comments and interpretations are given in the text.

9.2. Exciton BEC

Science 300, 1871 (2003).

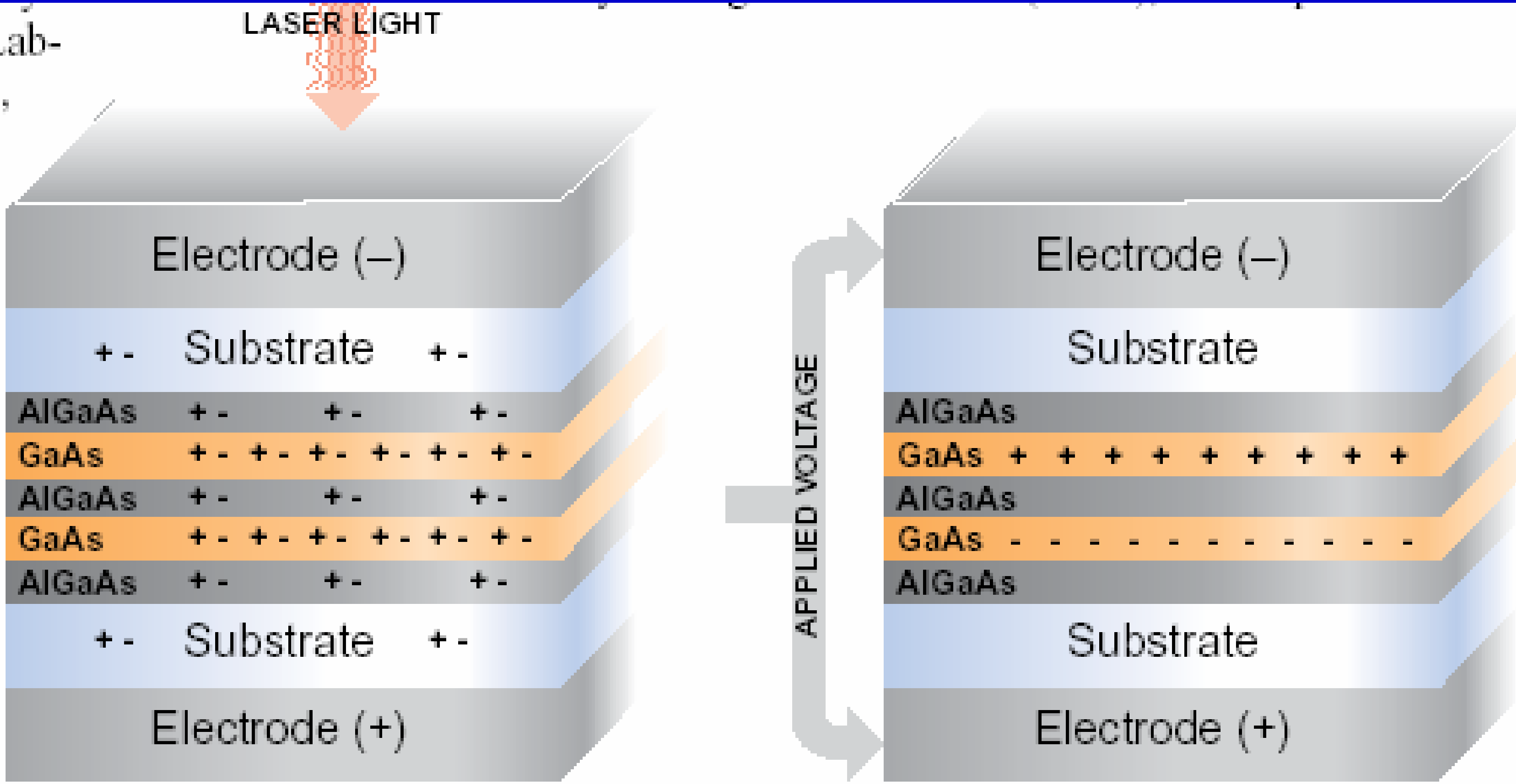

BEC in a semiconductor? Laser produces pairs of electrons (–) and holes (+) (left). Trapped in low-energy layers (right), charges form excitons that may condense into a BEC.

9.3. Superflow in Solid Helium

M. Chan, Science 305, 1941 (2004).

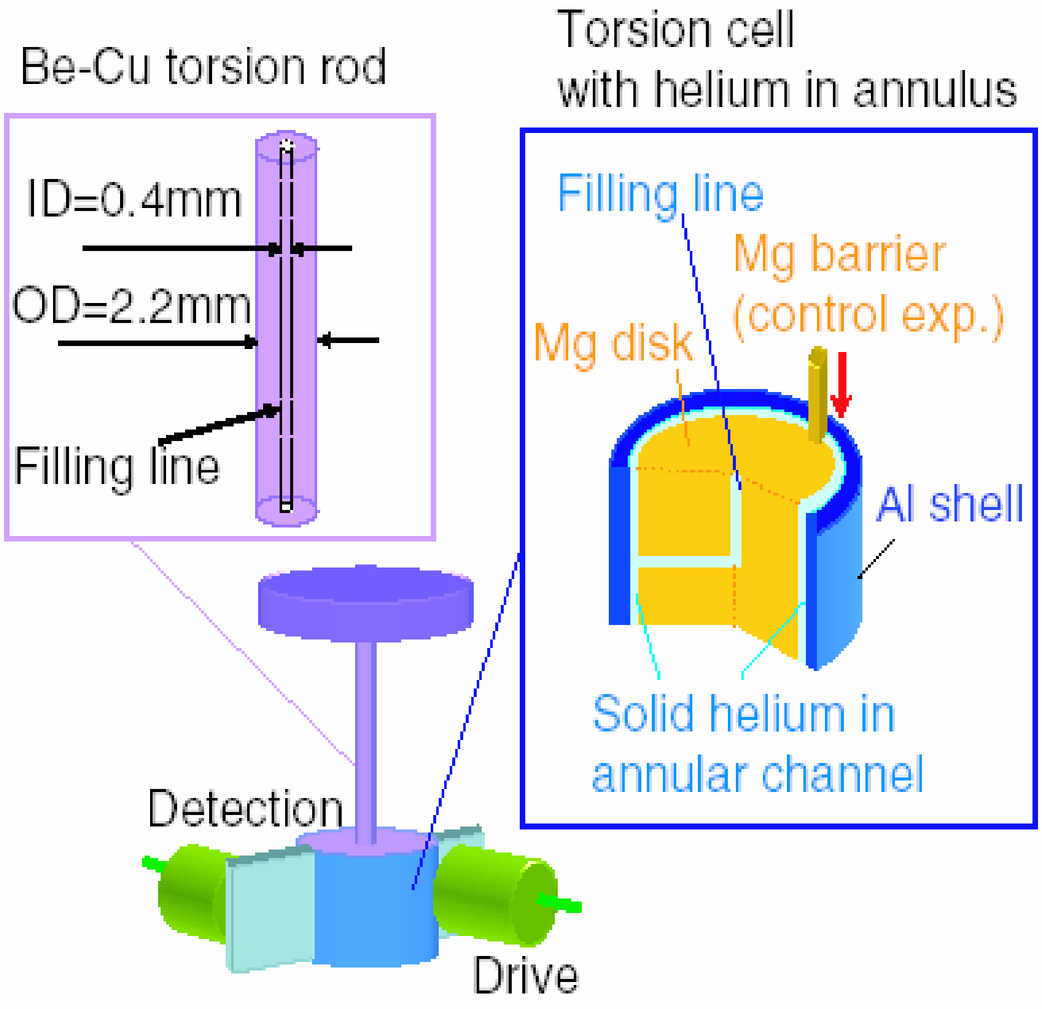

Fig. 1. Torsional oscillators: The cylindrical drive and detection electrodes are coupled capacitively to the two planar electrodes attached as fins on the two sides of the cylindrical torsion cell. Oscillation of the torsion cell induces an ac voltage on the detection electrode. This voltage enables a lock-in amplifier to keep the oscillation in resonance. The outside diameter, width, and height of the channel in the barrier-free torsion cell are 10 mm, 0.63 mm, and 5 mm, respectively. The mechanical quality factor of the oscillator is 2×10^6, allowing the determination of the resonant period to 0.2 ns out of a resonant period of 1 ms. The outside diameter, width, and height of the (blocked) channel of a second torsion cell with the barrier are 15 mm, 1.1 mm, and 5 mm, respectively. The mechanical quality factor and period precision values are similar to those of the barrier-free torsion cell.

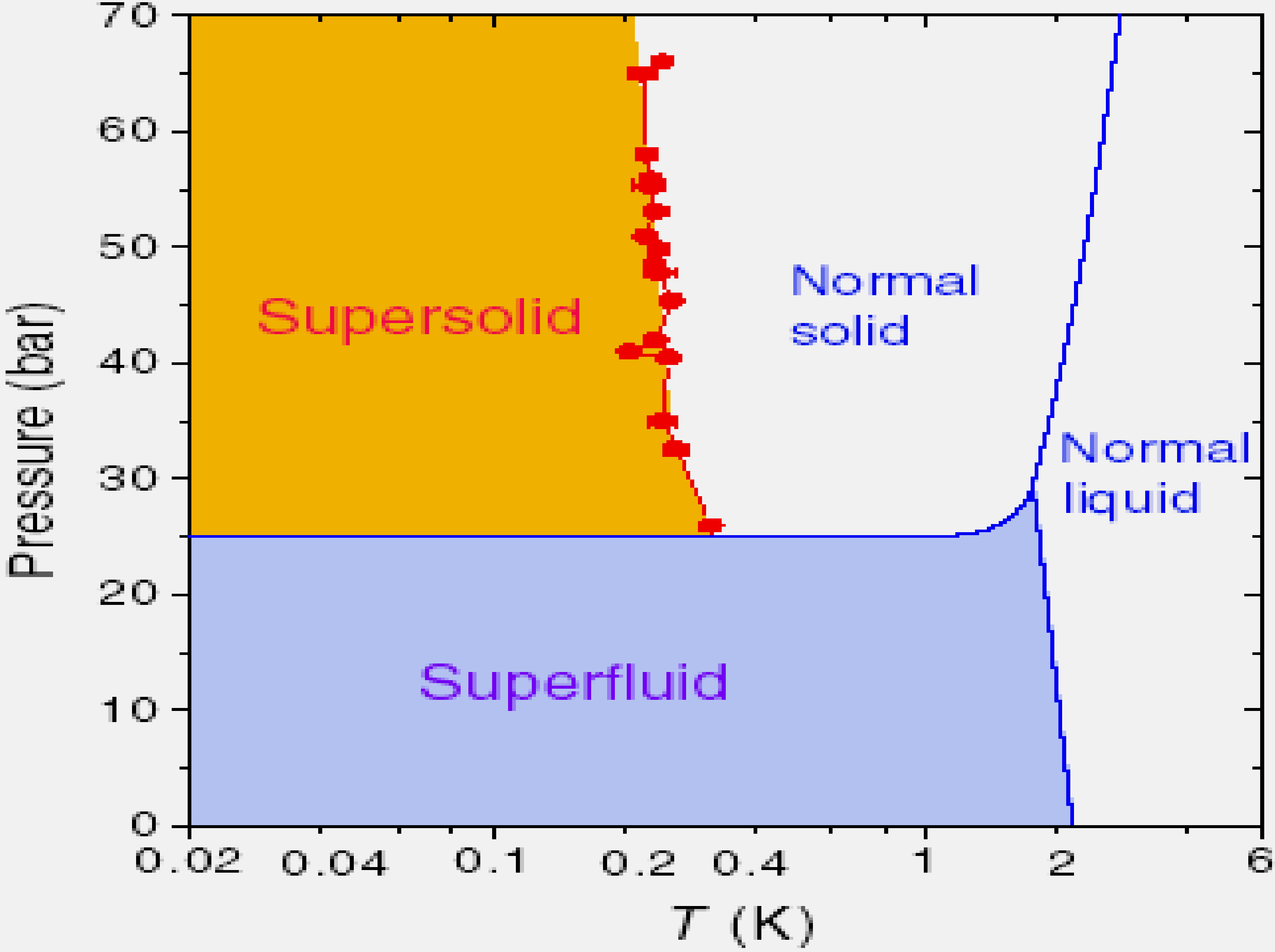

Fig. 4. Phase diagram of liquid and solid helium.

10. Application

- 10.1. Atomic laser
- 10.2. Atom clock
- 10.3. Interferometer (microgravity)
- 10.4. Waveguide
- 10.5. BEC on chip
- 10.6. Quantum tweezer
- 10.7. Information storage
- 10.8. Quantum computer
- 10.9. Four-wave mixing
- 10.10. Reducing light speed
- 10.11. Superradiance
- 10.12. Supernova

10.1. Atom laser

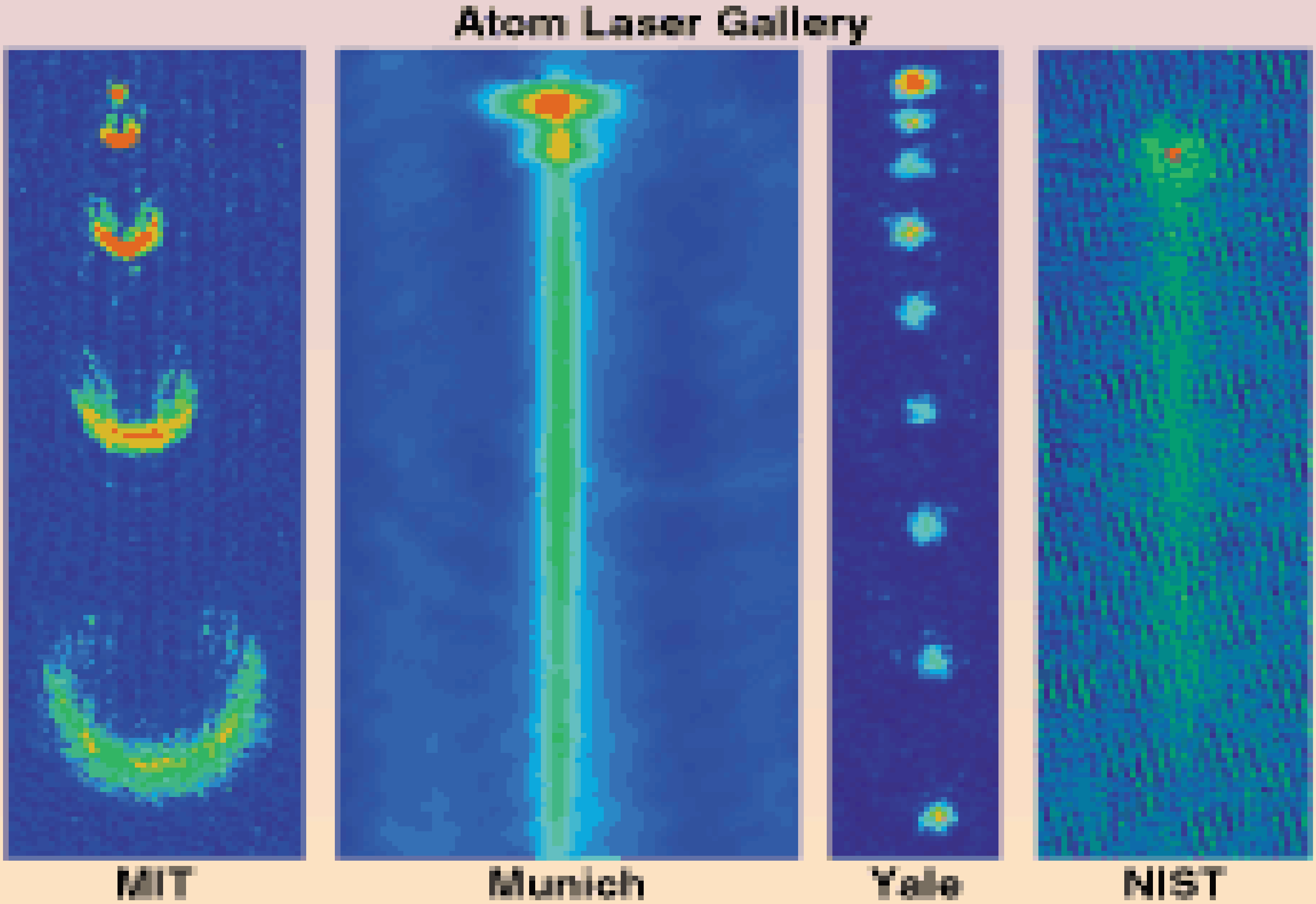

10.2. Atom clock

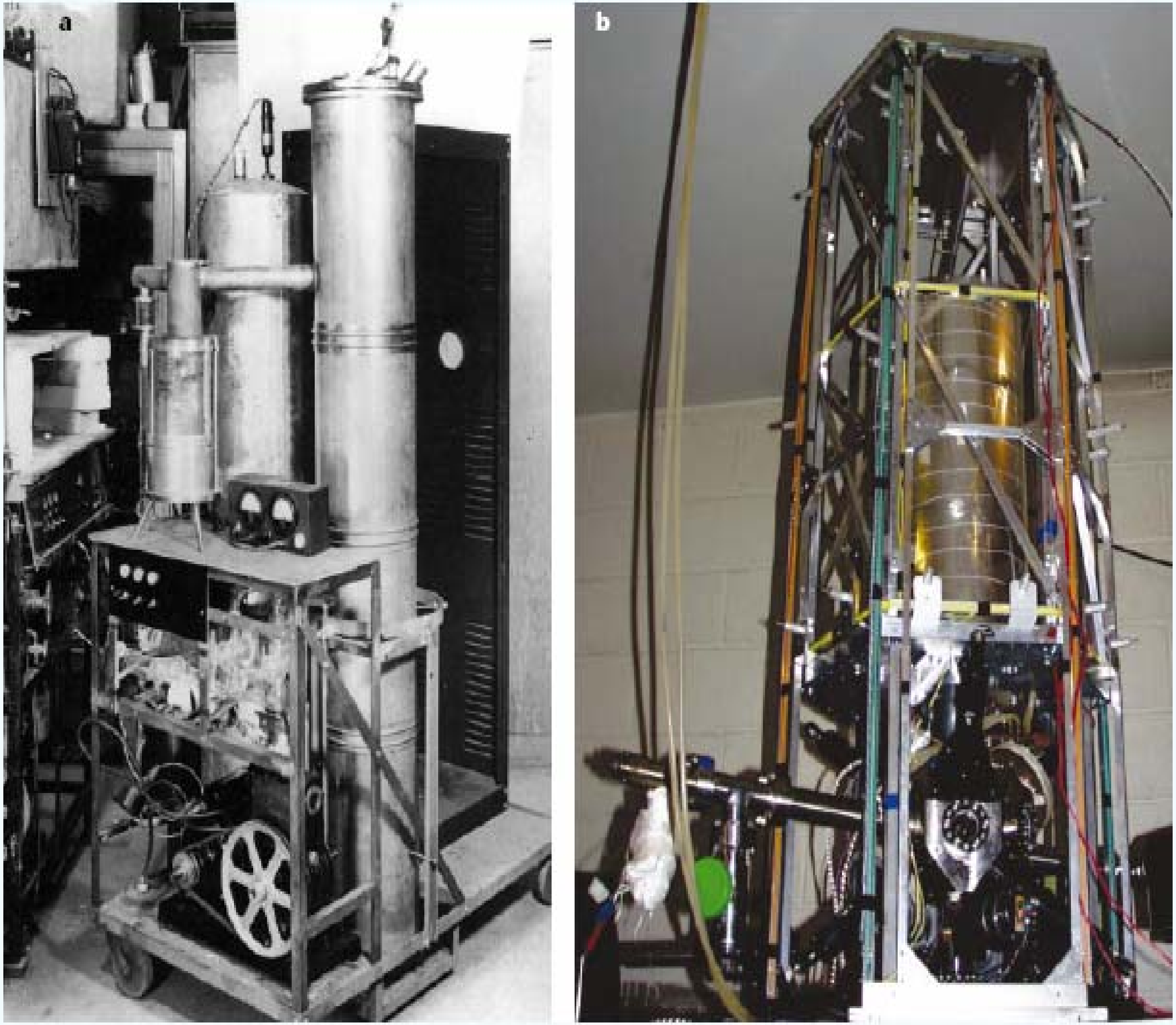

Figure 3 Atomic clocks. **a**, The first caesium atomic clock, built by Jerrold Zacharias in 1953. Zacharias also proposed a caesium clock using a fountain of atoms to test Einstein's prediction that a clock would slow down in raised in a gravitational potential. He failed to construct an atomic fountain, and although he never published his proposal, his attempt was passed down to two generations of physicists by word of mouth. (Photo: MIT Museum.) **b**, A rubidium atomic fountain clock built by the BNM-LPTF (Bureau National de Métrologie — Laboratoire Primaire du Temps et des Fréquences) and the Ecole Normale Supérieure, Paris. The atoms are trapped and cooled in the lower part of the apparatus before being launched upwards to a height of – 1 metre. The estimated accuracy of this clock is 1 part in 10^{15}, or 7 minutes over a period of time equal to the age of the Universe (–14 billion years). (Photo: C. Solomon, ENS.)

10.3. Atom interferometer (microgravity)

M. A. Kasevich, Science 298, 1363 (2002)

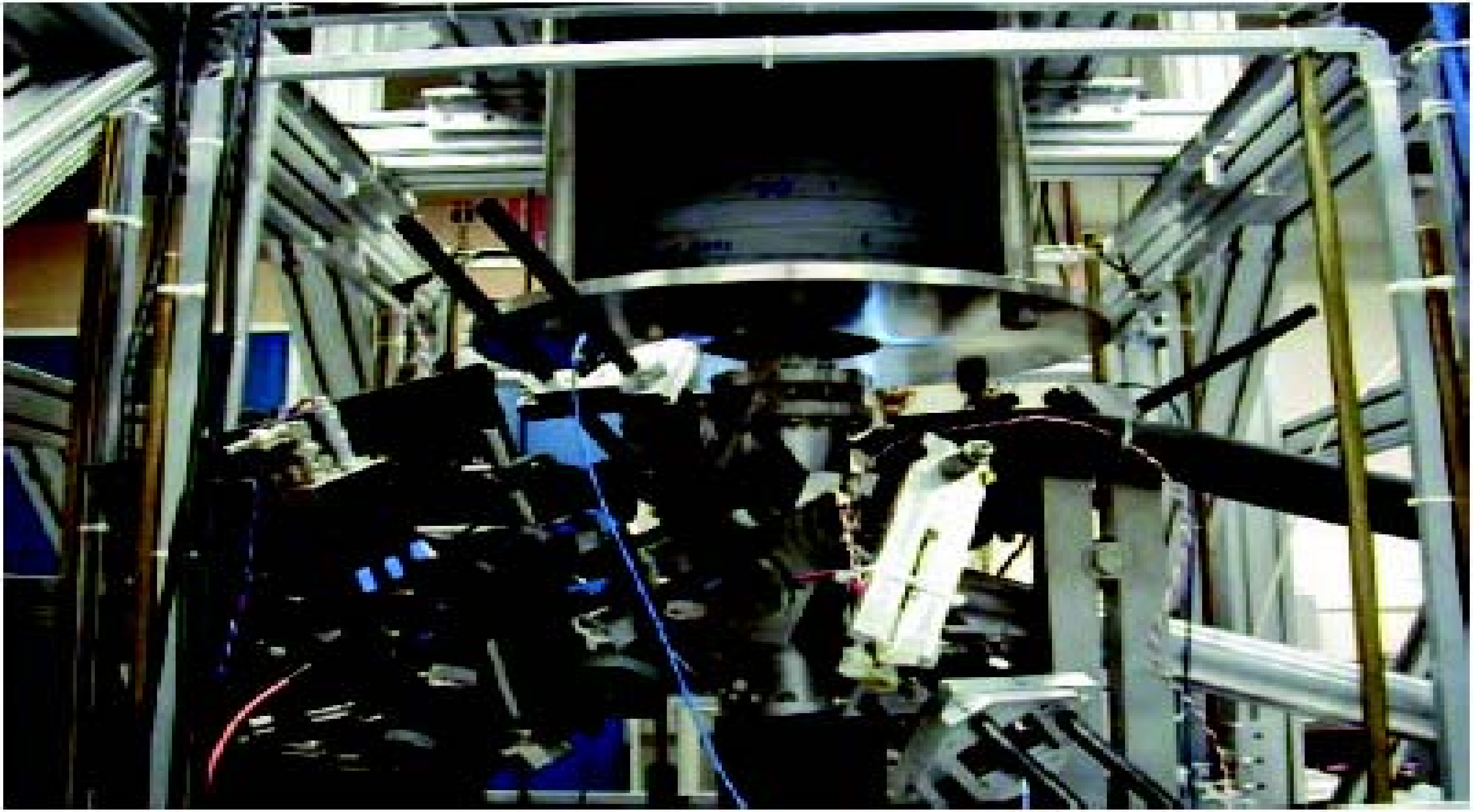

Fig. 4. Laboratory gravity gradiometer at Yale University, used to measure the gravitational influence of a well-characterized Pb test mass on a spatially separated pair of atom interferometer accelerometers.

10.3. Interferometer

J. Denschlag et al., Science 287, 97 (2000).

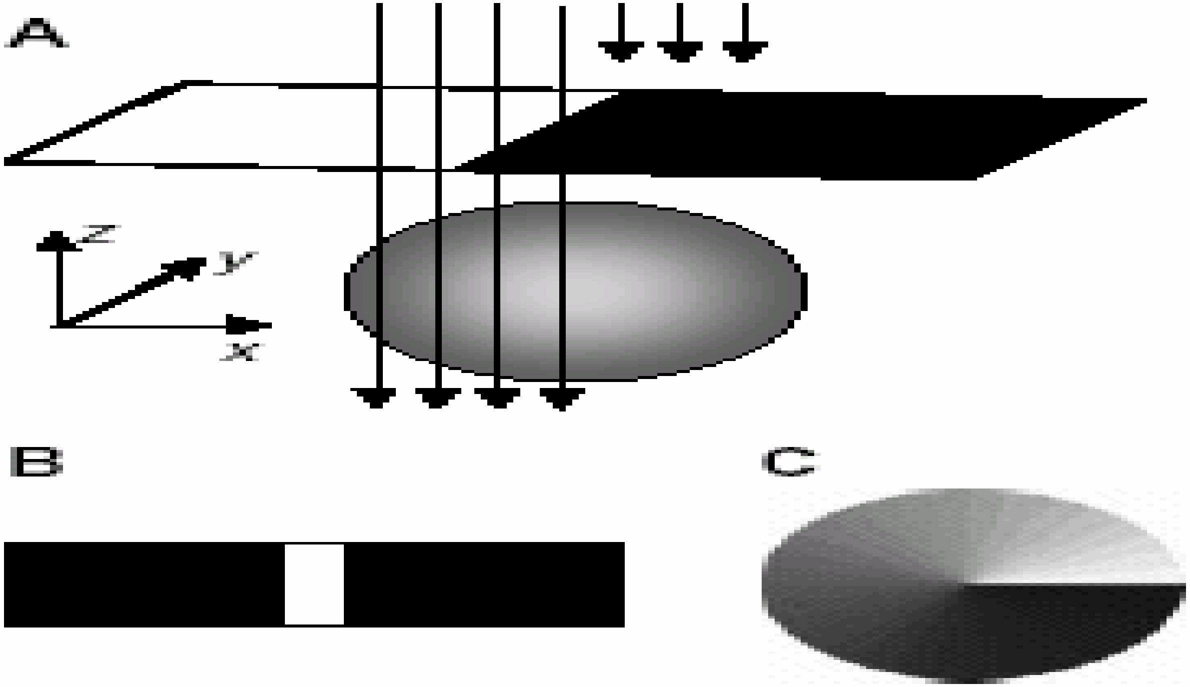

Fig. 1. (A) Writing a phase step onto the condensate. A far-detuned uniform light pulse projects a mask (a razor blade) onto the condensate. Because of the light shift, this imprints a phase distribution that is proportional to the light intensity distribution. A lens (not shown) is used to image the razor blade onto the condensate. The mask in (B) writes a phase stripe onto the condensate. The mask in (C) imprints an azimuthally varying phase pattern that can be used to create vortices.

10.4. Waveguides

Science 298, 1363 (2002)

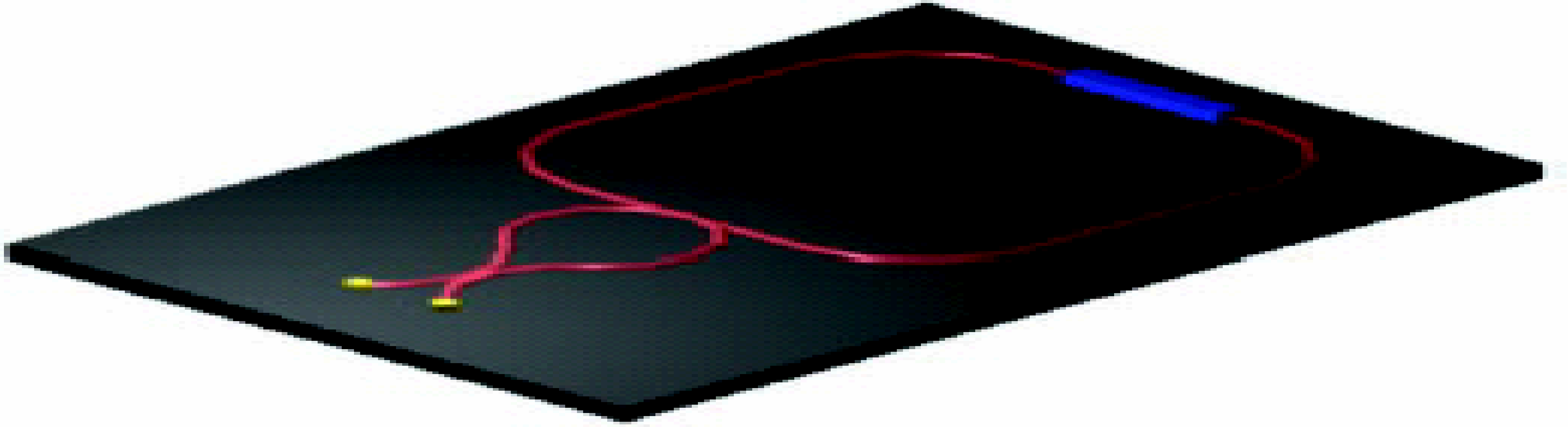

Fig. 3. Schematic of a possible geometry for a waveguide Sagnac-effect atom gyroscope. An atom gain element (blue) feeds a loop waveguide structure (red). Atoms are extracted and detected using correlated-state techniques to achieve sub-shot-noise limited detection (yellow). The past year has seen substantial progress in the development of each relevant element. A loop 10 cm by 10 cm might achieve a 10^6-fold improvement in sensitivity to rotations for intermediate acquisition bandwidths (tens of seconds), and a 10^4-fold improvement for high frequencies (less than 1 s). The long-term stability and accuracy are difficult to project.

10.5. BEC on chip

Nature 413, 498 (2001).

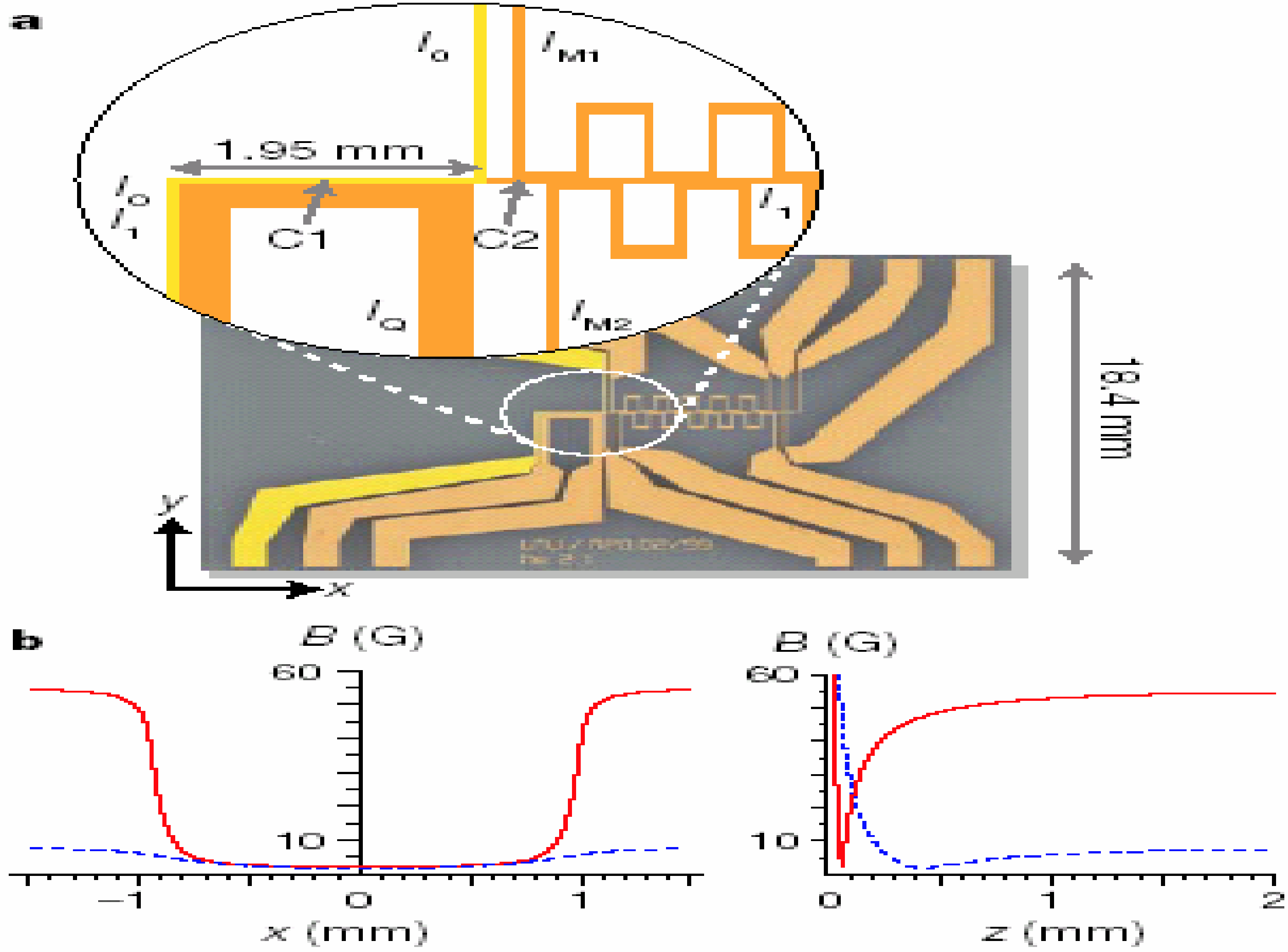

Figure 1 The chip and the magnetic potentials that it creates. **a**, Layout of the lithographic gold wires on the substrate. The inset shows the relevant part of the conductor pattern. I_0, I_1, I_{M1} and I_{M2} create the various magnetic potentials for trapping (see **b**) and transport, as described in the main text. I_Q is used only during trap loading (intermediate MOT step[5]). **b**, Potentials created by a wire current $I_0 = 2$ A for two different values of the external

10.6. Quantum tweezers (loading single atom)

Nature 411, 1024 (2001); Science 293, 278 (2001); Phys. Rev. Lett. 89, 070401 (2002).

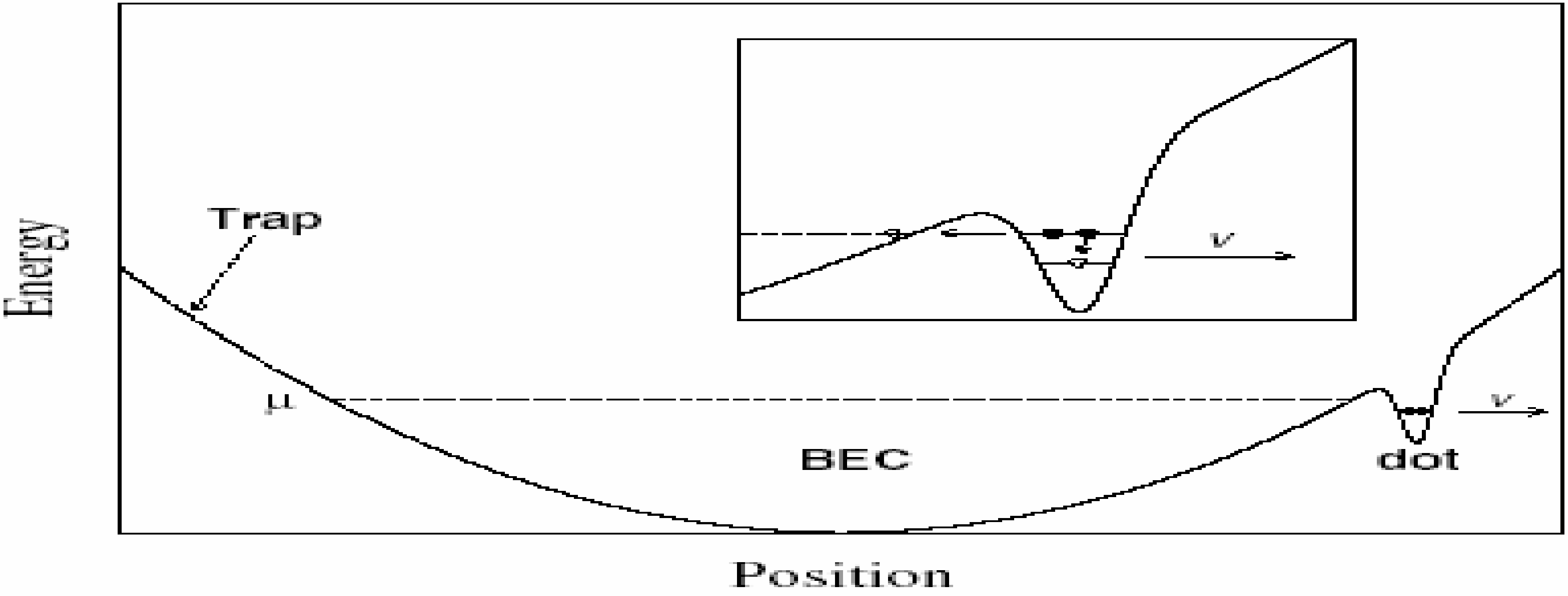

FIG. 1. A quantum dot (tweezer) moves out of a trapped BEC (reservoir) with the speed of v. The inset illustrates that a resonance occurs as the dot moves further away from the trap center such that the energy of the atoms matches the chemical potential μ of the condensate. If one of the atoms is tunneled into the BEC, the energy level of the dot is lowered, due to the absence of repulsion from the lost atom. Thus, no other atom has a chance of leaking back to the condensate at this position.

10.7. Information storage

C. Liu et al., Nature 409, 490 (2001).

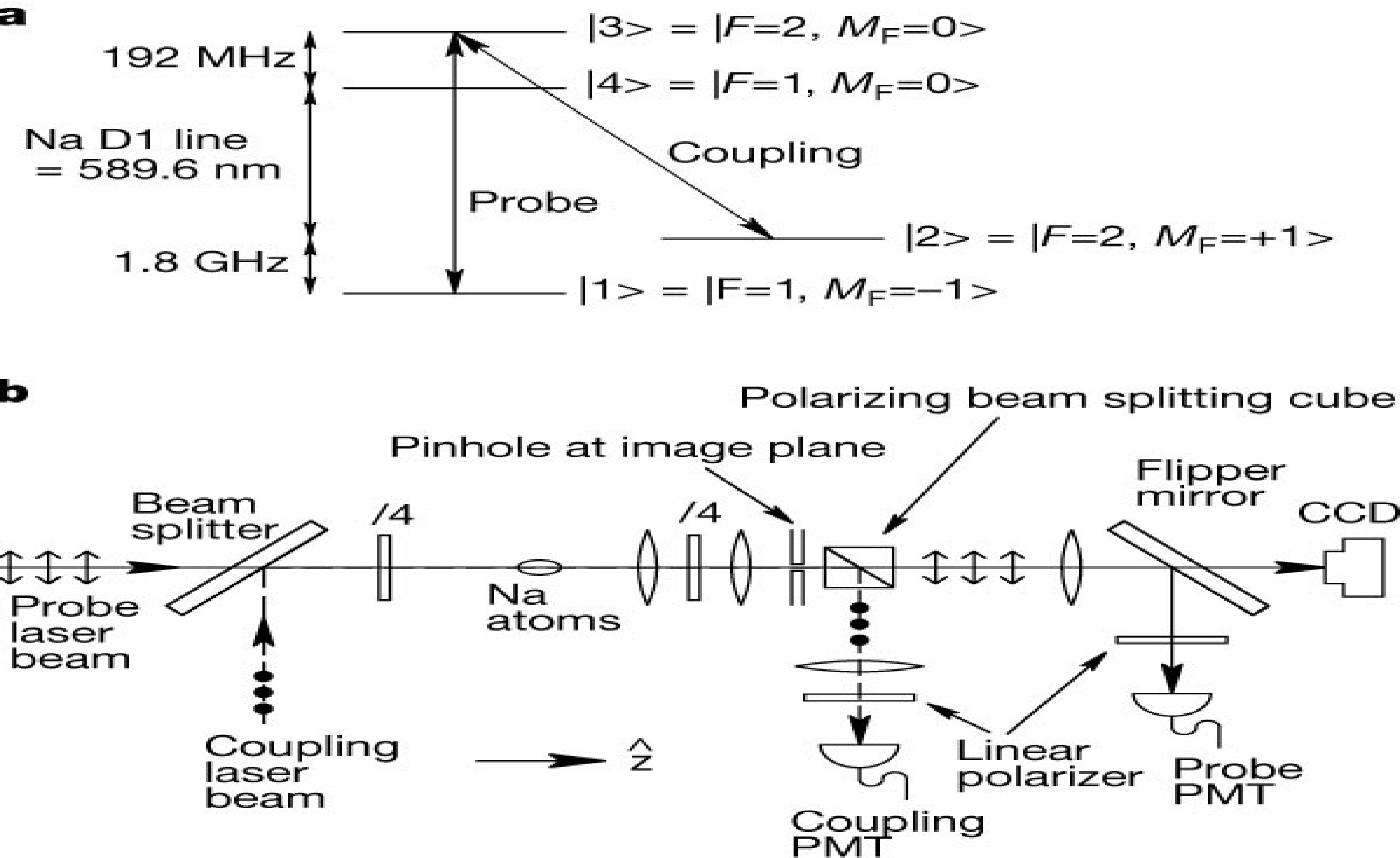

10.8. Quantum computer and entanglement

Nature 409, 63 (2001).

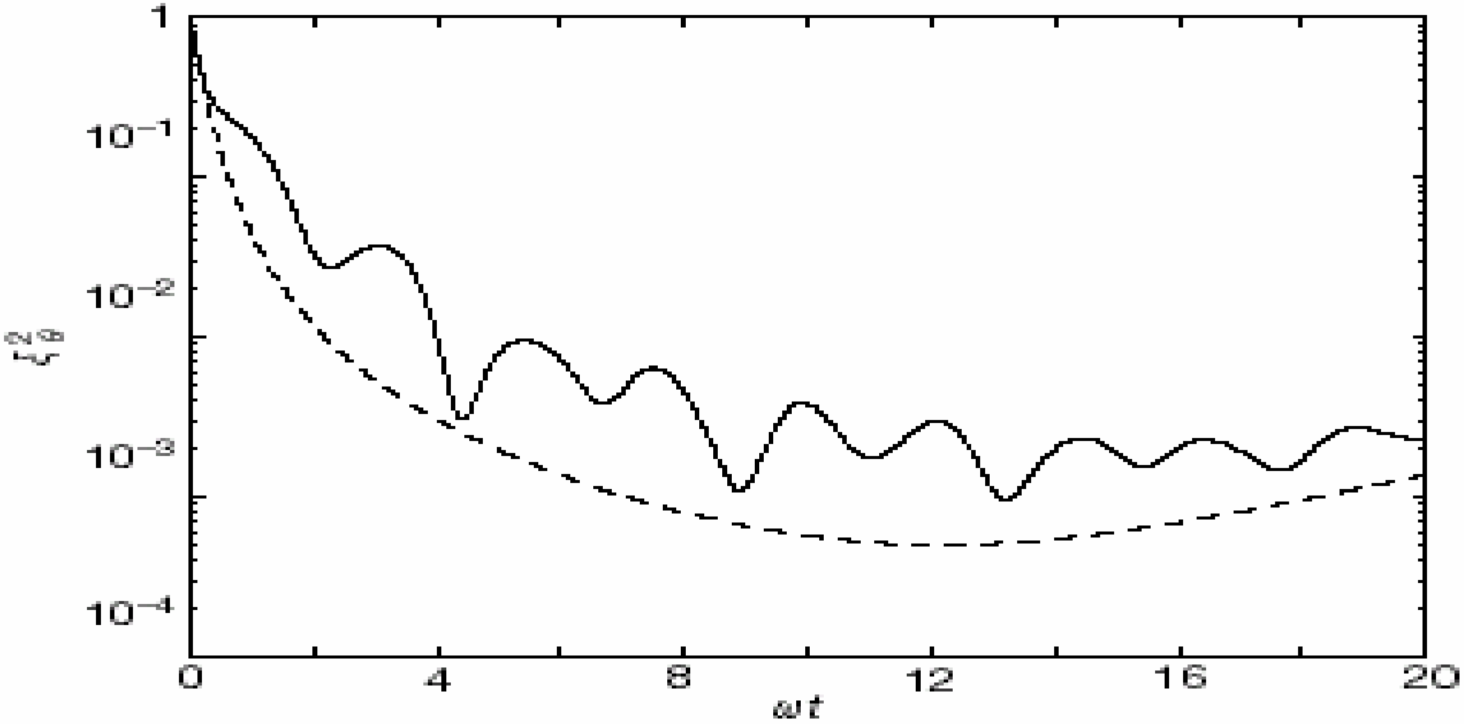

Figure 1 Reduction in the squeezing parameter ξ^2. A fast $\pi/2$ pulse between two internal states is applied to all atoms in the condensate. The subsequent free evolution with time results in a strong squeezing of the total spin. The angle θ is chosen such that ξ_θ^2 is minimal. The solid line shows the results of a numerical integration (see text). For numerical convenience we have assumed a spherically symmetric potential $V(r) = m\omega^2 r^2/2$. The parameters are $a_{aa}/d_0 = 6 \times 10^{-3}$, $a_{bb} = 2a_{ab} = a_{aa}$, and $N = 10^5$. The dashed curve shows the squeezing obtained from the hamiltonian $H_{\mathrm{spin}} = \hbar\chi J_z^2$. The parameter χ is chosen such that the reduction of $\langle J_x \rangle$ obtained from the solution in ref. 7 is consistent with the results of ref. 11.

10.9. Four-wave mixing

L. Deng et al., Nature 398, 218 (1999).

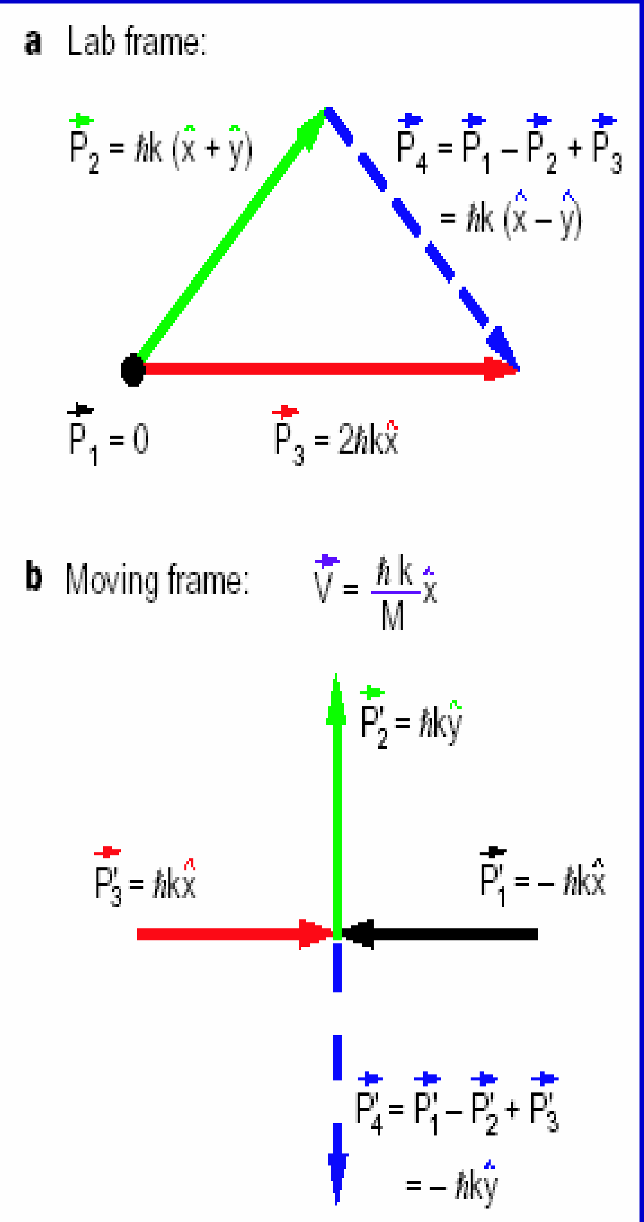

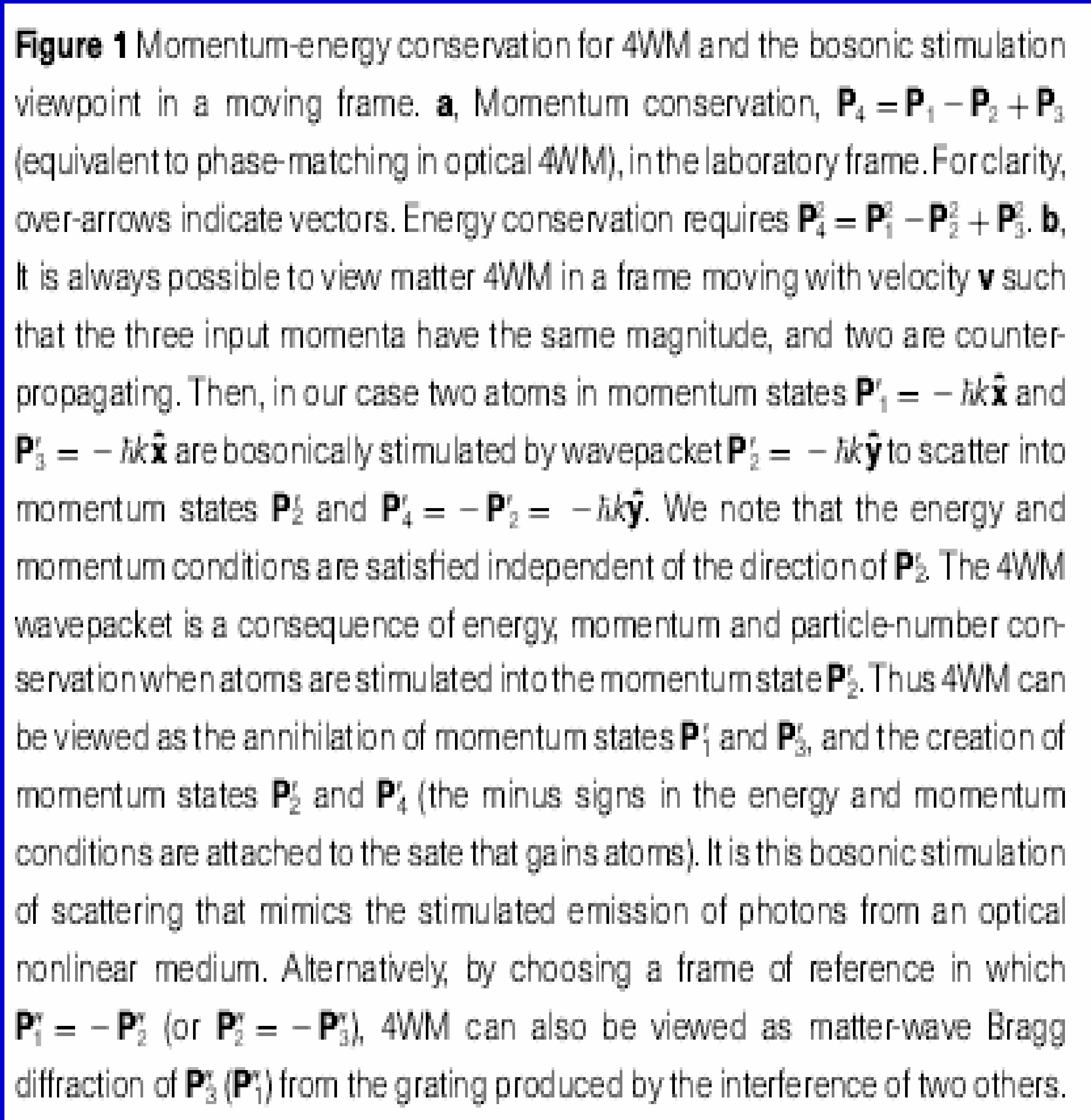

Figure 1 Momentum-energy conservation for 4WM and the bosonic stimulation viewpoint in a moving frame. **a**, Momentum conservation, $\mathbf{P}_4 = \mathbf{P}_1 - \mathbf{P}_2 + \mathbf{P}_3$ (equivalent to phase-matching in optical 4WM), in the laboratory frame. For clarity, over-arrows indicate vectors. Energy conservation requires $\mathbf{P}_4^2 = \mathbf{P}_1^2 - \mathbf{P}_2^2 + \mathbf{P}_3^2$. **b**, It is always possible to view matter 4WM in a frame moving with velocity **v** such that the three input momenta have the same magnitude, and two are counter-propagating. Then, in our case two atoms in momentum states $\mathbf{P}'_1 = -\hbar k\hat{\mathbf{x}}$ and $\mathbf{P}'_3 = -\hbar k\hat{\mathbf{x}}$ are bosonically stimulated by wavepacket $\mathbf{P}'_2 = -\hbar k\hat{\mathbf{y}}$ to scatter into momentum states $\mathbf{P}'_2$ and $\mathbf{P}'_4 = -\mathbf{P}'_2 = -\hbar k\hat{\mathbf{y}}$. We note that the energy and momentum conditions are satisfied independent of the direction of $\mathbf{P}'_2$. The 4WM wavepacket is a consequence of energy, momentum and particle-number conservation when atoms are stimulated into the momentum state $\mathbf{P}'_2$. Thus 4WM can be viewed as the annihilation of momentum states $\mathbf{P}'_1$ and $\mathbf{P}'_3$, and the creation of momentum states $\mathbf{P}'_2$ and $\mathbf{P}'_4$ (the minus signs in the energy and momentum conditions are attached to the sate that gains atoms). It is this bosonic stimulation of scattering that mimics the stimulated emission of photons from an optical nonlinear medium. Alternatively, by choosing a frame of reference in which $\mathbf{P}''_1 = -\mathbf{P}''_2$ (or $\mathbf{P}''_2 = -\mathbf{P}''_3$), 4WM can also be viewed as matter-wave Bragg diffraction of $\mathbf{P}''_3$ ($\mathbf{P}''_1$) from the grating produced by the interference of two others.

10.10. Reducing light speed

L.V. Hau, Nature 397, 594 (1999).

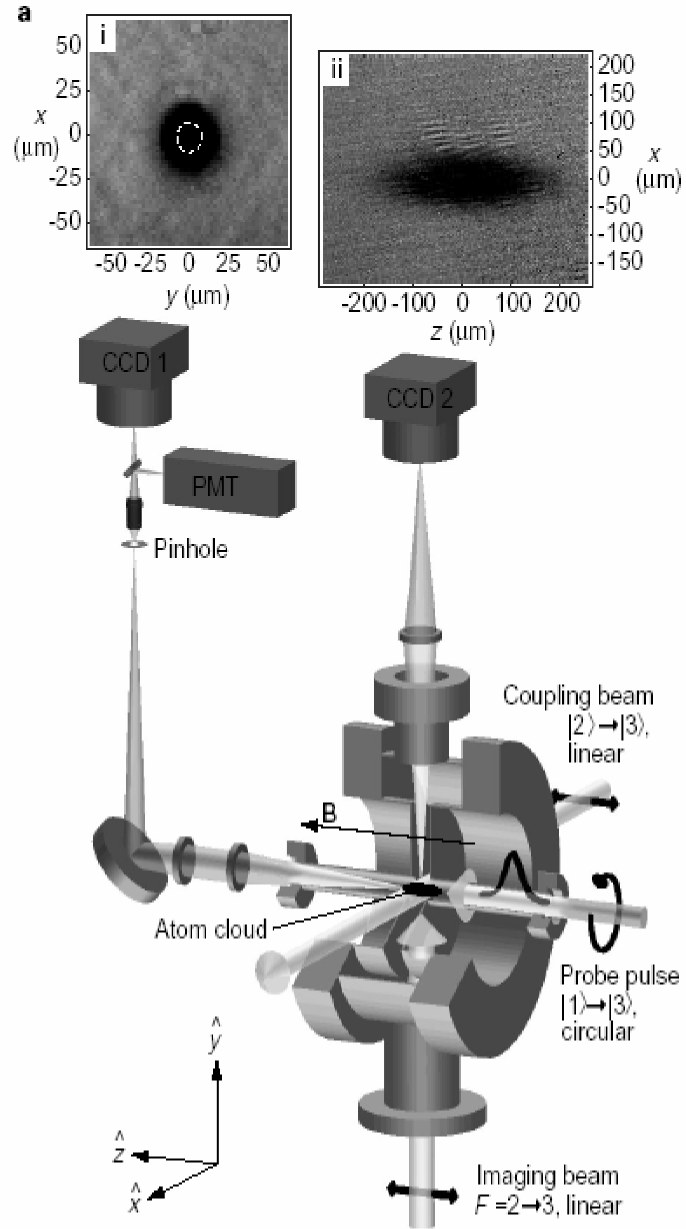

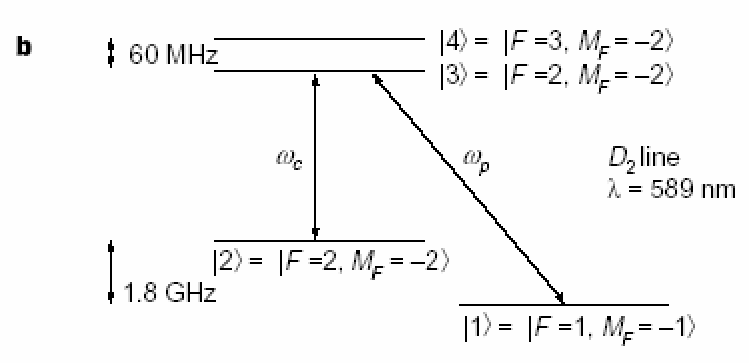

Figure 1 Experimental set-up. A ‘coupling’ laser beam propagates along the *x* axis with its linear polarization along the 11-G bias field in the *z* direction. The ‘probe’ laser pulse propagates along the *z* axis and is left-circularly polarized. With a flipper mirror in front of the camera CCD 1, we direct this probe beam either to the camera or to the photomultiplier (PMT). For pulse delay measurements, we place a pinhole in an external image plane of the imaging optics and select a small area, 15 μm in diameter, of the probe beam centred on the atom clouds (as indicated by the dashed circle in inset (i)). The pulse delays are measured with the PMT. The imaging beam propagating along the *y* axis is used to image atom clouds onto camera CCD 2 to find the length of the clouds along the pulse propagation direction (*z* axis) for determination of light speeds. Inset (ii) shows atoms cooled to 450 nK which is 15 nK above T_c. (Note that this imaging beam is never applied at the same time as the probe pulse and coupling laser). The position of a cloud and its diameter in the two transverse directions, *x* and *y*, are found with CCD 1. Inset (i) shows an image of a condensate.

10.11. Superradiance

S. Inouye et al., Science 285, 571 (1999).

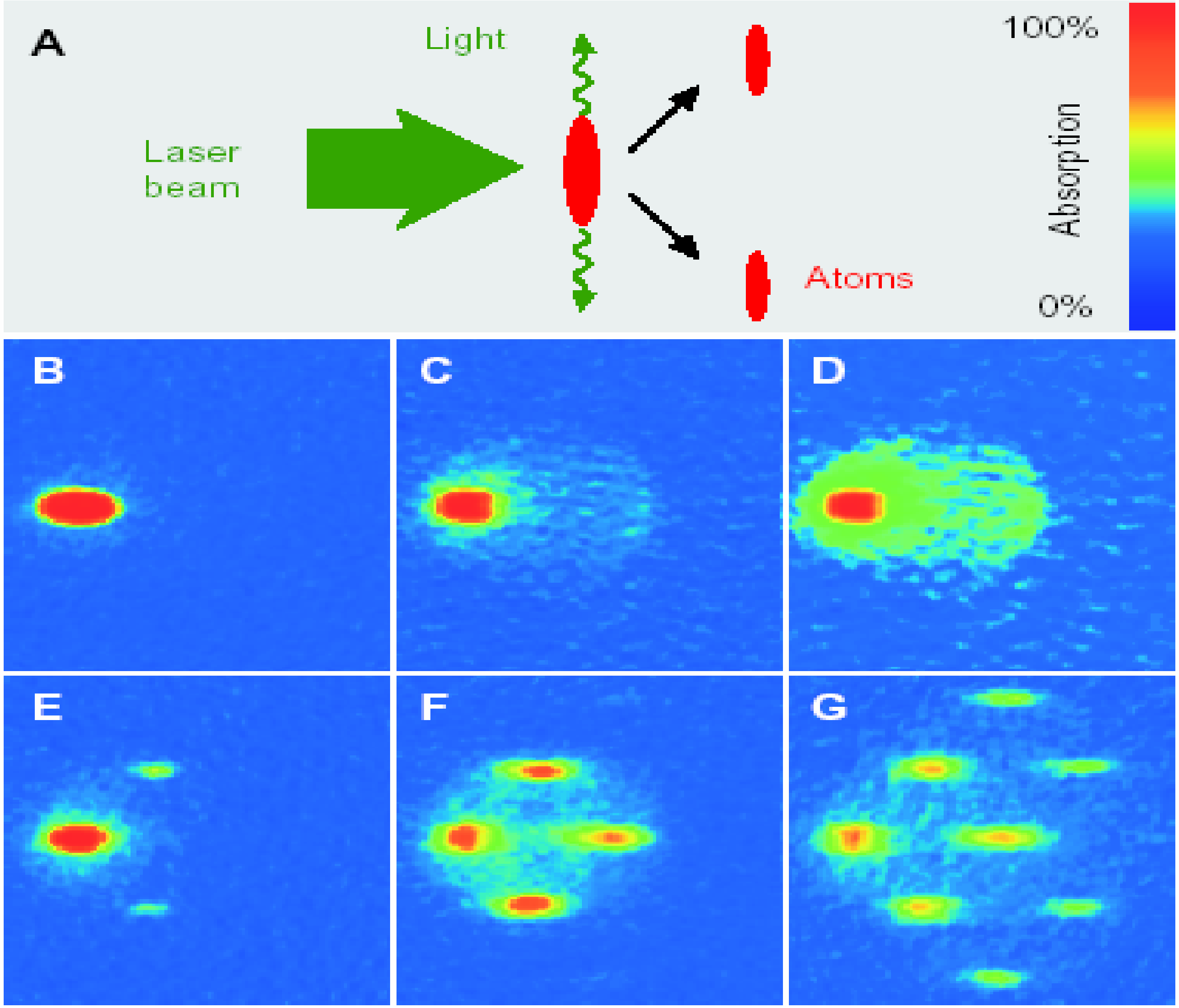

Fig. 1. Observation of superradiant Rayleigh scattering. **(A)** An elongated condensate is illuminated with a single off-resonant laser beam. Collective scattering leads to photons scattered predominantly along the axial direction and atoms at 45°. **(B to G)** Absorption images after 20-ms time of flight show the atomic momentum distribution after their exposure to a laser pulse of variable duration. When the polarization was parallel to the long axis, superradiance was suppressed, and normal Rayleigh scattering was observed (B to D). For perpendicular polarization, directional superradiant scattering of atoms was observed (E to G) and evolved to repeated scattering for longer laser pulses (F and G). The pulse durations were 25 (B), 100 (C and D), 35 (E), 75 (F), and 100 (G) μs. The field of view of each image is 2.8 mm by 3.3 mm. The scattering angle appears larger than 45° because of the angle of observation. All images use the same color scale except for (D), which enhances the small signal of Rayleigh scattered atoms in (C).

10.12. Supernova

S.L. Cornish et al., Phys. Rev. Lett. 85, 1795 (2000).

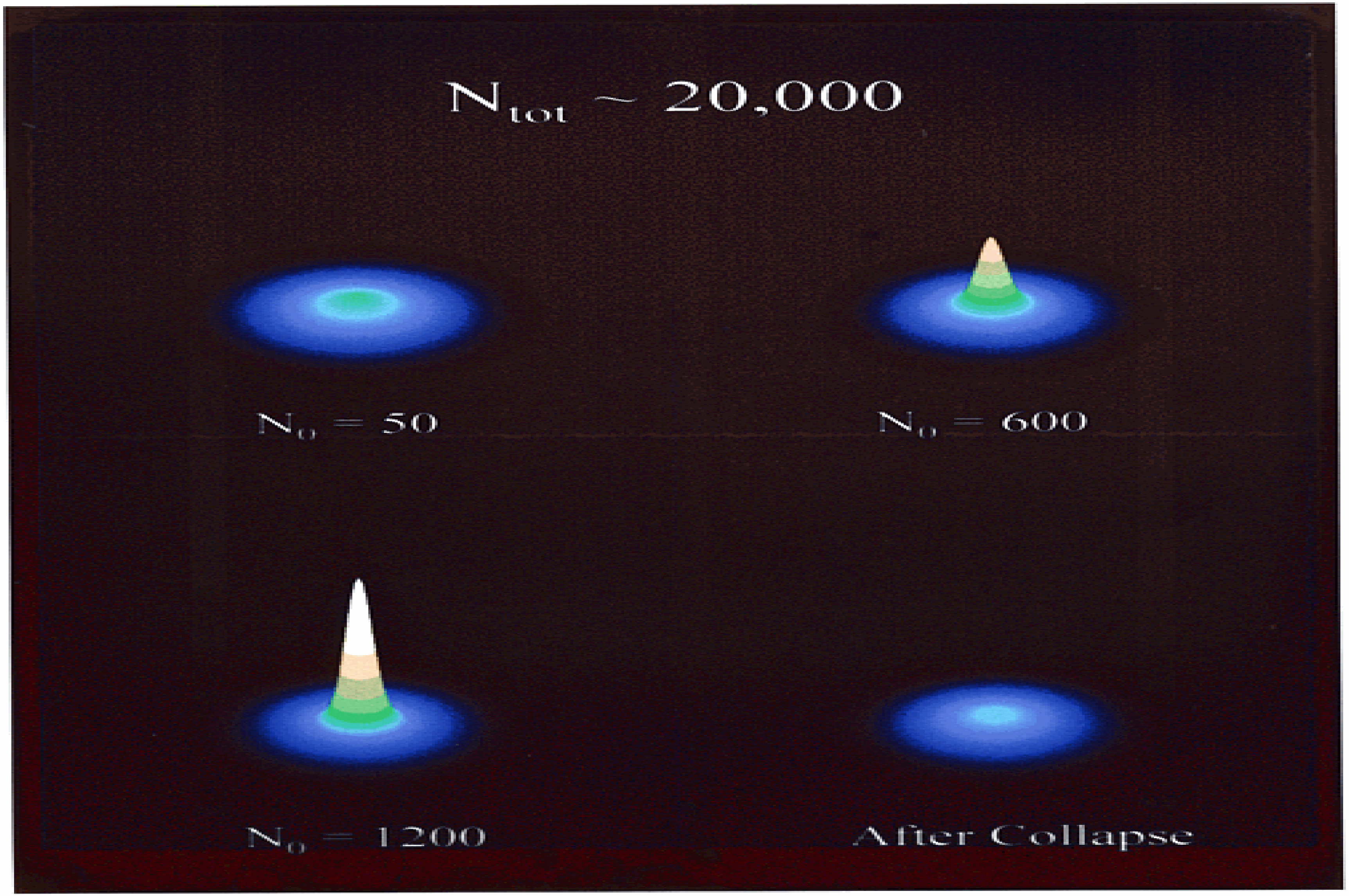

11. Outlook

11.1. Importance and applications

11.2. Future topics

11.1. Importance and applications

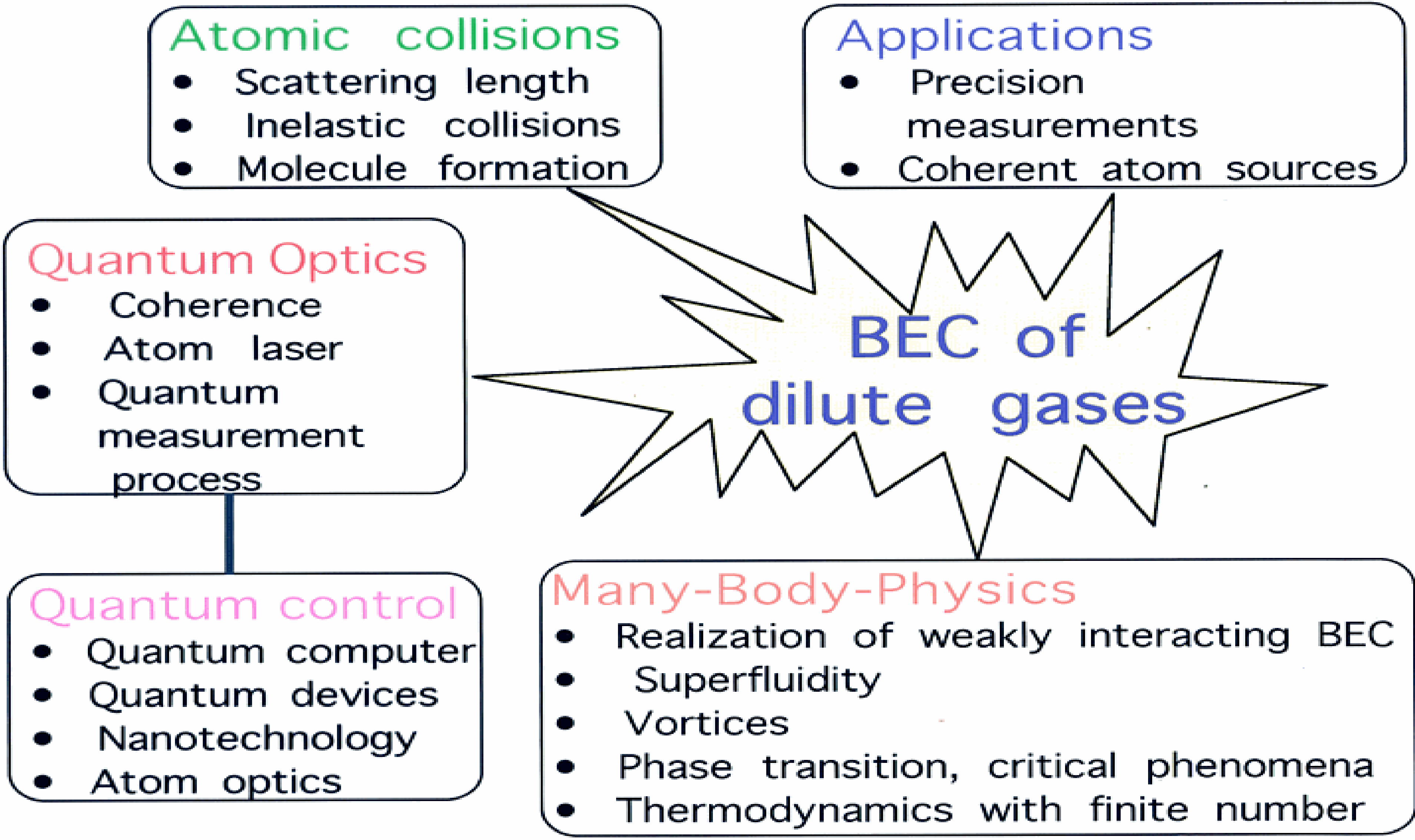

BEC of dilute gases

Atomic collisions

- Scattering length
- Inelastic collisions
- Molecule formation

Applications

- Precision measurements
- Coherent atom sources

Quantum Optics

- Coherence
- Atom laser
- Quantum measurement process

Quantum control

- Quantum computer
- Quantum devices
- Nanotechnology
- Atom optics

Many-Body-Physics

- Realization of weakly interacting BEC
- Superfluidity
- Vortices
- Phase transition, critical phenomena
- Thermodynamics with finite number

11.2. Future topics

W. Ketterle, Nature **416**, 211 (2002)

- **Bose-Einstein condensates become an**

ultralow-temperature laboratory

for atom optics, collisional physics and many-body physics, superfluidity, quantized vortices, Josephson junctions and quantum phase transitions.

谢 谢！